



i-Rheo Squeeze: broadband rheology of complex materials

Trung Son Nguyen

Matriculation Number: 3045544
School of Engineering
College of Science and Engineering
University of Glasgow

A dissertation presented in part fulfilment of the requirements of the
Degree of Master of Science in Medical Devices Engineering at The
University of Glasgow

15/08/2025

Abstract

A geometry-agnostic, model-free workflow was implemented to recover broadband linear viscoelastic (LVE) properties from a single step-indentation experiment. The software tool, i-Rheo Squeeze, computes the complex modulus $G^*(\omega) = G'(\omega) + iG''(\omega)$ as a transfer function by taking the ratio of the analytical Fourier transforms of the measured force $F(t)$ and a geometry-aware deformation $\Lambda[\delta(t)]$ derived from contact mechanics. An automated analysis-window finder, phase-preserving interpolation with virtual oversampling, and exportable plots/data were integrated in a Python/Streamlit application deployed behind NGINX for secure web access. Validation was performed on PDMS formulations (5:1, 10:1, 20:1; 2 mm thick) using log-spaced indentation depths (100 - 1400 μm) and two indenter families (spherical and cylindrical). Across identified linear-regime/yield-plateau ranges, $G'(\omega)$ and $G''(\omega)$ obtained from different tip sizes and types were consistent, supporting geometry-invariant recovery of moduli from a single relaxation. The expected stiffness ranking - 20:1 < 10:1 < 5:1 - was broadly observed; however, instances of 10:1 exceeding 5:1 indicated unresolved systematic factors (e.g., adhesion at shallow depth, finite-thickness effects, load history, or curing/storage variability). Trials with Whittaker–Henderson smoothing showed noise reduction but also attenuation of early-time features and underestimation of G'' at large smoothing parameters, indicating that conservative or no smoothing, combined with careful windowing and oversampling, provides the most reliable dissipation estimates. The study demonstrates that single-experiment indentation can deliver broadband $G'(\omega)$, $G''(\omega)$, and $\tan \delta(\omega)$ in a time-efficient manner without Maxwell-model fitting or frequency sweeps.

Contents

1	Introduction	5
1.1	Background	5
1.2	Outline	6
2	Theory	8
2.1	The Context of Rheology in This Study:	8
2.2	Conventional Linear Oscillatory Shear Rheometry and Broadband Linear Rheology	8
2.3	The classical approach to step-strain test	9
2.3.1	Classical step-strain analysis: the three assumptions	9
2.3.2	Drawbacks of current analytical procedures and the role of the Generalised Maxwell model	10
2.4	Measuring the linear response without assumptions; time→frequency without artefacts.	11
2.5	Model-free approach and Hertzian Contact Mechanics and Indentation Response	11
2.6	Software Development:	12
2.7	PDMS formulations (5:1, 10:1, 20:1): composition, properties, and expected rheology	13
2.8	Indentation depths and rationale for logarithmic spacing.	13
2.9	Whittaker smoothing: definition, properties, and why it is suitable to try in this study	14
3	Results and Discussion	16
3.1	Program and Web Application	16
3.2	Domain host:	20
3.3	Experimental Setup for Data Acquisition	21
3.4	Investigation of the linearity and stiffness of PDMS samples (5:1, 10:1, and 20:1).	22

3.5	Investigation of linear elasticity and yield plateau:	27
3.6	Investigation of the similarity in G' and G'' for each PDMS sample when using different indenter types and sizes:	31
3.7	Investigation of the properties of each PDMS sample from G' and G'' when using different indenter types and sizes:	33
3.8	Investigation of the application of the Whittaker smoothing filter for noise reduction in input data	36
4	Conclusions	45
5	Future Considerations	47
Bibliography		48
A	First appendix	51
	A.1 Implementation repository	51
B	Second appendix	52
	B.1 Data collection	52

Acknowledgements

I wish to express my sincere gratitude to my supervisor, Dr. Manlio Tassieri, and to Andrea Jannina Fernandez, a PhD candidate in the School of Engineering. Their expert guidance and steadfast encouragement were instrumental in navigating the challenges of this project and maintaining a high standard of professionalism. The successful completion of this work would not have been possible without their unwavering support.

I am also deeply grateful to my colleague, Fan Dong, for his consistent and dependable support throughout the entire research process.

Nomenclature

- t — Time [s].
- $F(t)$ — Normal force (indentation load) [N].
- $\delta(t)$ — Indentation depth [m].
- $\Lambda(t) = \Lambda(\delta(t))$ — Geometry-aware deformation term used in i-Rheo indentation [units depend on geometry; see below].
- $\dot{\Lambda}(t)$ — Time derivative of $\Lambda(t)$ [units of Λ/s].
- $g(0^+)$ — Post-step value of a generic signal $g(t)$.
- \dot{g}_∞ — Long-time slope/drift of $g(t)$ [units of g/s].
- ω — Angular frequency [$\text{rad} \cdot \text{s}^{-1}$].
- $G^*(\omega)$ — Complex shear modulus = $G'(\omega) + iG''(\omega)$ [Pa].
- $G'(\omega)$ — Storage (elastic) modulus [Pa].
- $G''(\omega)$ — Loss (viscous) modulus [Pa].
- $\eta^*(\omega)$ — Complex viscosity = $G^*(\omega)/(i\omega)$ [Pa·s].
- $\tan \delta(\omega)$ — Loss tangent = $G''(\omega)/G'(\omega)$ [-].
- $\varphi(\omega)$ — Phase lag between input and output in SAOS [rad] (used to avoid confusion with indentation δ).
- $G(t)$ — Shear relaxation modulus [Pa].
- E — Young's modulus [Pa].
- G — (Static) shear modulus = $\frac{E}{2(1+\nu)}$ [Pa].
- E^* — Reduced (contact) modulus = $\frac{E}{1-\nu^2}$ for a rigid indenter [Pa].
- ν — Poisson's ratio (PDMS ≈ 0.5) [-].
- T — Temperature [K] (lab: 22.8–25 °C).
- ρ — Density [$\text{kg} \cdot \text{m}^{-3}$] (rarely used).
- λ — Whittaker–Henderson smoothing parameter.

Chapter 1: Introduction

1.1 Background

The characterization of mechanical properties in materials is of particular interest in many areas, such as manufacturing industries, materials science and technology, biomechanics, and soft-matter physics. Among these, the property of viscoelasticity is especially important, describing the tendency of materials to exhibit both viscous and elastic responses to deformation. Such behavior is common in soft solids and complex fluids, including polymers, colloidal assemblies, gels, and biological tissues. In the linear viscoelastic (LVE) regime, the frequency-dependent storage modulus $G'(\omega)$ quantifies the recoverable elastic energy, while the loss modulus $G''(\omega)$ quantifies energy dissipated as heat (10). Accurate determination of these moduli over a broad frequency range reveals relaxation spectra, molecular architecture, and structure–property relationships that ultimately control performance in real applications.

Conventional dynamic mechanical analysis (DMA) obtains the LVE spectrum by applying small-amplitude oscillatory strain or stress at discrete frequencies. While robust and widely adopted, DMA is time-consuming because frequencies are probed sequentially, and practical instrument limits constrain both the low-frequency end (due to long experiment durations) and the high-frequency end (due to actuator and inertia limits) (35; 24). These constraints are particularly problematic for time-evolving systems (e.g., gelling solutions or living cells), where the material may change faster than a full sweep can be completed (2). To circumvent these limitations, transient protocols such as step-strain or step-stress relaxation are attractive because the sharp temporal input contains a continuum of Fourier components; the challenge is then to convert time-domain data to frequency-domain moduli in a way that is mathematically controlled and experimentally robust (35).

Recent advances address this challenge by directly evaluating the Fourier transforms of the input (strain or indentation) and output (stress or force) to compute $G^*(\omega) = G'(\omega) + iG''(\omega)$ without resorting to assumed constitutive forms. In bulk rheometry, this idea underpins the i-Rheo family of methods, enabling the direct conversion of relaxation compliance to moduli (9) and yielding close agreement with conventional frequency sweeps while dramatically shortening acquisition time (35). Closely related concepts emerged in microrheology, where thermal or driven probe motions are transformed to viscoelastic spectra via generalized Stokes–Einstein relations and frequency-domain analysis, extending accessible bandwidth and reducing sample volume (25; 11; 3). These developments collectively motivate Fourier-based pipelines that operate directly on raw transients to recover $G'(\omega)$ and $G''(\omega)$.

Indentation platforms—from benchtop instruments to AFM—offer additional advantages for soft materials: small test volumes, straightforward sample preparation, and compatibility with patterned or spatially heterogeneous specimens (2). However, general applicability across indenter geometries requires careful treatment of contact mechanics. While the classic Hertz solution provides the force–indentation relation for frictionless spherical contact in elastic solids (14), realistic studies routinely use conical, cylindrical (flat-punch), or pyramidal tips. Foundational extensions for viscoelastic half-spaces (21; 36) and the broader framework of contact mechanics (17), together with geometry-specific solutions and instrumented indentation methods (27), provide the basis to transform indentation-time signals

into physically meaningful deformation measures compatible with frequency-domain analysis.

Building on this background, the present work introduces i-Rheo Squeeze, a Python-based, domain-hosted application that generalizes the i-Rheo analytical strategy beyond a single probe geometry. The software ingests raw force–time and indentation–time transients from step-indentation tests and, after geometry-aware conversion of indentation to a deformation term, computes moduli by taking the ratio of the analytical Fourier transforms of force and deformation. In contrast to implementations specialized for spherical tips, i-Rheo Squeeze supports spherical, conical, cylindrical (flat-punch), and four-sided pyramidal indenters by invoking the appropriate contact relations (Hertz for spheres; Sneddon-type solutions for cones; established flat-punch/pyramidal formulations) (14; 32; 27). Numerically, the pipeline employs controlled interpolation and virtual oversampling to regularize sampling for the transform while preserving phase information that is essential for reliable G'' recovery (35; 9). The approach is validated on PDMS formulations spanning common mixing ratios (5:1, 10:1, 20:1), demonstrating broadband $G'(\omega)$ and $G''(\omega)$ consistent with expectations and highlighting the practical benefits of a geometry-agnostic, fast, and accessible workflow for viscoelastic characterization of soft materials (2; 35).

1.2 Outline

This dissertation presents the conception, implementation, and validation of i-Rheo Squeeze, a domain-hosted Python application for recovering broadband linear viscoelastic (LVE) properties from a single step-indentation experiment. The work is motivated by the need for rapid, geometry-agnostic analysis pipelines that transform raw time-domain force/indentation signals into frequency-domain moduli with minimal assumptions. The project integrates: (i) contact-mechanics models for multiple indenter geometries; (ii) a numerically stable, phase-preserving Fourier pipeline; and (iii) a practical software stack that automates data ingestion, analysis-window selection, visualisation, and export for routine laboratory use.

Aims and Objectives

The overarching aim is to design, develop, and validate a software tool for fast and accurate determination of $G'(\omega)$, $G''(\omega)$, and $\tan \delta(\omega)$ from step-indentation measurements. This aim is addressed through three objectives:

O1 – Generalise the analytical framework. Extend time-to-frequency conversion by incorporating appropriate contact models for at least two of the following indenter geometries: spherical, conical, cylindrical (flat-punch), and four-sided pyramidal; parameterise each by its relevant dimensions/angles.

O2 – Develop a robust Python program. Implement a user-oriented application that: loads and parses raw force/indentation/time data; automatically identifies the relaxation window with noise-aware thresholds and manual overrides; accepts indenter type and geometry; computes $G'(\omega)$, $G''(\omega)$, $\tan \delta$; produces publication-quality plots; and exports results for downstream analysis.

O3 – Acquire experimental validation data. Conduct step-indentation tests on well-characterised PDMS formulations (5:1, 10:1, 20:1) to demonstrate that recovered material properties are internally consistent across indenter type and size within validated depth ranges.

Organisation of the Report

chapter 1 – Introduction. Establishes the context and motivation for broadband LVE characterisation in soft materials; outlines limitations of conventional frequency-sweep approaches; frames step-based Fourier analysis as a fast alternative; states the project aim, objectives O1–O3, and contributions; and summarises the structure of the thesis.

chapter 2 – Theory and Methods. Introduces the linear viscoelastic framework and the spectral relationship between force, indentation-derived deformation, and moduli. Presents the contact-mechanics relations used for each supported indenter geometry and the assumptions underpinning their validity. Details the numerical pipeline—analysis-window detection, interpolation and virtual oversampling, analytical Fourier transform, and modulus extraction—together with user-exposed parameters, stability considerations, and the rationale for avoiding over-smoothing of phase-sensitive data. The chapter also documents software architecture, reproducibility choices, and the web deployment (reverse proxy and HTTPS).

chapter 3 – Results and Discussion. Reports the experimental protocol on PDMS (instrumentation, log-spaced indentation depths, temperature control) and evaluates the software on real datasets. Compares G' and G'' across spherical and cylindrical tips of two diameters, identifies linear-regime/yield-plateau ranges, and extracts representative stiffness values. Discusses the observed stiffness hierarchy ($20 : 1 \ll 10 : 15 : 1$), plausible causes for the $10 : 1 > 5 : 1$ anomaly, and the sensitivity of G'' to noise and phase. Assesses the effect of Whittaker smoothing on dissipation estimates and provides recommendations for trustworthy spectral recovery.

chapter 4 – Conclusions. Summarises the main findings: successful generalisation of the i-Rheo strategy across indenter geometries (O1); delivery of a robust, accessible Python application with automated preprocessing and export (O2); and experimental validation on PDMS demonstrating geometry-consistent moduli within validated depth ranges (O3). Highlights methodological insights (importance of windowing and phase fidelity) and practical implications for routine viscoelastic testing.

chapter 5 – Future Work. Outlines extensions to adhesive contact regimes, phase-preserving denoising and uncertainty quantification, broader material validation (hydrogels, tissues), automated quality control for non-stationary data, and software engineering enhancements (testing, packaging, acceleration, and spatial mapping).

Chapter 2: Theory

2.1 The Context of Rheology in This Study:

Rheology is the science that quantifies how materials deform and flow under applied loads by relating stress, strain, and strain rate, with particular emphasis on time- and frequency-dependent responses characteristic of soft solids and complex fluids (10; 24). In the linear viscoelastic (LVE) regime relevant to small deformations, the stress $\sigma(t)$ is given by the Boltzmann superposition integral over the strain history, and the Fourier transform of this relation yields the complex shear modulus $G^*(\omega) = G'(\omega) + iG''(\omega)$, where G' measures the recoverable elastic energy and G'' measures viscous dissipation; the loss tangent $\tan \delta = G''/G'$ provides a compact measure of damping (10). Indentation rheology extends this framework by using contact mechanics to convert the measured indentation $\delta(t)$ into a deformation term $\Lambda(t)$ appropriate to the indenter geometry (e.g., Hertzian for spheres), enabling direct comparison with bulk LVE quantities (17). Modern i-Rheo methods compute $G^*(\omega)$ from a single step-relaxation by taking the ratio of the Fourier transforms of the output force $F(t)$ and the geometry-aware deformation $\Lambda(t)$, avoiding parametric fitting and dramatically broadening the accessible frequency range compared to sequential frequency sweeps (9; 35; 2).

2.2 Conventional Linear Oscillatory Shear Rheometry and Broad-band Linear Rheology

In small-amplitude oscillatory shear (SAOS), a sample is subjected to a sinusoidal shear strain,

$$\gamma(t) = \gamma_0 \sin(\omega t), \quad (2.1)$$

that is sufficiently small to keep the response in the linear viscoelastic (LVE) regime; the measured shear stress is

$$\sigma(t) = \sigma_0 \sin(\omega t + \varphi), \quad (2.2)$$

where $\varphi(\omega)$ is the phase lag between stress and strain (10; 24). Using complex notation, the complex modulus is defined as the ratio of the complex stress to the complex strain at the same frequency(35),

$$G^*(\omega) = \frac{\hat{\sigma}(\omega)}{\hat{\gamma}(\omega)} = \frac{\sigma_0}{\gamma_0} [\cos \varphi(\omega) + i \sin \varphi(\omega)] = G'(\omega) + iG''(\omega), \quad (2.3)$$

so that the storage modulus and loss modulus follow directly as(35)

$$G'(\omega) = \frac{\sigma_0}{\gamma_0} \cos \varphi(\omega), \quad G''(\omega) = \frac{\sigma_0}{\gamma_0} \sin \varphi(\omega), \quad (2.4)$$

and the loss tangent is $\tan \delta(\omega) = G''(\omega)/G'(\omega)$; equivalently, the complex viscosity is $\eta^*(\omega) = G^*(\omega)/(i\omega)$ (10). In practice (e.g., cone-and-plate geometry), the rheometer imposes $\gamma(t)$ at a chosen ω , measures torque and displacement to obtain σ_0/γ_0 and $\varphi(\omega)$, and repeats across a set of discrete frequencies to build the spectrum $G'(\omega), G''(\omega)$. Linearity is verified by checking that G' and G'' are independent of the strain amplitude γ_0 within the chosen range; bandwidth is limited at low ω by experiment duration and drift, and at high ω

by instrument inertia and sample–fixture resonances (24). Despite its benchmark status, conventional small-amplitude oscillatory shear (SAOS) rheometry has well-known practical and conceptual limitations. Bandwidth is inherently constrained because frequencies are probed sequentially; low-frequency data require long experiments susceptible to drift and evaporation, whereas high-frequency data are limited by instrument inertia, geometry resonances, and torque sensitivity (typically confining ω to about 10^{-2} – 10^2 rad s $^{-1}$) (10; 24; 35). SAOS also demands bulk, homogeneous specimens of millimetre dimensions prepared in standard fixtures (cone–plate, parallel plate), which is incompatible with thin films, small-volume samples, spatially heterogeneous systems, or situations where surfaces/adhesion alter the measured response (24). Because the spectrum is assembled over time, SAOS is poorly suited to time-evolving materials (e.g., curing gels, living cells): the microstructure can change during a sweep, compromising spectral consistency (35; 2). Furthermore, SAOS reports a macroscopic shear average; it cannot readily probe local mechanics or accommodate non-standard test geometries, whereas many applications require indentation-based access to confined regions or patterned substrates (2). Finally, attempts to extend bandwidth by stitching disparate methods (DMA, creep/relaxation transforms, microrheology) introduce inter-method biases and require additional assumptions (e.g., thermorheological simplicity for time–temperature superposition) that may not hold for soft networks and composites (10; 35).

Research Gap

There is a need for a single-shot, broadband, geometry-agnostic methodology that

- (i) extracts $G'(\omega)$, $G''(\omega)$, $\tan \delta(\omega)$ directly from raw transients without constitutive fitting;
- (ii) works with indentation data and multiple tip geometries via appropriate contact mechanics;
- (iii) preserves phase fidelity so G'' is reliable; and
- (iv) is practical for small volumes and evolving samples.

Prior i-Rheo implementations demonstrate the promise of computing moduli by taking the ratio of Fourier transforms of input and output signals from a single step response, but these have largely been tied to specific experimental setups and most commonly to spherical contact only (9; 35; 2).

2.3 The classical approach to step-strain test

2.3.1 Classical step-strain analysis: the three assumptions

In a classical step-strain test, the strain is increased from 0 to a target value γ over a short but finite ramp of duration ε ending at t_0 , and then held constant. In the linear viscoelastic (LVE) regime the stress obeys the Boltzmann superposition integral(35)

$$\sigma(t) = \int_{-\infty}^t G(t - t') \dot{\gamma}(t') dt', \quad (2.5)$$

so that for a uniform ramp $\dot{\gamma}(t') = \gamma/\varepsilon$ on $t' \in [t_0 - \varepsilon, t_0]$,

$$\sigma(t) = \frac{\gamma}{\varepsilon} \int_{t_0 - \varepsilon}^{t_0} G(t - t') dt'. \quad (2.6)$$

The classical reduction of this expression relies on three assumptions (10; 9; 35).

- (A1) Mean-value (“instantaneous step”) approximation. The convolution over the finite ramp is replaced by a single evaluation of G using the mean-value theorem,

$$\sigma(t) \approx \frac{\gamma}{\varepsilon} \varepsilon G(t - t_0 + \phi\varepsilon) = \gamma G(t - t_0 + \phi\varepsilon), \quad 0 \leq \phi \leq 1, \quad (2.7)$$

i.e., the finite ramp is treated as if it were an instantaneous step occurring at an effective time within the ramp determined by ϕ (often taken ad hoc as $\phi = 1/2$).

- (A2) Time-origin shift. The end of the ramp is chosen as the origin so that $t_0 = 0$ and the argument becomes $t + \phi\varepsilon$; practically, the shift is absorbed into the definition of $t = 0$.
- (A3) Long-time limit. Analysis is restricted to $t \gg \varepsilon$, where the ramp duration is neglected and

Together, (A1)–(A3) justify reading off the relaxation modulus directly from the post-ramp stress, but at the cost of discarding early-time information and introducing an uncontrolled parameter ϕ ; consequently, the high-frequency part of $G^*(\omega)$ (obtained via Laplace/Fourier transform or by fitting $G(t)$ to generalized-Maxwell forms) is sensitive to those approximations and to any additional model bias (10; 9; 35).

2.3.2 Drawbacks of current analytical procedures and the role of the Generalised Maxwell model

A common way to convert relaxation data into frequency-domain moduli is to fit the stress–relaxation function with a Generalised Maxwell (GM) model, i.e. a discrete sum of exponential modes(35),

$$G(t) = \sum_{i=1}^n G_i e^{-t/\tau_i} \implies G^*(\omega) = \sum_{i=1}^n \frac{i\omega\tau_i G_i}{1 + i\omega\tau_i}, \quad (2.8)$$

where $\{G_i, \tau_i\}_{i=1}^n$ are spring strengths and relaxation times chosen to reproduce the data (10; 39; 24). Although analytically convenient and physically interpretable in terms of modes, this parametric inversion has four well-documented drawbacks.

- (i) Accuracy and non-uniqueness. Recovering $\{G_i, \tau_i\}$ from noisy time- or frequency-domain measurements is an ill-posed inverse problem: many different mode sets can fit the same data within experimental error, and the inferred spectrum is highly sensitive to noise and preprocessing (15; 1). As a result, the fitted $G^*(\omega)$ may be numerically accurate yet not unique, which undermines quantitative comparisons across instruments or laboratories.
- (ii) Operator bias in the number of modes. The analyst must choose n (and often initial guesses for τ_i), a decision that strongly biases the outcome: too few modes underfit broad spectra; too many modes overfit noise and create spurious features (39; 24).
- (iii) A strong long-time assumption. Classical GM fitting typically assumes that beyond the last mode the relaxation remains exponential, so that the late-time tail can be represented by a finite set of τ_i . This assumption is not generally valid for systems that display broad, non-exponential (e.g., power-law or stretched-exponential) relaxation—typical of entangled, cross-linked, or heterogeneous soft materials (23; 10).
- (iv) Loss of early-time information. Because points (i) and (ii) make the fit unstable near $t \rightarrow 0^+$ (where finite ramp and instrument response complicate the signal), analysts often down-weight or discard short-time data to stabilise the fit. This practice removes precisely the information that encodes the high-frequency part of the spectrum, leading to systematic underestimation or smearing of $G'(\omega)$ and, crucially, $G''(\omega)$ at large ω (9; 35).

2.4 Measuring the linear response without assumptions; time→frequency without artefacts.

In the i-Rheo framework, a linear viscoelastic material is treated as a linear time-invariant (LTI) system whose input $u(t)$ (strain or a geometry-aware deformation) and output $y(t)$ (stress or force) are related by the Boltzmann superposition integral, $\sigma(t) = \int_{-\infty}^t G(t-t')\dot{\gamma}(t') dt'$. Taking Fourier transforms converts the convolution into a product (35) so that

$$\hat{\sigma}(\omega) = [i\omega\hat{G}(\omega)]\hat{\gamma}(\omega) \implies G^*(\omega) = \frac{\hat{\sigma}(\omega)}{\hat{\gamma}(\omega)} = G'(\omega) + iG''(\omega), \quad (2.9)$$

i.e., the complex modulus is exactly the transfer function $H(\omega) = \hat{y}(\omega)/\hat{u}(\omega)$ of the LTI system (9; 35). Crucially, i-Rheo does *not* fit $G(t)$ to a Maxwell sum nor assume an “instantaneous step”; instead it computes the Fourier transform of the raw, finite-length time record directly and forms the spectral ratio. Let $g(t)$ denote any causal time-dependent quantity (stress, strain, force, or deformation) sampled at N points $\{(t_k, g_k)\}_{k=1}^N$ over $[0, t_N]$. Following Evans’ analytical development, one defines a piecewise-linear (or non-overshooting cubic) interpolant for $g(t)$ and evaluates its transform in closed form, which properly accounts for the finite window (35):

$$-\omega^2\hat{g}(\omega) = i\omega g(0^+) + (1 - e^{-i\omega t_1}) \frac{g_1 - g(0^+)}{t_1} + \dot{g}_\infty e^{-i\omega t_N} + \sum_{k=2}^N \frac{g_k - g_{k-1}}{t_k - t_{k-1}} (e^{-i\omega t_{k-1}} - e^{-i\omega t_k}), \quad (2.10)$$

where $g(0^+) = \lim_{t \rightarrow 0^+} g(t)$ and $\dot{g}_\infty = \lim_{t \rightarrow \infty} \dot{g}(t)$ (9; 35). To minimise spectral leakage at high ω , i-Rheo augments this analytic transform with virtual oversampling: the measured waveform is first reconstructed with a phase-preserving, non-overshooting spline and then densely resampled before applying the above expression, which markedly reduces truncation artefacts while preserving the early-time information that governs $G''(\omega)$ (34; 35). The usable frequency band is set by the experimental window rather than by a swept-sine schedule: $\omega_{\max} \sim 1/t_{\min}$ (set by the smallest reliable time increment after the step) and $\omega_{\min} \sim 1/t_N$ (set by the total relaxation time) (2).

2.5 Model-free approach and Hertzian Contact Mechanics and Indentation Response

Two indenter families were employed - spherical and cylindrical (flat punch) - with each experiment recording the force $F(t)$ and indentation $\delta(t)$ as functions of time. Under linear viscoelasticity, the response obeys the principle of superposition: the effect of successive increments of indentation adds linearly, yielding the hereditary relation

$$F(t) = \int_0^t G(t-\tau) \frac{d}{d\tau} \Lambda(\delta(\tau)) d\tau, \quad (2.11)$$

where $G(t)$ is the shear relaxation modulus and $\Lambda(\delta)$ is the instantaneous elastic deformation measure defined by the relevant contact-mechanics model (10; 38). For an incompressible linear elastic half-space ($\nu \approx 0.5$) and a rigid spherical probe of radius R , Hertzian contact gives

$$F = E \frac{4R^{1/2}}{3(1-\nu^2)} \delta^{3/2} = G \frac{8R^{1/2}}{3(1-\nu)} \delta^{3/2}. \quad (2.12)$$

using $E = 2G(1 + \nu)$ (20) implies E^* is constant for a fixed ν , so the corresponding deformation term can be chosen as

$$\Lambda(\delta(t)) = \frac{8R^{1/2}}{3(1 - \nu)}\delta^{3/2}(t). \quad (2.13)$$

For a cylindrical flat punch of radius a :

$$F = E \frac{2a}{1 - \nu^2} \delta = G \frac{4a}{1 - \nu} \delta \quad (2.14)$$

and thus the deformation term

$$\Lambda(\delta(t)) = \frac{4a}{1 - \nu} \delta(t) \quad (2.15)$$

again after substituting $E = 2G(1 + \nu)$ for $\nu \approx 0.5$ (30; 20). In both cases, Λ depends only on geometry and δ , so once the probe dimensions (R or a and ν are fixed by the experimental design, the time dependence in the constitutive equation enters exclusively through $\delta(t)$. This formulation allows the viscoelastic response to be determined without imposing a Maxwell fit, by transforming $F(t)$ and $\Lambda(\delta(t))$ directly within the linear viscoelastic framework (10; 38; 30; 20).

2.6 Software Development:

The application for this study was implemented from scratch in Python to place the rheological analytics (analytical Fourier transform, virtual oversampling, and geometry-aware deformation mapping) in the same language ecosystem that provides mature, peer-reviewed numerical libraries. Vectorised array operations in NumPy enable efficient manipulation of time–frequency data and convolution kernels, while SciPy supplies robust interpolation, optimization, and signal-processing routines used by the window finder and oversampling pipeline; figures are generated with Matplotlib for publication-quality plots (12; 40; 16). These choices keep the numerical core close to the theory (9; 35) while minimising translation overhead between research code and deployable software.

For the user interface, Streamlit was adopted, an open-source Python framework designed specifically for turning analytical scripts into interactive data apps with minimal boilerplate. Streamlit’s declarative, reactive model lets widgets (sliders, file uploaders, selectors) reflect code state automatically, so the moduli plots and diagnostic panels update immediately when a user changes the analysis window, interpolation density, or indenter geometry. This shortens the loop between experiment and analysis and keeps the entire stack in Python—no bespoke front-end code—reducing maintenance cost while promoting reproducibility. Streamlit’s docs explicitly position it as “a faster way to build and share data apps,” emphasising the small amount of code required and the iterative development workflow that syncs UI with script state.

To expose the app securely on the web and to decouple the Python process from public traffic, NGINX is placed in front of the Streamlit server as a reverse proxy. In this role, NGINX accepts client connections on ports 80/443, handles TLS termination (HTTPS), applies request-header normalization, and buffers responses before forwarding them to the internal Streamlit service (e.g., `localhost :8502`). This architecture improves performance (kernel-level event loop and buffering), reduces attack surface on the Python process, and simplifies certificate management and HTTP→HTTPS redirection. NGINX’s official documentation details reverse-proxy configuration, buffering behaviour in the `nginx_http_proxy_module`, and TLS termination for HTTPS sites; it also supports request routing and (if desired) HTTP

load balancing to multiple application instances for scalability and high availability. In practice, the deployment in this study runs the Streamlit app as a non-root background service bound to a high port, while NGINX listens publicly and proxies traffic, enabling clean separation of concerns: Python for the rheology and interactivity; NGINX for transport-layer security, caching/buffering, and production hardening.

In this study, these design choices allow the model-free i-Rheo/AFM2 algorithms to be translated directly into a responsive tool that laboratory users can access in a browser. The numerical core (NumPy/SciPy) reproduces the analytical Fourier pipeline and contact-mechanics mappings; Streamlit provides an intuitive control panel for analysis-window selection and parameter tuning; and NGINX supplies a production-grade edge that terminates HTTPS, proxies requests, and scales out if needed—so broadband LVE spectra can be computed and shared reliably from any workstation running a browser.

2.7 PDMS formulations (5:1, 10:1, 20:1): composition, properties, and expected rheology.

Polydimethylsiloxane (PDMS) is a platinum-catalysed, addition-cured silicone elastomer obtained by hydrosilylation between vinyl-terminated PDMS chains (base) and a multifunctional methylhydrosiloxane crosslinker (curing agent). The mixing ratio (base:curing agent) controls the network cross-link density: 5:1 contains the highest fraction of crosslinker, 10:1 is the manufacturer’s standard, and 20:1 is intentionally under-cross-linked; at room temperature ($\approx 23\text{--}25^\circ\text{C}$) all three are deep in the rubbery regime ($T_g \approx -120^\circ\text{C}$) (18; 28). In the linear viscoelastic (LVE) framework, the rubbery plateau shear modulus scales with the number density of elastically active strands, $G_{\text{plateau}} \approx \nu k_B T$, so increasing cross-link density monotonically increases $G'(\omega)$ over the accessible frequency band (37; 31; 10). For PDMS, dynamic and indentation measurements consistently report moduli in the MPa range that rise with crosslinker content, i.e., $G_{20:1} < G_{10:1} < G_{5:1}$ at comparable ω (28; 18). The loss modulus $G''(\omega)$ reflects frictional motion of chain segments and dangling ends; as cross-link density increases the load-bearing network becomes more constrained, generally reducing the loss tangent $\tan \delta = G''/G'$ and making the response more “elastic-like,” although the absolute magnitude of G'' can either decrease (fewer mobile segments) or remain comparable depending on measurement frequency and the population of non-load-bearing chains (10; 31). Using 5:1, 10:1, and 20:1 provides a convenient, reproducible way to span nearly an order of magnitude in stiffness while keeping chemistry, surface energy, and Poisson’s ratio (≈ 0.5) essentially constant—ideal for validating an algorithm that should recover consistent viscoelastic spectra across different indenters from a single relaxation experiment (18; 28). Based on rubber-elasticity theory and prior DMA/indentation reports, we expect (i) a monotonic stiffness ranking $G'_{20:1} < G'_{10:1} < G'_{5:1}$; (ii) a weak frequency dependence of G' across the rubbery plateau with G'' lower than G' and typically showing a broad maximum at intermediate ω ; and (iii) a decreasing $\tan \delta$ with increasing cross-link density (10; 31). In this study, these expectations provide the a priori checks for our model-free, indentation-based i-Rheo analysis: if the pipeline is correct, the recovered $G'(\omega)$ and $G''(\omega)$ for each ratio should reflect this cross-link-controlled ranking independently of indenter geometry (sphere, cylinder) once the appropriate contact-mechanics mapping $\Lambda(\delta)$ is applied.

2.8 Indentation depths and rationale for logarithmic spacing.

In this study, step-indentation tests were performed at depths 100, 200, 300, 400, 700, 1000, and 1400 μm on PDMS slabs of uniform thickness $h = 2\text{ mm}$. Depths were chosen on a logarithmic scale rather than a linear grid to (i) capture the rapidly changing mechanics at shallow

contact—where contact radius $a \sim (R\delta)^{1/2}$ and stress fields evolve nonlinearly with δ —while (ii) avoiding an excessive number of tests at large δ where responses vary more slowly (17; 27). Log spacing provides an efficient coverage of the dimensionless thickness parameter $a/h \propto \delta^{1/2}/h$ and the effective strain ε , thereby sampling both the near-surface regime and the onset of finite-thickness effects with fewer, but more informative, points (17). It also improves signal-to-noise at the low end (100–300 μm gives measurable forces without being dominated by contact-detection noise) and limits history/damage by avoiding an unnecessarily dense series of large indentations (27). In the Hertzian small-strain framework used to map indentation to deformation, validity improves at smaller δ/R ; the inclusion of 100–400 μm therefore anchors the analysis in a regime closer to Hertz’s assumptions, whereas the higher depths (700–1400 μm) intentionally probe departures from ideal half-space behaviour (17; 32). For a slab on a rigid support, finite-thickness stiffening grows with a/h ; by sampling δ over nearly 1.2 decades, it is possible to identify linear-regime/yield-plateau intervals where $G'(\omega)$ is approximately constant and geometry-invariant, and to diagnose thickness effects when they arise (5; 35).

For comparison across samples and tip types, a simple engineering indentation strain is reported, defined as

$$\epsilon = \frac{\delta}{h}, \quad (2.16)$$

where δ is the indentation depth and $h = 2\text{ mm}$ the sample height. Thus, the selected depths correspond to $\epsilon = 0.05, 0.10, 0.15, 0.20, 0.35, 0.50$, and 0.70 , respectively. This nondimensionalisation is useful for plotting moduli vs. strain and comparing datasets across geometries, even though the local strain field beneath a spherical or conical indenter is nonuniform and governed by contact mechanics (17; 32). In this study, the log-spaced depths ensure that i-Rheo Squeeze pipeline samples the regimes most informative for broadband $G'(\omega)$ and $G''(\omega)$: shallow indentations support the Hertzian mapping $\Lambda(\delta)$ and yield high-frequency content with good phase fidelity, while deeper indentations interrogate potential thickness-induced stiffening and help confirm the yield plateau used for cross-geometry consistency checks (35; 2).

2.9 Whittaker smoothing: definition, properties, and why it is suitable to try in this study

Whittaker–Henderson smoothing is a penalized least-squares method that estimates a smooth signal $\mathbf{z} = \{z_i\}_{i=1}^N$ from noisy observations $\mathbf{y} = \{y_i\}$ by balancing fidelity to the data and smoothness of the estimate. In its standard discrete form with equally spaced samples, \mathbf{z} is obtained by solving

$$\min_{\mathbf{z}} \sum_{i=1}^N w_i (y_i - z_i)^2 + \lambda \|\mathbf{D}^{(p)} \mathbf{z}\|_2^2, \quad (2.17)$$

where $w_i \geq 0$ are optional data weights, $\mathbf{D}^{(p)}$ is the p -th order difference operator (typically $p = 2$, i.e., a second-difference penalty), and $\lambda > 0$ is the smoothing parameter that controls curvature suppression (42; 13; 6). The normal equations are linear and sparse,

$$(\mathbf{W} + \lambda(\mathbf{D}^{(p)})^\top \mathbf{D}^{(p)}) \mathbf{z} = \mathbf{W} \mathbf{y}, \quad (2.18)$$

so \mathbf{z} is found rapidly via banded solvers, with explicit extrapolation at the ends handled by the structure of $\mathbf{D}^{(p)}$ (no ad-hoc filtering passes). For uniformly sampled data, the method is equivalent to applying a zero-phase, linear smoother with a known frequency response; for $p = 2$,

$$H(\omega) = \frac{1}{(1 + \lambda(2 - 2 \cos \omega)^2)^2}, \quad (2.19)$$

which behaves as a low-pass filter that preserves long-wavelength trends while attenuating high-frequency noise (6).

The approach generalises naturally to weighted and robust variants (iteratively reweighted least squares), handles missing points, and extends to irregular grids after reparameterisation (8). In the indentation-based i-Rheo pipeline, the inputs are the force $F(t)$ and the geometry-aware deformation $\Lambda(t)$ derived from indentation. Both signals are finite-length, time-domain records that feed a Fourier transform; small high-frequency perturbations (sensor noise, electrical pick-up, quantisation) can disproportionately corrupt phase and thus bias $G''(\omega)$. Whittaker smoothing is attractive here because: (i) it is model-free and does not impose a mechanistic rheology model; (ii) it offers a single, physically interpretable smoothness knob λ to trade off noise suppression against detail preservation; (iii) it is global and zero-phase (no causal lag), avoiding the phase shifts introduced by many recursive filters; and (iv) it is computationally lightweight, solving a banded linear system once per waveform—compatible with interactive use in the Streamlit app (42; 6). From a signal-processing viewpoint, applying Whittaker smoothing to $F(t)$ and $\Lambda(t)$ before the analytical Fourier transform should improve SNR, reduce truncation artefacts due to small irregularities, and stabilise the high- ω tail where G'' is most sensitive—hence it is worth testing as a denoising candidate in the pre-processing stage (6; 7).

In this study, Whittaker smoothing was therefore evaluated on the raw force and transformed indentation signals prior to computing $G^*(\omega) = \hat{F}(\omega)/\hat{\Lambda}(\omega)$, with $p = 2$ and λ spanning several decades to explore the bias–variance trade-off. The rationale—grounded in the properties above—was that a mild curvature penalty could suppress measurement noise without erasing the physically meaningful early-time structure that encodes the high-frequency modulus (9; 35). (As discussed later in the Results & Discussion, overly large λ values can over-attenuate phase content and underestimate G'' , highlighting the need for conservative tuning.)

Chapter 3: Results and Discussion

3.1 Program and Web Application

The program, developed in Python and hosted on a dedicated service server as stated in Section 2.6, is designed to compute the frequency-dependent viscoelastic moduli of materials by evaluating the ratio between the Fourier transforms of time-dependent force and indentation signals. This approach allows the software to analyse stress relaxation measurements performed with any generic indenter, supporting four different tip types—spherical, cylindrical, conical, and four-sided pyramid—with the relevant geometric parameters (e.g., diameter for spherical and cylindrical tips, additional cone angle or face angle parameters for conical and pyramid tips). The system is accessible via a web interface, enabling straightforward user interaction without the need for local installation. In practical use, the raw input

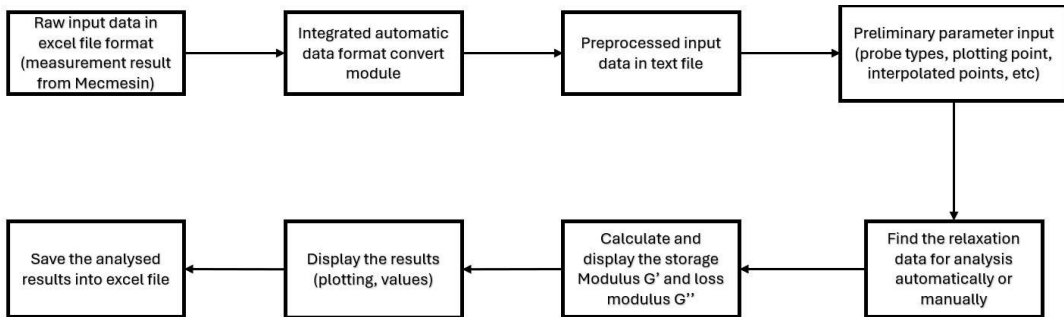


Figure 3.1: Block Diagram of the program

data is typically obtained from a Mecmesin OmniTest 2.5 testing machine and exported in Excel format. Such raw files often contain scattered and unstructured data, with relevant measurements spread across multiple sheets and intermixed with unnecessary metadata or calibration records. To address this, an automatic data format conversion module is integrated into the program. When raw data from Mecmesin machines is passed through this module, it automatically identifies and extracts only the essential components—namely the force and indentation values—needed for modulus calculation. Importantly, the original numerical values of force and indentation are preserved exactly during this process to maintain data integrity.

Once extracted, the cleaned data is converted into a lightweight plain-text file containing only the key parameters arranged in a consistent, algorithm-ready format:

```
{time [s], force [N], indentation [m]}
```

This structured format ensures rapid loading into the core algorithm for Fourier-transform processing, while significantly reducing file size and eliminating unnecessary overhead. By automating the formatting step, the program not only improves workflow efficiency but also minimises the potential for user error during manual preprocessing, making the system robust and accessible for a wide range of users in viscoelastic characterisation. The next module focuses on selecting the key parameters required for processing the output results. This

interface provides the user with the ability to specify the type of indenter used during the experimental setup, along with its corresponding geometric parameters. For spherical and cylindrical indenters, this includes the tip radius (or diameter), while for conical or four-sided pyramid tips, the relevant angular parameters are also available for input. These values are essential for correctly applying the appropriate Hertzian or related contact mechanics model during modulus calculation.

In addition to geometric specifications, the module allows the user to set the Poisson's ratio of the tested material, which is typically assumed to be 0.5 as stated in Section 2.5 for incompressible elastomers such as PDMS. Accurate input of these parameters ensures that the force-indentation data is correctly transformed into viscoelastic moduli, accounting for both the tip geometry and the intrinsic mechanical behaviour of the material. By integrating these settings into a dedicated module, the program streamlines the data analysis process, ensures model-parameter consistency, and provides flexibility for testing a variety of indenter types and materials without modifying the core algorithm. This module contains the algorithm

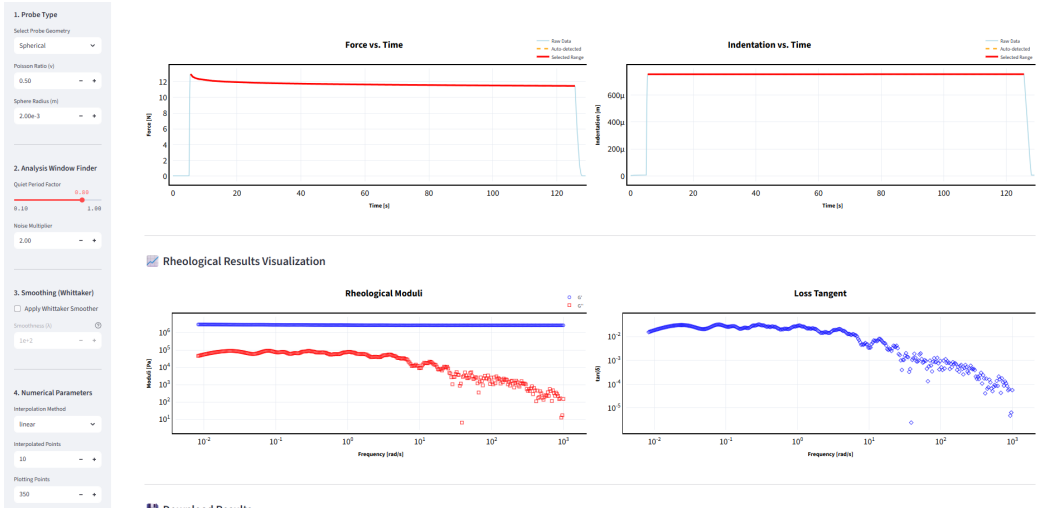


Figure 3.2: Block Diagram of the program

responsible for identifying the analysis range within the input dataset for both the force and indentation signals. Once a step-indentation measurement is loaded, the program displays the time evolution of force and indentation in the upper section of the application's front panel. Only the force relaxation phase is analysed, and this section is first detected automatically by the program and highlighted in red on both the force and indentation plots in Figure 3.2.

The automatic detection process begins by iterating through the force data to locate the start index, which corresponds to the maximum force value recorded. Once identified, this index is mapped to the time axis. From this start point, the program scans through the indentation data, calculating the difference between consecutive values. The end index is defined as the first point where this difference is non-zero, indicating the onset of indenter retraction. Since real experimental data inevitably contains noise—caused by factors such as mechanical vibrations, sensor resolution limits, or environmental fluctuations—the idealised detection approach can fail in some cases. To address this, the algorithm incorporates a noise threshold to ensure the process is not disrupted by minor fluctuations in the relaxation data.

The procedure for defining this threshold is as follows:

Noise estimation: The algorithm examines the indentation data during a pre-indentation “quiet period” and calculates the standard deviation of the changes in indentation. This value represents the typical noise magnitude in the measurement system.

Threshold calculation: The noise level is multiplied by a user-defined noise multiplier (default = 5.0) to generate the stationary threshold. Any indentation change smaller than this threshold is treated as noise, while any change larger is considered a real displacement event.

End-of-relaxation detection: Starting from the peak force, the code steps forward through the dataset point by point, checking the change in indentation at each step. The first instance where this change exceeds the stationary threshold marks the end index, indicating that the indenter has started to retract.

By combining peak force detection with noise-aware thresholding, the module can reliably identify the start and end points of the relaxation phase, producing an optimised analysis window for accurate modulus calculation.

While the automatic detection algorithm for identifying the start and end points of the relaxation phase generally works well, real experimental data often presents additional challenges. In some cases, even with an appropriately set noise threshold, the auto-detection may fail to capture the correct analysis range. To address these situations, the program includes Manual Adjustment Controls, allowing the user to fine-tune each index manually for maximum accuracy.

This flexibility is essential because the Fourier transform calculation is highly sensitive to the selected input range. Including even a small number of irrelevant data points—either from before the true start of relaxation or after it has ended—can introduce substantial errors into the computed viscoelastic moduli.

Two adjustment methods are available:

Offset Inputs – These fields enable precise numerical modification of the automatically detected start and end points. For example, if the start point is detected five data points too late, entering “-5” in the Start Offset box will shift it earlier by exactly five points; this will overwrite the automatically detected start index.

Manual Sliders (Start Index, End Index) – These provide a visual and interactive way to redefine the analysis window. By dragging the sliders, the user can directly select the start and end indices of the relaxation phase on the plotted data. This approach is especially useful when the auto-detection is significantly inaccurate or when a noise spike misleads the algorithm. By manually repositioning the sliders, the user can exclude problematic segments and define a clean, representative window for analysis. The real-time visual feedback ensures the selected range is exactly what the user intends to analyse.

By combining automated detection with these manual override tools, the program offers both speed and precision, ensuring that the final analysis window is optimised for the highest possible accuracy in modulus calculations. The next module involves selecting the numerical parameters that govern the analysis process once an appropriate analysis window has been defined. These settings directly influence both the accuracy and efficiency of the viscoelastic modulus calculation.

The Interpolation Method parameter determines the mathematical algorithm—either linear or cubic—used to generate a continuous function from the discrete, time-stamped force and indentation data points. This interpolation is essential because the Fourier transform requires evenly spaced data, whereas experimental measurements are often irregularly sampled or contain slight timing inconsistencies.

Once interpolated, the data is virtually oversampled to a higher resolution defined by the Interpolated Points parameter. This step is critical: by increasing the density of data points before applying the Fourier transform Section 2.4, the program reduces the risk of aliasing and spectral leakage, both of which can distort the calculated moduli, especially at higher frequencies. High-resolution re-sampling ensures that the transform accurately captures the true frequency content of the relaxation signal, enabling reliable modulus estimation over a broad frequency range. In essence, this virtual oversampling simulates the benefits of collecting more data in the experiment itself—without physically re-running the test—while preserving the original measurement’s physical meaning.

The Plotting Points parameter is a separate, purely visual control. It specifies the number of frequency points at which the final G' and G'' values are displayed. This ensures that the resulting graphs are smooth and interpretable, while avoiding the unnecessary computational cost of plotting an excessively dense frequency grid.

Once the analysis window is defined, the program applies a multi-stage computational procedure - based on the i-Rheo framework from Section 2.4 - to convert the raw, time-domain indentation data into accurate, frequency-dependent viscoelastic moduli. This process integrates physical modelling, numerical signal enhancement, and a specialised Fourier transform to ensure that the extracted storage and loss moduli faithfully represent the material’s behaviour over a broad frequency range. The final step computes the complex shear modulus from the ratio of the two spectra (35):

$$G^*(\omega) = \frac{\hat{F}(\omega)}{\hat{\Lambda}(\omega)}. \quad (3.1)$$

Here, $G^*(\omega)$ represents the total viscoelastic response, which is then decomposed into:

Storage Modulus $G'(\omega)$: the real part of $G^*(\omega)$, representing the elastic energy stored per cycle.

Loss Modulus $G''(\omega)$: the imaginary part of $G^*(\omega)$, representing the viscous energy dissipated per cycle.

After the computation process, the resulting ω , G' , G'' , and $\tan(\delta)$ are plotted and clearly displayed in the graphs located in the lower section of the application. At the same time, the program calculates the average value of G' within the defined analysis window, providing a key numerical output for subsequent interpretation and discussion.

These results constitute the primary output dataset of the program and are essential for the next stages of analysis. For ease of use and further processing, the output is saved as an Excel file, formatted with the following column order:

```
{frequency [rad/s], G' [Pa], G'' [Pa]}
```

This export format ensures compatibility with statistical tools, data visualisation software, and reporting templates, enabling seamless integration of the computed viscoelastic parameters into the overall experimental workflow.

3.2 Domain host:

After the program was developed and validated for stability, it was deployed in a domain-hosted environment to allow global user access. The deployment utilised a service server running Nginx as a reverse proxy, enabling both domain-to-IP and IP-to-domain routing, with full HTTP-to-HTTPS redirection for secure access.

Step 1: Running the Streamlit App on the Server

The application was launched as a background process using:

```
nohup streamlit run app.py --server.address=0.0.0.0 \
--server.port=8502 --server.enableCORS=false \
--server.enableXsrfProtection=false > log_streamlit.txt 2>&1 &
```

This configuration ensures that the app listens on all network interfaces (0.0.0.0), disables CORS and XSSRF protections to allow Nginx to manage headers, and logs all output to log_streamlit.txt. Running in the background with nohup allows the app to persist after the terminal session is closed.

Step 2: Configuring Nginx as a Reverse Proxy

Next, a dedicated Nginx configuration file was created:

```
sudo nano /etc/nginx/sites-available/irheoglasgow
```

Sample reverse proxy configuration:

```
server {
    listen 80;
    server_name irheoglasgow.id.vn;
    client_max_body_size 200M;

    location / {
        proxy_pass http://localhost:8502;
        proxy_set_header Host $host;
        proxy_set_header X-Real-IP $remote_addr;
        proxy_set_header X-Forwarded-For $proxy_add_x_forwarded_for;
        proxy_set_header X-Forwarded-Proto $scheme;
    }
}
```

This setup ensures that requests to `http://irheoglasgow.id.vn` are transparently forwarded to the locally running Streamlit app on port 8502, with appropriate headers preserved for client information and protocol awareness. The configuration was enabled and verified:

```
sudo ln -s /etc/nginx/sites-available/irheglasgow  
/etc/nginx/sites-enabled/  
sudo nginx -t  
sudo systemctl reload nginx
```

Step 3: Enabling HTTPS with Certbot

To secure communications, Certbot was installed and configured:

```
sudo apt update  
sudo apt install certbot python3-certbot-nginx -y  
sudo certbot --nginx -d irheglasgow.id.vn
```

Certbot automatically obtained and installed an SSL/TLS certificate for the domain, with an option selected to redirect all HTTP traffic to HTTPS, ensuring end-to-end encryption.

Step 4: Configuring Streamlit for Reverse Proxy Operation

Lastly, to prevent Streamlit from modifying headers needed by Nginx, the following configuration was added to `~/.streamlit/config.toml`:

```
[server]  
enableCORS = false  
enableXsrfProtection = false  
headless = true  
port = 8502
```

This ensured smooth interaction between Streamlit and Nginx, avoiding conflicts in header handling.

3.3 Experimental Setup for Data Acquisition

The raw data acquisition process for program input was carried out on PDMS samples prepared at mixing ratios of 5:1, 10:1, and 20:1 as mentioned in Section 2.7. Measurements were performed using a Mecmesin Omnitest 2.5 testing machine, with the VectorPro software interfacing directly to control the instrument and record data.

Indentation depths were selected as 100, 200, 300, 400, 700, 1000, and 1400 µm for all samples (Section 2.8). These values were chosen following a logarithmic scale rather than uniform spacing to ensure that both low-depth and high-depth deformation regimes were adequately captured. Logarithmic spacing allows for higher resolution in the small indentation range—where material stiffness and viscoelastic behaviour can change rapidly—while still sampling adequately at larger depths without unnecessarily increasing the total number of test points. This approach optimises experimental efficiency while maintaining sensitivity to both initial contact mechanics and deeper penetration responses (17; 26).

In addition to these baseline indentations, extra depths were introduced for specific sample-indenter combinations to refine the analysis in the linear regime and yield plateau regions determined from preliminary trials:

- PDMS 5:1 - Additional indentations at 450, 500, 650, and 750 μm for cylindrical indenters (4 mm and 8 mm) and spherical indenters (4 mm).
- PDMS 10:1 - Additional indentations at 250 and 350 μm for cylindrical indenters (4 mm and 8 mm) and spherical indenters (4 mm).
- PDMS 20:1 - Additional indentations at 220, 250, and 350 μm for cylindrical indenters (4 mm and 8 mm) and spherical indenters (4 mm).

These supplementary depths were strategically selected to provide higher measurement density in regions where modulus values exhibited minimal variation with increasing indentation -allowing more precise determination of the viscoelastic moduli and confirmation of plateau stability. By increasing resolution in these regions, subtle deviations or transitions could be detected, improving the robustness of the modulus evaluation. Throughout all experiments, the ambient temperature was carefully monitored and found to remain between 22.8 $^{\circ}\text{C}$ and 25 $^{\circ}\text{C}$, minimising temperature-induced variability in the PDMS mechanical response.

3.4 Investigation of the linearity and stiffness of PDMS samples (5:1, 10:1, and 20:1).

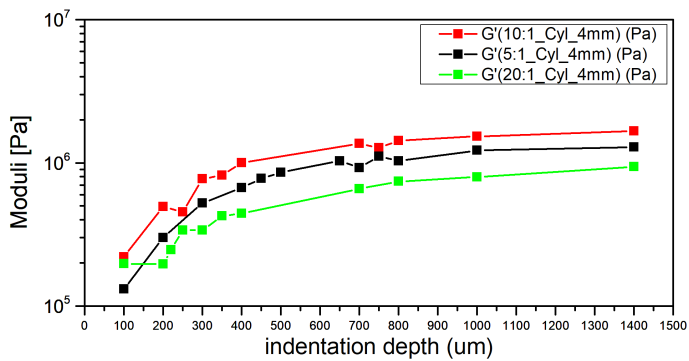


Figure 3.3: Average storage modulus G' versus indentation depth of each PDMS sample (5:1, 10:1, 20:1) using a cylindrical indenter with 4mm in diameter.

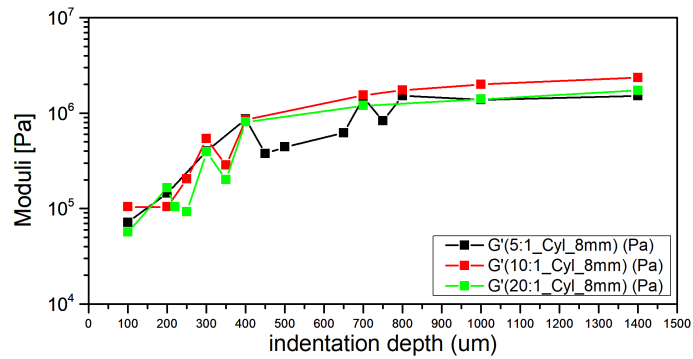


Figure 3.4: Average storage modulus G' versus indentation depth of each PDMS sample (5:1, 10:1, 20:1) using a cylindrical indenter with 8mm in diameter.

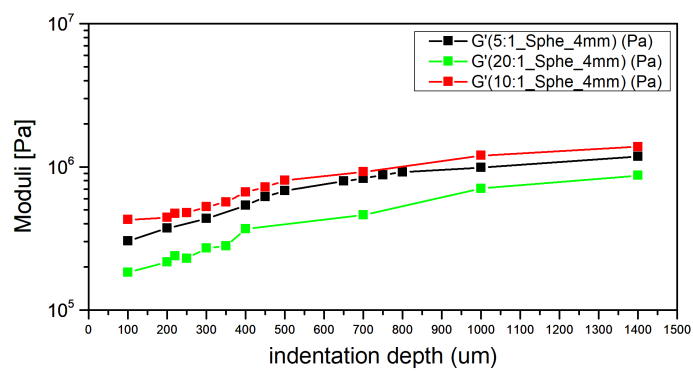


Figure 3.5: Average storage modulus G' versus indentation depth of each PDMS sample (5:1, 10:1, 20:1) using a spherical indenter with 4mm in diameter.

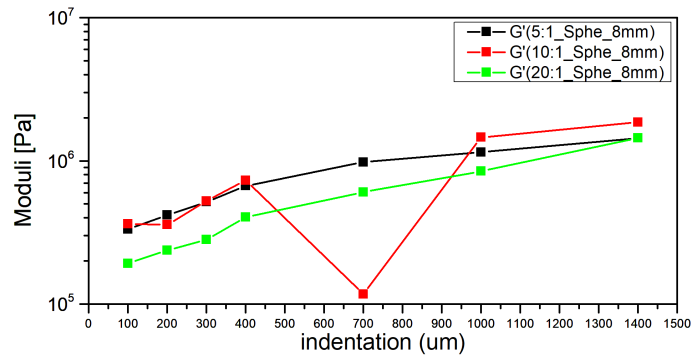


Figure 3.6: Average storage modulus G' versus indentation depth of each PDMS sample (5:1, 10:1, 20:1) using a spherical indenter with 8mm in diameter.

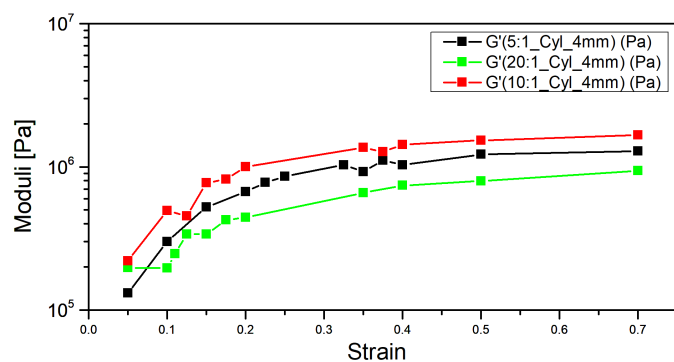


Figure 3.7: Average storage modulus G' versus strain of each PDMS sample (5:1, 10:1, 20:1) using a cylindrical indenter with 4mm in diameter.

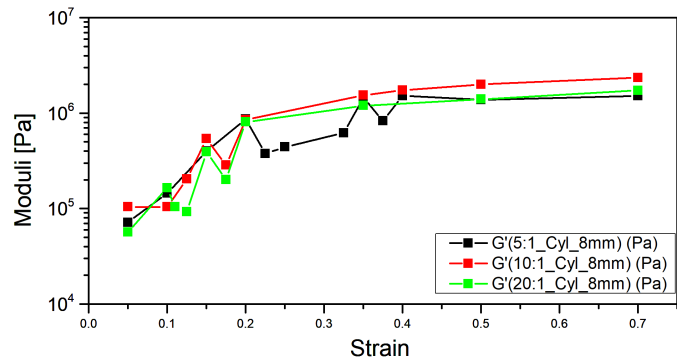


Figure 3.8: Average storage modulus G' versus strain of each PDMS sample (5:1, 10:1, 20:1) using a cylindrical indenter with 8mm in diameter.

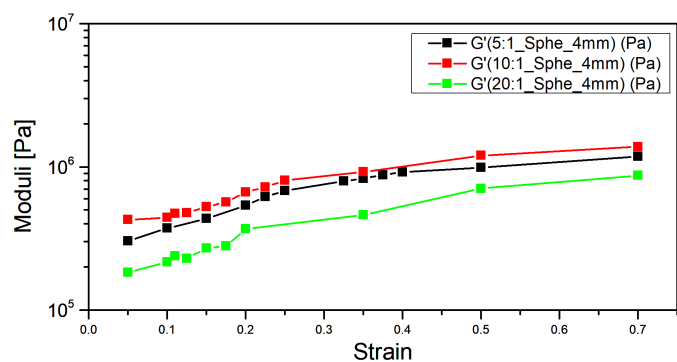


Figure 3.9: Average storage modulus G' versus strain of each PDMS sample (5:1, 10:1, 20:1) using a spherical indenter with 4mm in diameter.

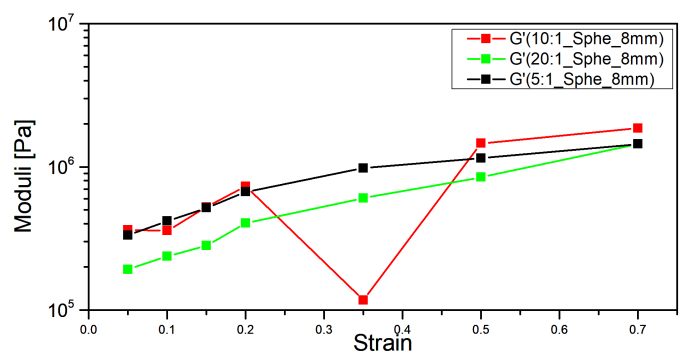


Figure 3.10: Average storage modulus G' versus strain of each PDMS sample (5:1, 10:1, 20:1) using a spherical indenter with 8mm in diameter.

From the modulus-indentation depth graphs as shown in Figures 3.3, 3.4, 3.5, and 3.6, a clear linear-like trend can be observed in which the storage modulus G' increases with increasing indentation depth. This behaviour reflects a typical strain-stiffening response of elastomeric networks such as PDMS, where greater deformation leads to polymer chain alignment and reduced configurational freedom, resulting in a higher resistance to further deformation (33). A similar tendency is expected in modulus-strain relationships as shown in Figures 3.7, 3.8, 3.9, and 3.10, as deeper indentation corresponds to larger local strains in the contact area. This progressive stiffening is consistent with the non-linear elastic regime described by Hertzian contact mechanics (Section 2.5 and by the finite-strain behaviour of crosslinked silicone elastomers (Section 2.7).

When assessing stiffness solely from G' , the results align partially with theoretical expectations. As predicted from crosslink density considerations, PDMS 20:1 is clearly the softest, exhibiting the lowest average G' across all indentation depths and indenter geometries, in agreement with the literature (18). This indicates that the developed program's Fourier-transform-based analysis yields reasonable and physically consistent results for the softer formulation. However, a notable and consistent anomaly arises for the stiffer formulations: theoretically from (Section 2.7), PDMS 5:1 should be the stiffest due to its highest curing agent ratio and corresponding highest crosslink density, yet in all datasets—across spherical and cylindrical indenters of both 4 mm and 8 mm diameter—PDMS 10:1 shows the highest average G' , while PDMS 5:1 is consistently lower.

Several plausible explanations can account for this deviation. First, PDMS 5:1 may have undergone softening during storage, as silicone elastomers can experience partial network degradation or plasticisation when exposed to ambient humidity, UV light, or thermal cycling, leading to a reduction in modulus over time (41; 22). Second, repeated indentations on the same surface location during testing could have induced mechanical fatigue or the Mullins effect, where permanent microstructural changes reduce the material's ability to recover its original stiffness (4), as notably, the data for 10:1 PDMS with the 8 mm spherical indenter exhibited a marked dip in G' around 700 μm before recovering at deeper indentations, suggesting a local heterogeneity in the sample as this anomaly contrasts with the smoother depth dependence in other datasets. Third, incomplete mixing of base and curing agent, or uneven curing, may have caused localised regions of lower crosslink density in the PDMS 5:1 samples, disproportionately affecting modulus measurements (29). Additionally, the much higher crosslink density of 5:1 PDMS can make it more brittle, and microcracking under repeated loading could reduce the effective modulus captured during quasi-static indentation (19).

3.5 Investigation of linear elasticity and yield plateau:

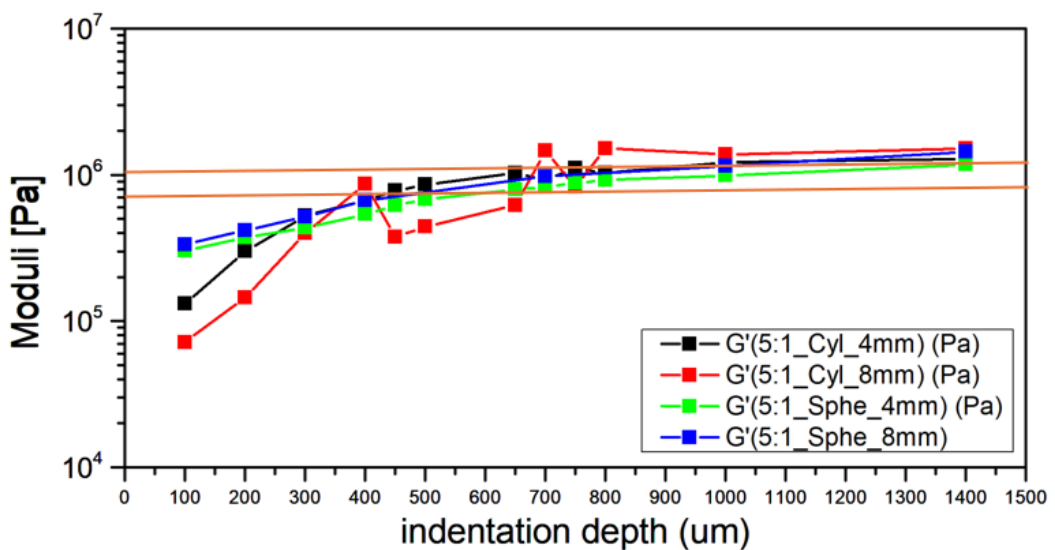


Figure 3.11: Average storage modulus G' versus indentation depth of PDMS sample 5:1 with spherical indenter with 4mm and 8mm in diameter and cylindrical indenter with 4mm and 8mm in diameter.

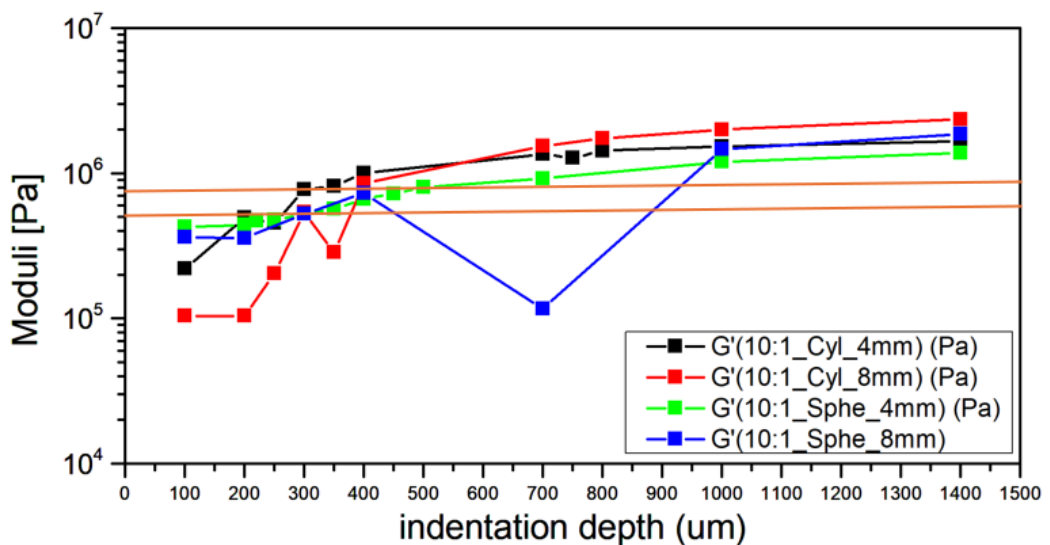


Figure 3.12: Average storage modulus G' versus indentation depth of PDMS sample 10:1 with spherical indenter with 4mm and 8mm in diameter and cylindrical indenter with 4mm and 8mm in diameter.

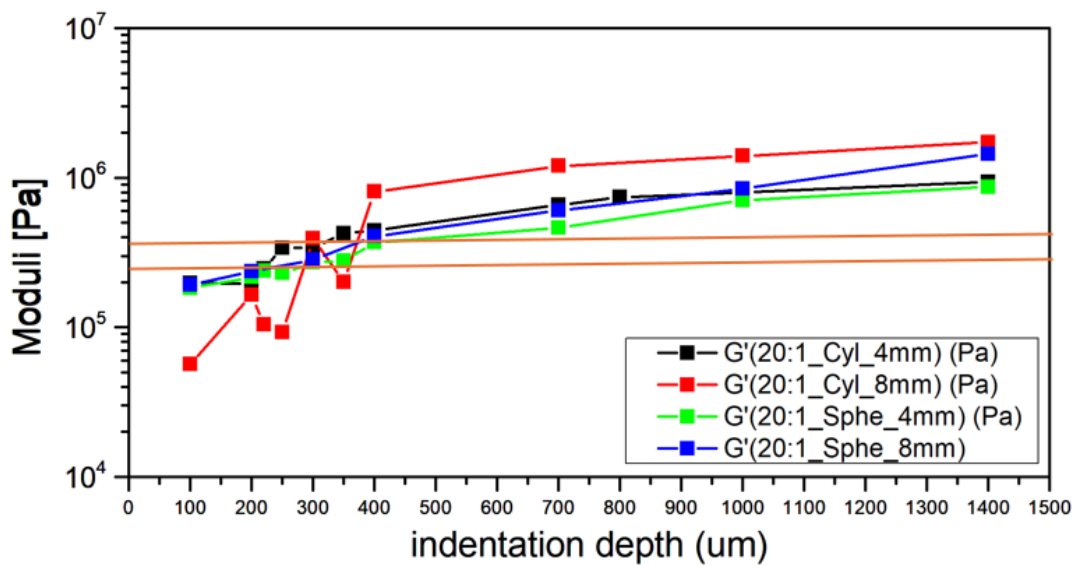


Figure 3.13: Average storage modulus G' versus indentation depth of PDMS sample 20:1 with spherical indenter with 4mm and 8mm in diameter and cylindrical indenter with 4mm and 8mm in diameter.

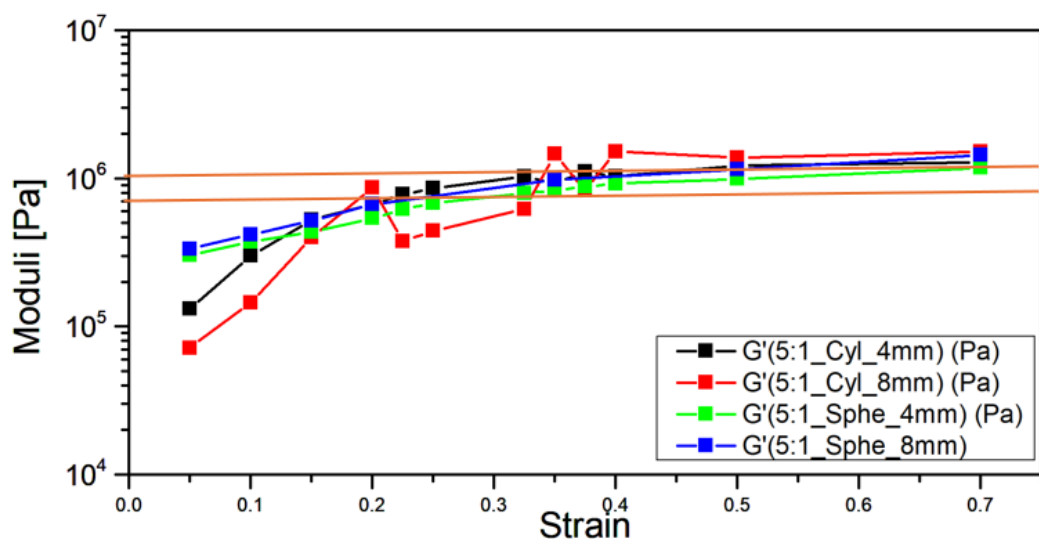


Figure 3.14: Average storage modulus G' versus strain of PDMS sample 5:1 with spherical indenter with 4mm and 8mm in diameter and cylindrical indenter with 4mm and 8mm in diameter.

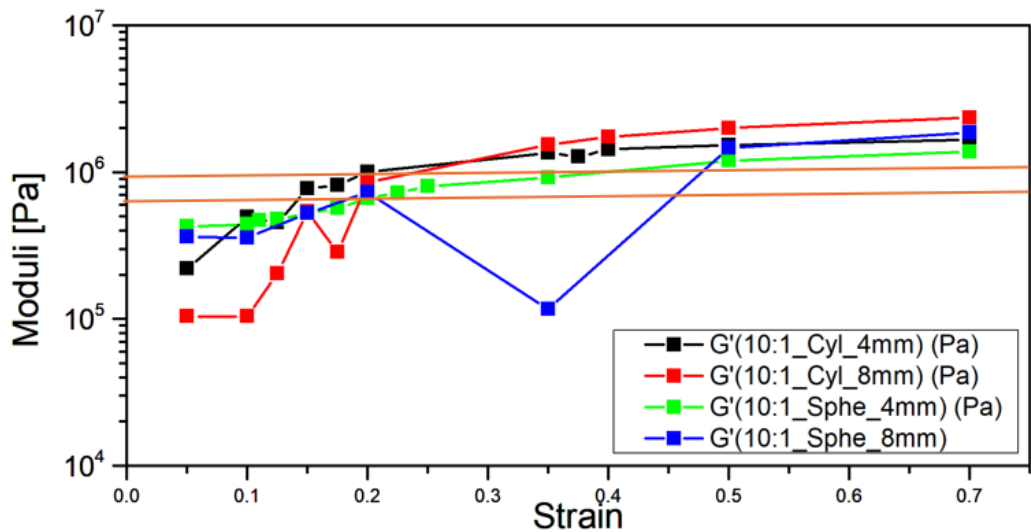


Figure 3.15: Average storage modulus G' versus strain of PDMS sample 10:1 with spherical indenter with 4mm and 8mm in diameter and cylindrical indenter with 4mm and 8mm in diameter.

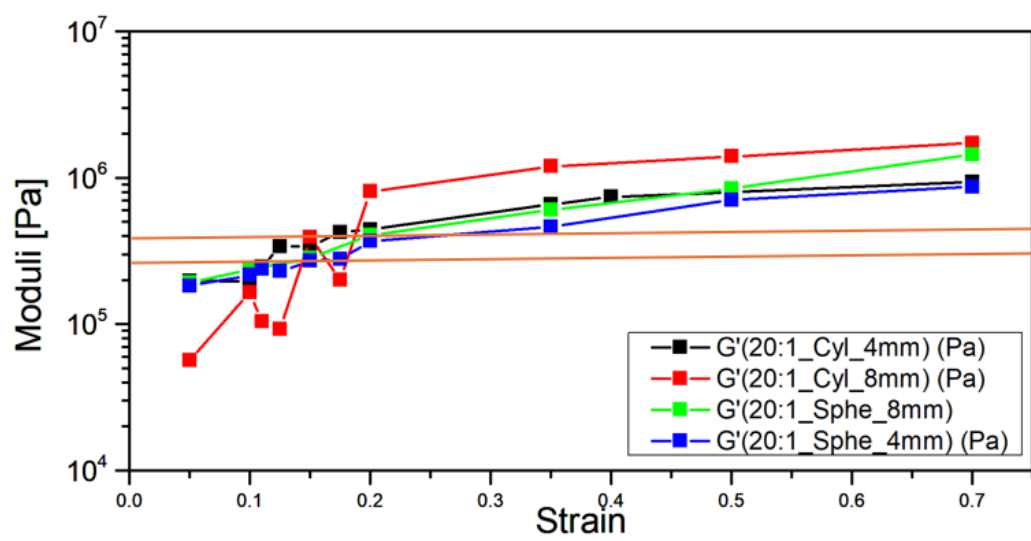


Figure 3.16: Average storage modulus G' versus strain of PDMS sample 20:1 with spherical indenter with 4mm and 8mm in diameter and cylindrical indenter with 4mm and 8mm in diameter.

From the plotted results shown in Figures 3.11, 3.12, 3.13, 3.14, 3.15, and 3.16, it is evident that for each PDMS formulation, there exists a specific range of indentation depths over which the measured storage modulus G' remains approximately constant. This constant region—highlighted by horizontal lines in the corresponding graphs—indicates the transition from the initial strain-stiffening behaviour into a regime of near-constant stiffness. For PDMS 5:1, G' remains within approximately 0.9–1.0 MPa between indentation depths of about 400–800 μm ; for PDMS 10:1, the plateau occurs around 0.7–1.0 MPa between 200–400 μm ; and for PDMS 20:1, the modulus is approximately 0.28–0.35 MPa between 200–400 μm , most prominently near 300 μm . The presence of such a plateau in G' can be interpreted as the linear elasticity regime, where the material's microstructure is deforming elastically without significant additional stiffening or softening, and the stress–strain relationship can be considered nearly linear. This range corresponds to the region before the onset of non-linear effects such as large-strain chain alignment, network rearrangement, or damage.

Following the linear elastic region, if the applied deformation continues to increase, the plateau can also be interpreted in the context of a yield plateau, where the material approaches the limit of purely elastic response and begins to transition toward irreversible or viscoelastic deformation. The valid stiffness value for each PDMS formulation should be pinpointed according to Section 2.7 and the indentation depth/strain threshold should be located beyond which the response is no longer purely elastic.

It is important to note that in this study, the experimental error in the plateau regions is relatively large, which may be attributed to setup-related issues discussed previously—such as small misalignments in the indenter–sample contact, local heterogeneity in the PDMS surface, and signal-to-noise limitations of the force/displacement acquisition system. Despite these factors, the identified plateau ranges still provide physically meaningful information: the measured G' values in these intervals are close to those expected from theoretical and literature-reported bulk modulus values for the respective PDMS formulations, thereby validating the experimental data as representative of the material's intrinsic stiffness within its linear elastic regime.

3.6 Investigation of the similarity in G' and G'' for each PDMS sample when using different indenter types and sizes:

From the comparative plots of G' and G'' for PDMS 5:1 (Figures 3.17), 10:1 (Figures 3.18), and 20:1 (Figures 3.19), it is evident that using different indenter geometries (spherical vs. cylindrical) and sizes (4 mm and 8 mm diameter) yields broadly consistent results within the valid indentation depth ranges for each formulation. The representative depth of 750 μm for PDMS 5:1 is well within the yield plateau of 400–800 μm . The representative depth of 300 μm for PDMS 10:1 is also within the valid range of 200–400 μm , and the same depth of 300 μm for PDMS 20:1 is also within its 200–400 μm plateau range. At these depths, the G' and G'' values measured show a lot of overlap across all types of indenters. The data points group together in a way that is consistent, rather than scattering randomly or diverging too much.

This visual consistency, observable directly from the graphs, indicates that the developed program processes force–time and indentation–time inputs robustly, independent of probe geometry and size, when operating within the valid deformation regime of the material. The underlying reason is that within the yield plateau, the material's response is dominated by bulk elastic–viscous properties rather than by localised surface effects or geometry-sensitive stress fields, so the Fourier-transform-based modulus extraction yields values that

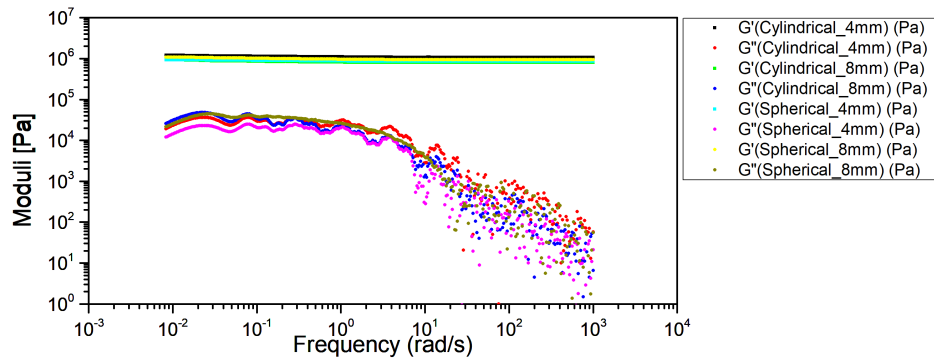


Figure 3.17: Plot of storage modulus G' and loss modulus G'' on the frequency domain of PDMS sample 5:1 using spherical indenter with 4mm and 8mm in diameter and cylindrical indenter with 4mm and 8mm in diameter and applying indentation depth of 750 μm .

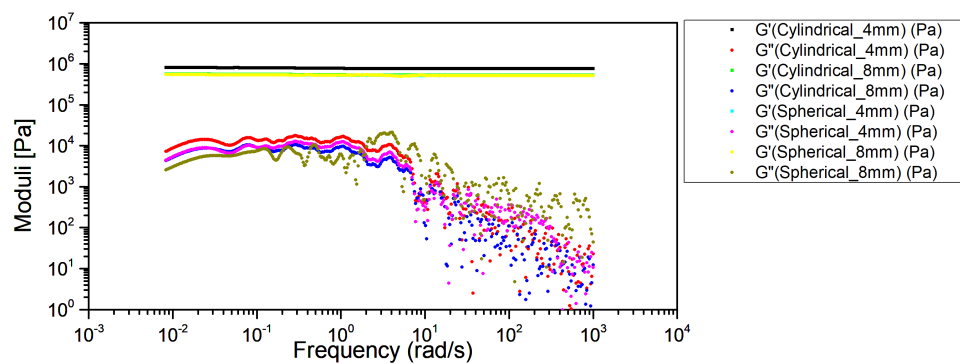


Figure 3.18: Plot of storage modulus G' and loss modulus G'' on the frequency domain of PDMS sample 10:1 using spherical indenter with 4mm and 8mm in diameter and cylindrical indenter with 4mm and 8mm in diameter and applying indentation depth of 300 μm .

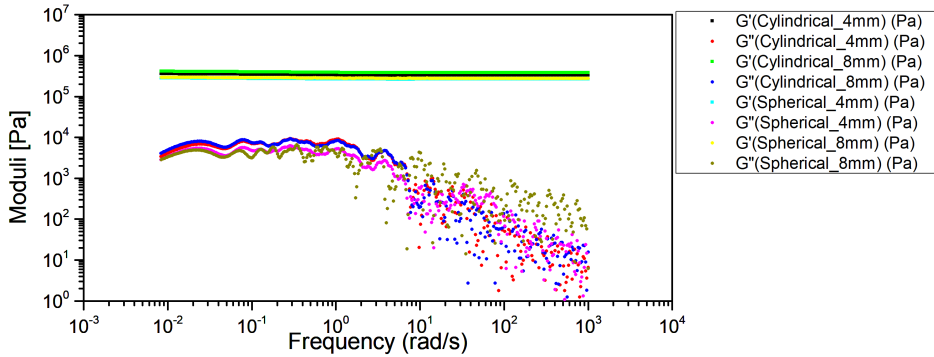


Figure 3.19: Plot of storage modulus G' and loss modulus G'' on the frequency domain of PDMS sample 10:1 using spherical indenter with 4mm and 8mm in diameter and cylindrical indenter with 4mm and 8mm in diameter and applying indentation depth of 300 μm

are geometry-invariant to a first approximation. Demonstrating that different probe configurations produce comparable moduli for the same sample type is a key validation objective of this study, as it confirms that the computational method isolates intrinsic material properties rather than artefacts of the measurement setup. This consistency strengthens the reliability of the developed analysis tool for broadband rheological characterisation, showing that it can be confidently applied across multiple indentation configurations without compromising the accuracy or comparability of G' and G'' measurements.

3.7 Investigation of the properties of each PDMS sample from G' and G'' when using different indenter types and sizes:

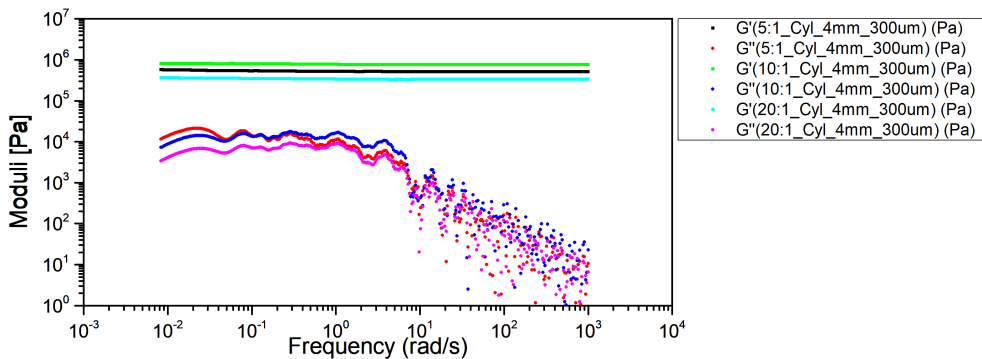


Figure 3.20: Plot of storage modulus G' and loss modulus G'' on the frequency domain of each PDMS sample (5:1, 10:1, 20:1) using cylindrical indenter with 4mm in diameter and applying indentation depth of 300 μm .

From the comparative plots illustrates in Figures 3.20, 3.21, 3.22, and 3.23 at a represen-

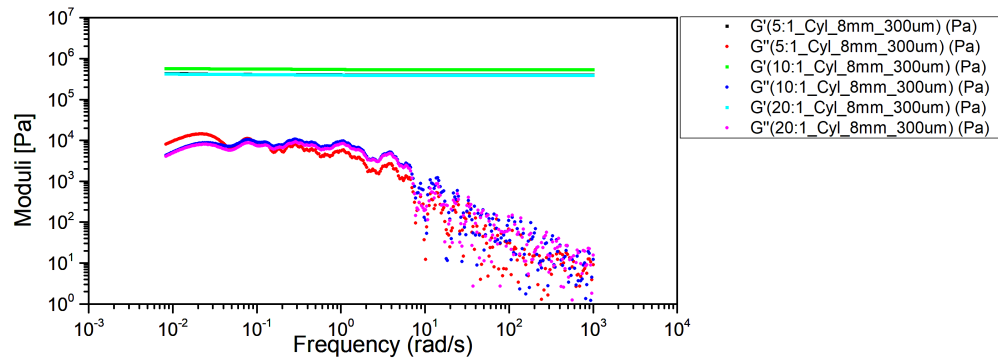


Figure 3.21: Plot of storage modulus G' and loss modulus G'' on the frequency domain of each PDMS sample (5:1, 10:1, 20:1) using cylindrical indenter with 8mm in diameter and applying indentation depth of 300 μ m.

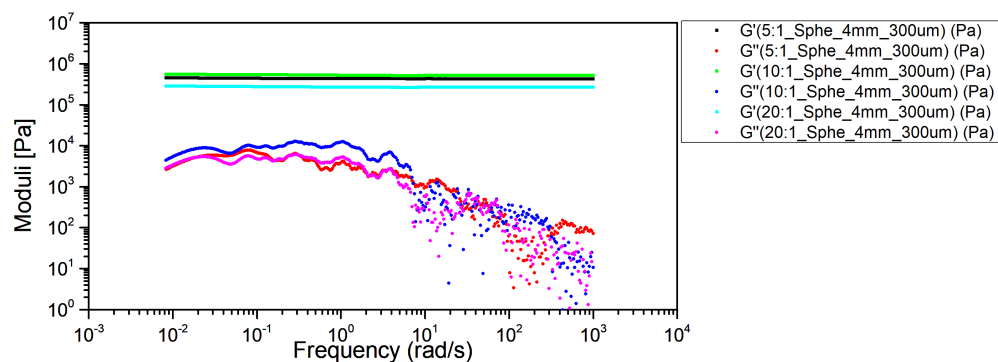


Figure 3.22: Plot of storage modulus G' and loss modulus G'' on the frequency domain of each PDMS sample (5:1, 10:1, 20:1) using spherical indenter with 4mm in diameter and applying indentation depth of 300 μ m.

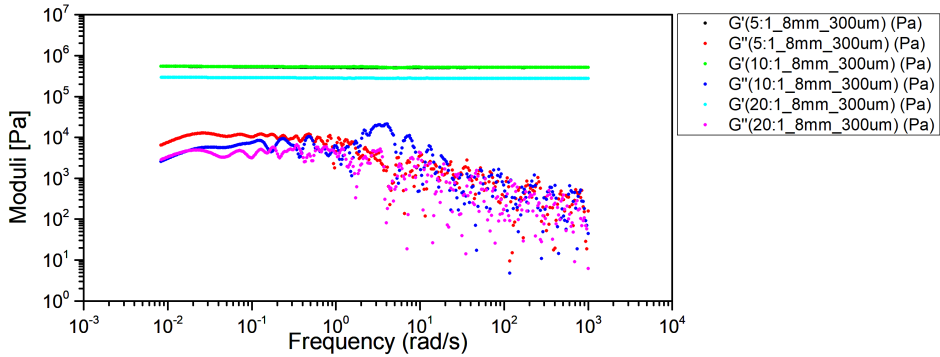


Figure 3.23: Plot of storage modulus G' and loss modulus G'' on the frequency domain of each PDMS sample (5:1, 10:1, 20:1) using spherical indenter with 8mm in diameter and applying indentation depth of 300 μm .

tative indentation depth of 300 μm for all indenter types, the storage modulus G' confirms the earlier observation that PDMS 20:1 is the softest formulation, while the stiffness ranking between PDMS 5:1 and 10:1 remains affected by the anomaly discussed previously. Examining the loss modulus G'' , the results follow the expected frequency-dependent behaviour for viscoelastic elastomers: G'' typically increases with angular frequency, reaching a broad maximum in the mid-frequency range (approximately 10–100 rad/s), which corresponds to the transition from predominantly elastic to more dissipative behaviour. At very high frequencies, G'' either levels off or decreases due to limited viscous dissipation as molecular segments cannot rearrange quickly enough. At low frequencies, G'' values are small (around 0.05–0.3 MPa), reflecting minimal energy loss in the fully relaxed state of the polymer network.

A notable feature in the current data is the onset of greater data dispersion in G'' around 10¹ rad/s. This is a well-recognised phenomenon in indentation rheology and other oscillatory techniques, arising from the fact that G'' is computed from relatively small phase shifts between force and displacement signals, which are inherently more sensitive to experimental noise and setup variability than G' . As frequency increases, any timing inaccuracies, sensor noise, or local sample heterogeneities can amplify scatter in the loss modulus measurements.

When looking at how crosslinking affects dissipation in different PDMS formulations, the data shows that PDMS 20:1 always has the lowest G'' values. PDMS 5:1 and PDMS 10:1 exhibit elevated and relatively similar G'' values, indicating comparable internal friction levels despite variations in nominal stiffness. This can be explained by how polymer chains move: in the highly crosslinked PDMS 5:1, the short chain segments between crosslinks can't move as much, which not only raises G' but also raises G'' by increasing internal friction during deformation. In the loosely crosslinked PDMS 20:1, the network has a lot of long, dangling chains that don't support weight. These free chains can move around more easily, but they don't add much to the dissipative friction in the elastic backbone, which lowers G'' . The intermediate PDMS 10:1 has a crosslink density that falls between these two extremes. In this dataset, its dissipation profile is similar to that of PDMS 5:1. Investigation of the application of the Whittaker smoothing filter for noise reduction in input data

3.8 Investigation of the application of the Whittaker smoothing filter for noise reduction in input data

The Whittaker–Henderson smoothing filter Section 2.9 was applied with the expectation of reducing noise in the input data - specifically in the raw force signal and the transformed indentation data - prior to the final Fourier-transform-based calculation of G' and G'' . The approach was tested on two out of three PDMS formulations (5:1 and 20:1) using the spherical 8 mm indenter, with indentation steps of 100, 200, 300, 400, 700, 1000, and 1400 μm , and smoothing parameters λ ranging from 10^2 to 10^{10} . Theoretically, the Whittaker filter is well-suited for noise reduction because it minimises the squared differences between the smoothed and original data while penalising large second differences, effectively acting as a low-pass filter that preserves long-wavelength trends while attenuating high-frequency noise. This is particularly relevant in indentation rheology, where high-frequency noise in the time domain can strongly affect the accuracy of frequency-domain modulus calculations.

However, the experimental results of PDMS 5:1 in Figures 3.24, 3.25, 3.26, 3.27, 3.28, 3.29, 3.30, and PDMS 20:1 in Figures 3.31, 3.32, 3.33, 3.34, 3.35, 3.36, 3.37 show that, in practice, the Whittaker filter did not deliver the expected benefits. For G' , almost no change was observed across smoothing levels because the storage modulus is largely determined by the amplitude of the force–indentation relationship, which was not significantly altered by the filtering. In contrast, G'' was severely affected: increasing the smoothing parameter λ progressively distorted the loss modulus curves, producing a steep downward slope and erasing characteristic features of the material’s dissipative response. This occurred because G'' is computed from the phase lag between force and indentation signals, and phase information is inherently sensitive to fine-scale variations in the data. Aggressive smoothing suppresses these subtle variations, effectively reducing or eliminating the measurable phase lag. This artificial phase reduction makes the material appear less viscous and more elastic than it truly is, leading to a substantial underestimation of G'' .

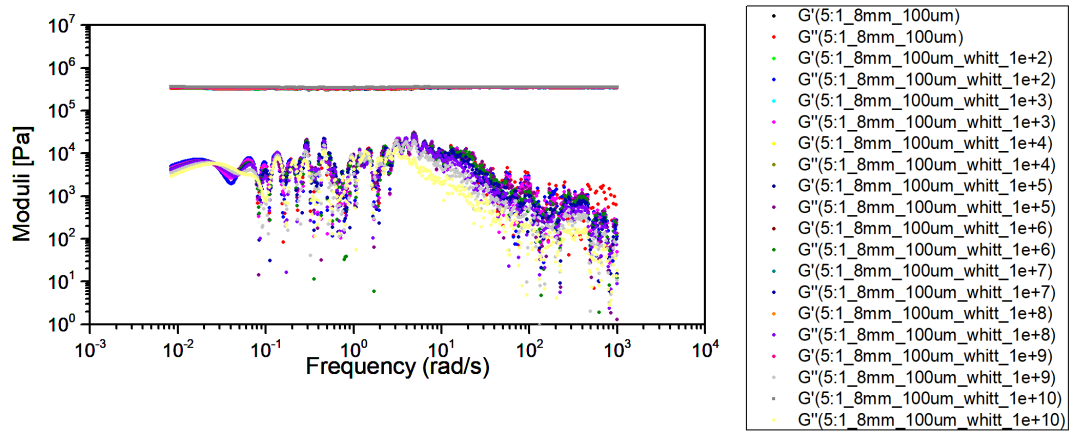


Figure 3.24: Plot of storage modulus G' and loss modulus G'' on the frequency domain of PDMS sample 5:1 using spherical indenter with 8mm in diameter and applying indentation depth of $100\text{ }\mu\text{m}$ with smoothing parameters λ ranging from 10^2 to 10^{10}

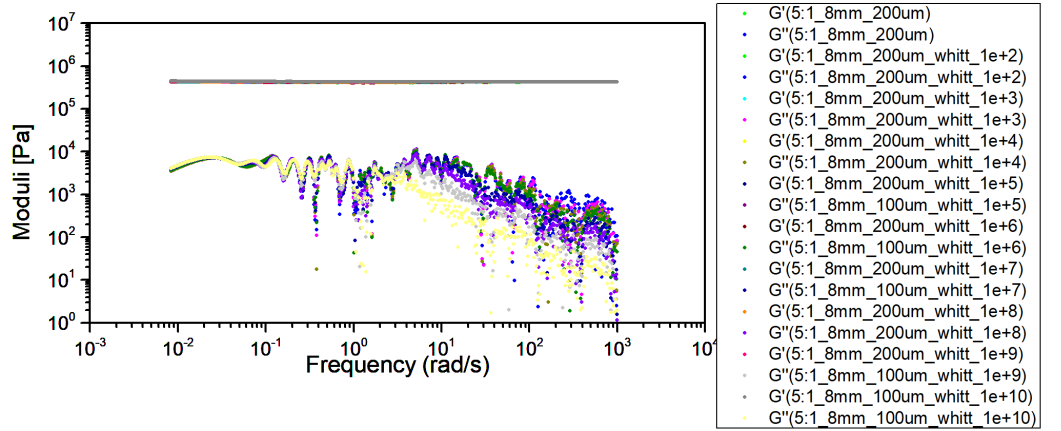


Figure 3.25: Plot of storage modulus G' and loss modulus G'' on the frequency domain of PDMS sample 5:1 using spherical indenter with 8mm in diameter and applying indentation depth of $200\text{ }\mu\text{m}$ with smoothing parameters λ ranging from 10^2 to 10^{10}

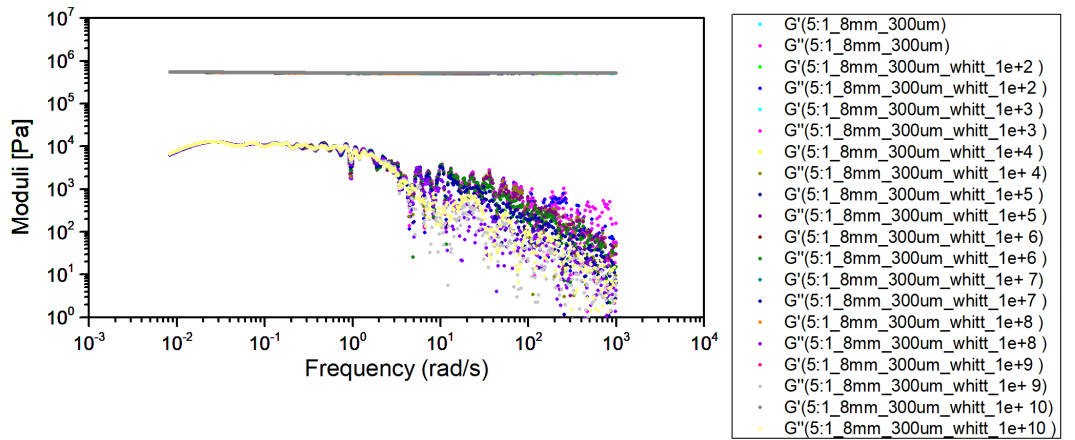


Figure 3.26: Plot of storage modulus G' and loss modulus G'' on the frequency domain of PDMS sample 5:1 using spherical indenter with 8mm in diameter and applying indentation depth of $300\text{ }\mu\text{m}$ with smoothing parameters λ ranging from 10^2 to 10^{10}

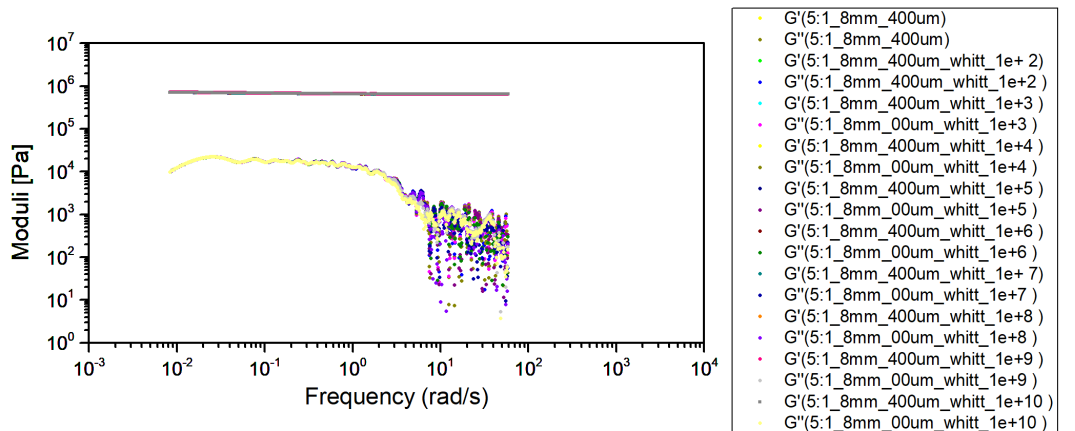


Figure 3.27: Plot of storage modulus G' and loss modulus G'' on the frequency domain of PDMS sample 5:1 using spherical indenter with 8mm in diameter and applying indentation depth of $400\text{ }\mu\text{m}$ with smoothing parameters λ ranging from 10^2 to 10^{10}

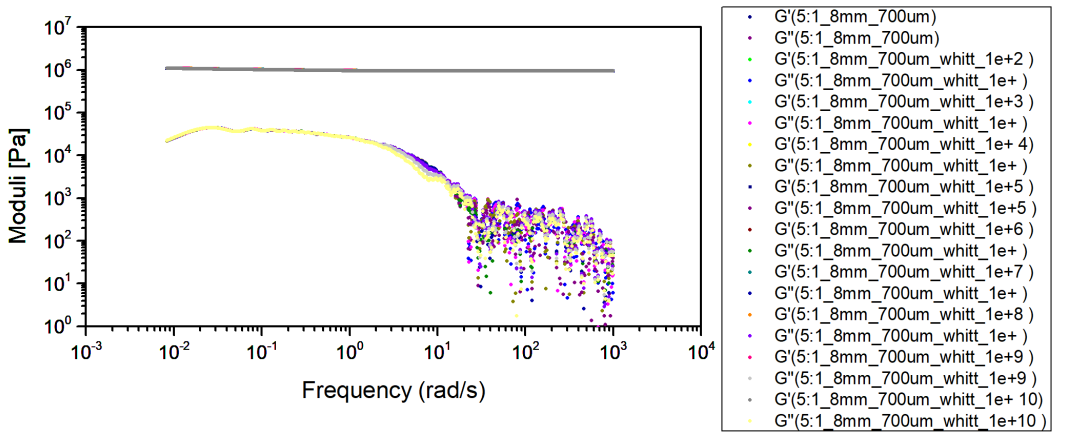


Figure 3.28: Plot of storage modulus G' and loss modulus G'' on the frequency domain of PDMS sample 5:1 using spherical indenter with 8mm in diameter and applying indentation depth of 700 μm with smoothing parameters λ ranging from 10^2 to 10^{10}

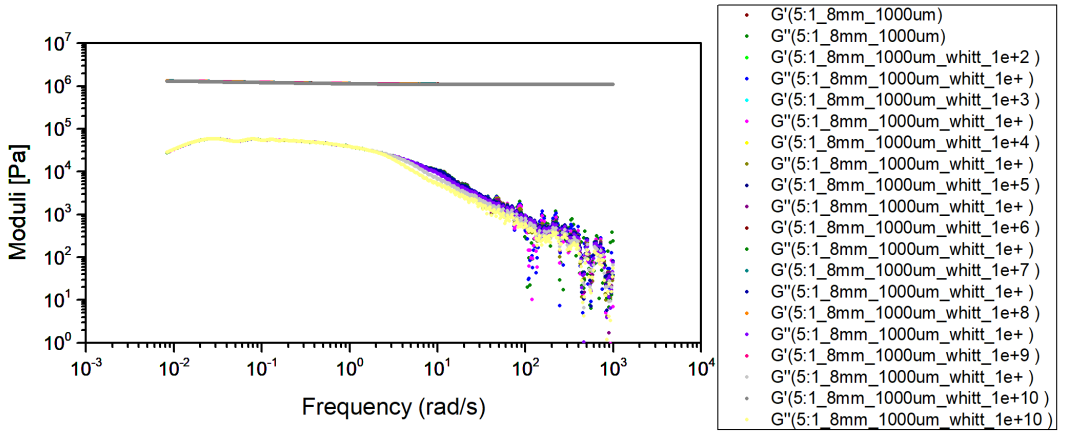


Figure 3.29: Plot of storage modulus G' and loss modulus G'' on the frequency domain of PDMS sample 5:1 using spherical indenter with 8mm in diameter and applying indentation depth of 1000 μm with smoothing parameters λ ranging from 10^2 to 10^{10}

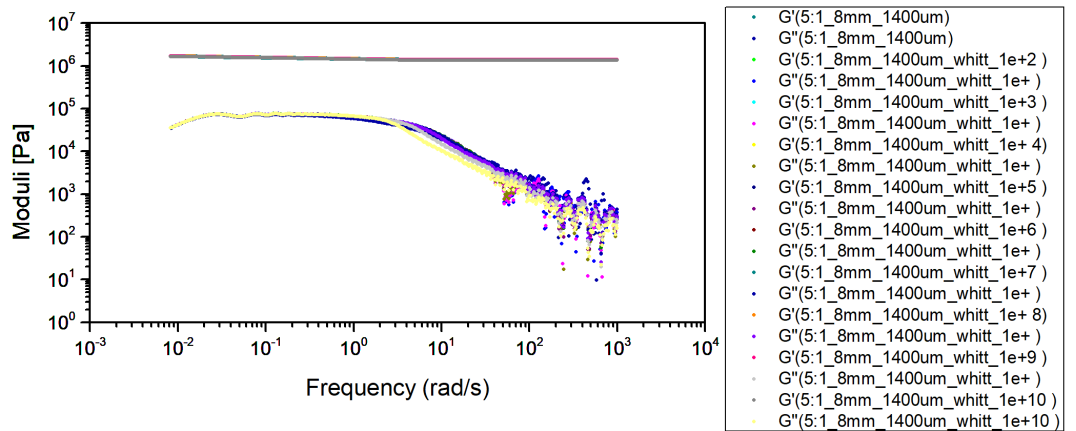


Figure 3.30: Plot of storage modulus G' and loss modulus G'' on the frequency domain of PDMS sample 5:1 using spherical indenter with 8mm in diameter and applying indentation depth of 1400 μm with smoothing parameters λ ranging from 10^2 to 10^{10}

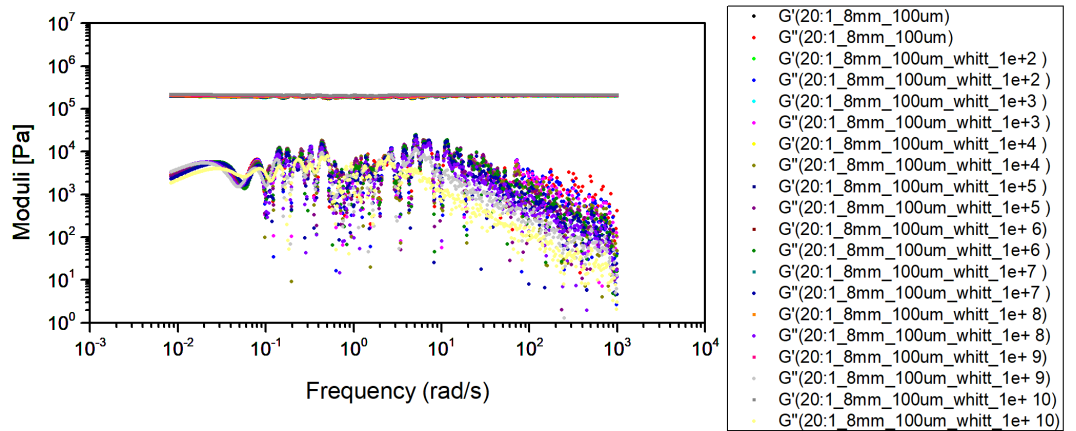


Figure 3.31: Plot of storage modulus G' and loss modulus G'' on the frequency domain of PDMS sample 20:1 using spherical indenter with 8mm in diameter and applying indentation depth of 100 μm with smoothing parameters λ ranging from 10^2 to 10^{10}

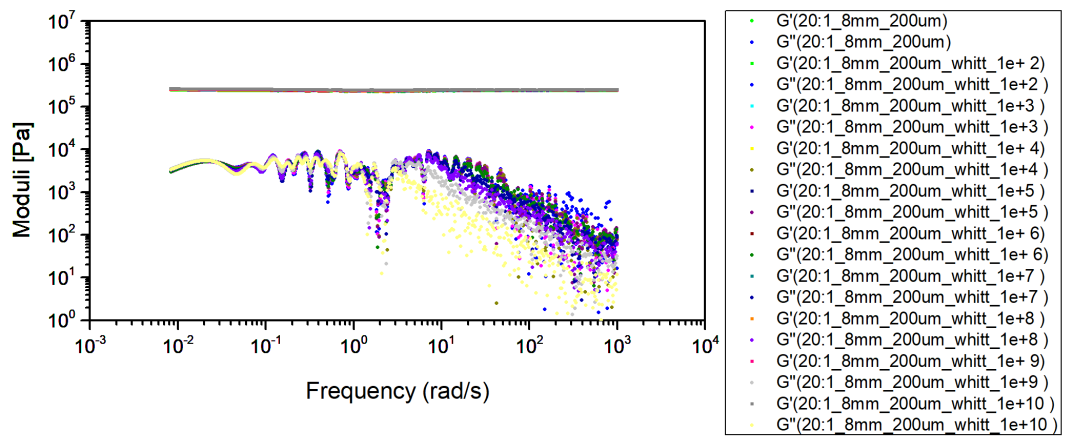


Figure 3.32: Plot of storage modulus G' and loss modulus G'' on the frequency domain of PDMS sample 20:1 using spherical indenter with 8mm in diameter and applying indentation depth of 200 μm with smoothing parameters λ ranging from 10^2 to 10^{10}

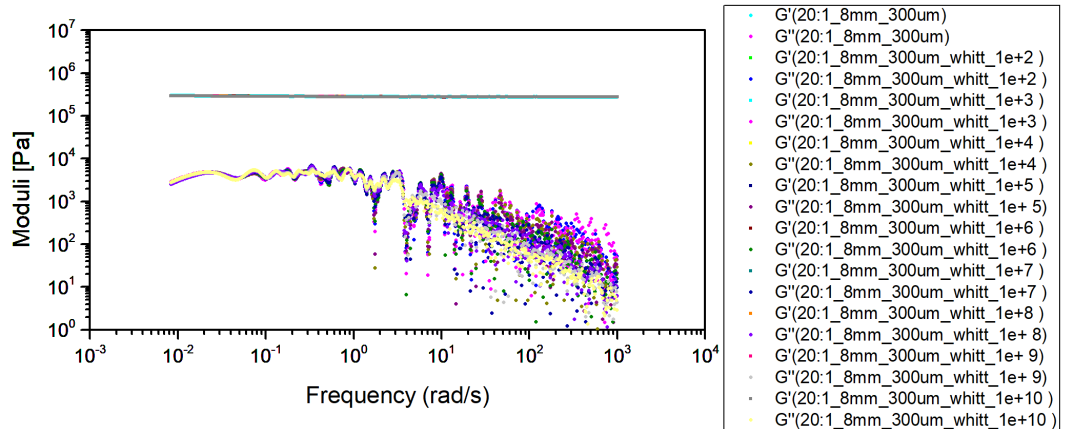


Figure 3.33: Plot of storage modulus G' and loss modulus G'' on the frequency domain of PDMS sample 20:1 using spherical indenter with 8mm in diameter and applying indentation depth of 300 μm with smoothing parameters λ ranging from 10^2 to 10^{10}

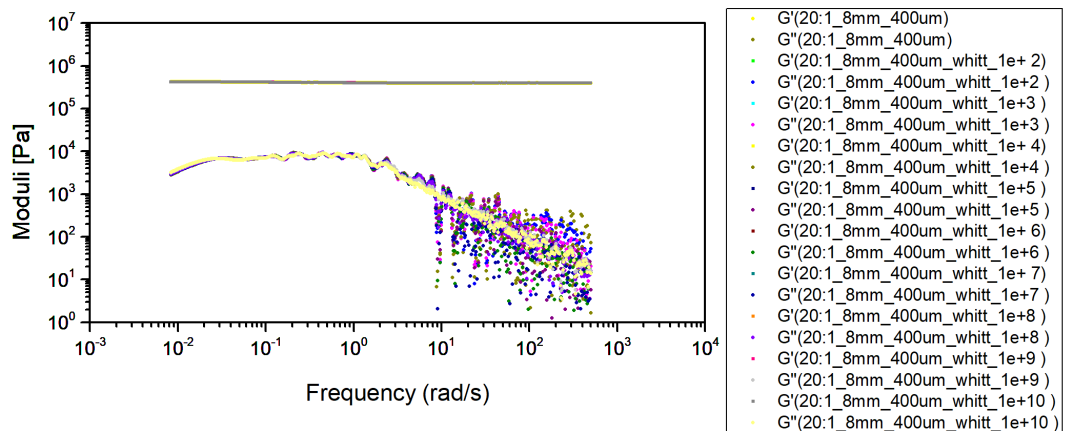


Figure 3.34: Plot of storage modulus G' and loss modulus G'' on the frequency domain of PDMS sample 20:1 using spherical indenter with 8mm in diameter and applying indentation depth of 400 μm with smoothing parameters λ ranging from 10^2 to 10^{10}

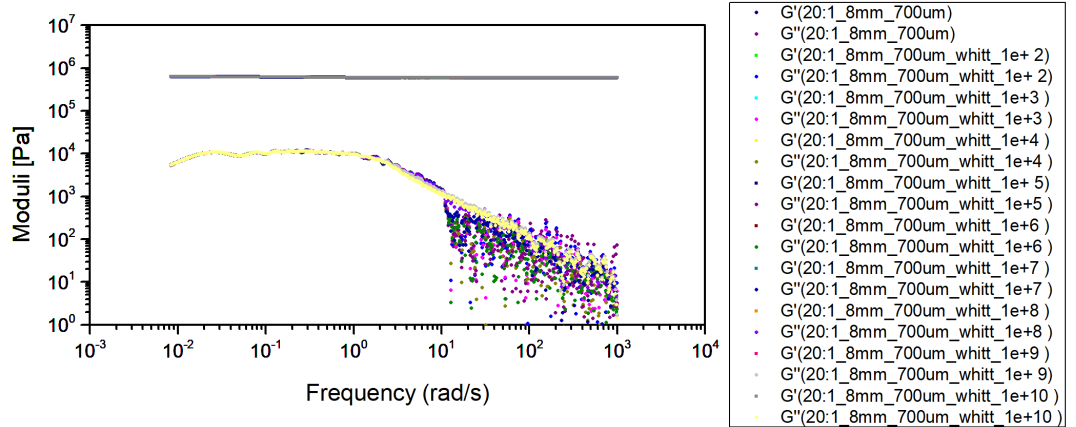


Figure 3.35: Plot of storage modulus G' and loss modulus G'' on the frequency domain of PDMS sample 20:1 using spherical indenter with 8mm in diameter and applying indentation depth of 700 μm with smoothing parameters λ ranging from 10^2 to 10^{10}

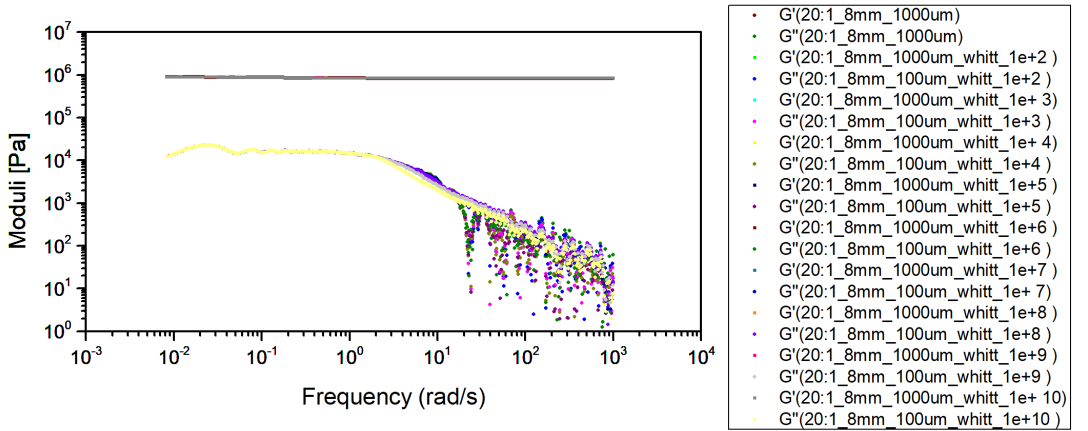


Figure 3.36: Plot of storage modulus G' and loss modulus G'' on the frequency domain of PDMS sample 20:1 using spherical indenter with 8mm in diameter and applying indentation depth of 1000 μm with smoothing parameters λ ranging from 10^2 to 10^{10}

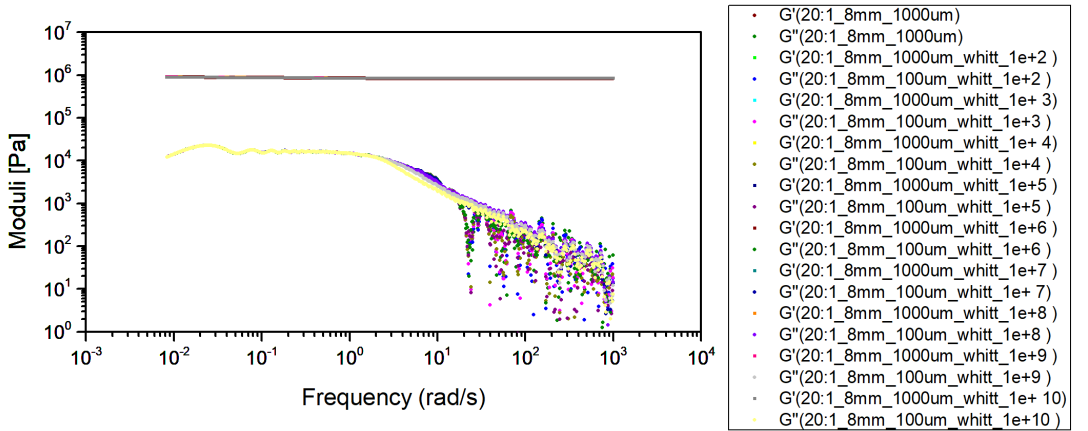


Figure 3.37: Plot of storage modulus G' and loss modulus G'' on the frequency domain of PDMS sample 20:1 using spherical indenter with 8mm in diameter and applying indentation depth of 1400 μm with smoothing parameters λ ranging from 10^2 to 10^{10}

When the Fourier transform is applied to these “phase-shifted” signals, the out-of-phase component is smaller than it should be, directly resulting in a severe and incorrect underestimation of the loss modulus, G'' . This is precisely the effect observed. The i-Rheo method’s strength is its ability to extract high-frequency data from the initial, raw transient phase of the measurement; an aggressive smoother destroys this very information.

In essence, while the Whittaker filter is theoretically viable for removing random measurement noise (Section 2.9), in this application it also removed physically meaningful high-frequency components that encode viscoelastic dissipation. This limitation was consistently observed across all PDMS formulations and indentation steps tested. The results suggest that, for Fourier-transform-based microrheology, any smoothing strategy must be carefully tuned to avoid compromising phase accuracy, with the risk of data distortion increasing dramatically at high λ values. This finding highlights that, although Whittaker–Henderson smoothing can be a powerful denoising tool, its indiscriminate application in dynamic mechanical analysis can lead to misleading rheological interpretations, especially for the loss modulus.

Chapter 4: Conclusions

A model-free, geometry-agnostic, single-experiment route to broadband linear viscoelastic (LVE) characterisation from step-indentation data was realised through the i-Rheo Squeeze application. The complex modulus $G^*(\omega) = G'(\omega) + iG''(\omega)$ was obtained as a transfer function, by forming the ratio of the analytical Fourier transforms of the measured force $F(t)$ and a geometry-aware deformation $\Lambda[\delta(t)]$ defined by contact mechanics; no Maxwell-mode fitting or idealised step assumptions were required (9; 35). A noise-aware analysis-window finder, phase-preserving interpolation/virtual oversampling, and support for multiple indenter geometries (spherical, cylindrical, conical, and four-sided pyramidal) were integrated in accordance with classical contact mechanics (17; 32; 36). The software was deployed behind NGINX to ensure secure, reproducible access.

Empirical validation on PDMS 5:1, 10:1, 20:1 demonstrated that consistent $G'(\omega)$ and $G''(\omega)$ are recovered across different tip geometries and sizes within clearly identified depth ranges, in agreement with the i-Rheo/AFM2 theoretical framework (35; 2). Log-spaced indentation depths on 2 mm slabs enabled identification of linear-regime/yield-plateau intervals in which G' is approximately constant, permitting geometry-invariant comparisons predicted by LVE theory. The expected stiffness ordering: $20 : 1 \ll 10 : 15 : 1$ - was broadly respected, with 20:1 consistently softest and $G' \approx E/3$ in line with literature values for PDMS (10; 18; 28). A persistent observation in the dataset was $10 : 1 > 5 : 1$ in some cases. This inversion is plausible under realistic test conditions and contact mechanics: adhesive forces at shallow contact, finite-thickness stiffening at larger contact radii, history-dependent softening (Mullins-type), or curing/storage variability can bias local stiffness estimates; the repetition of this trend across tip sizes argues for a systematic experimental factor rather than a numerical artefact (17; 27; 2).

On the dissipative response, $G''(\omega)$ showed the anticipated increase toward intermediate ω but also the well-known phase sensitivity at higher frequencies. Controlled trials with Whittaker-Henderson smoothing confirmed its usefulness as a candidate pre-transform denoiser (penalised curvature, zero-phase), while also demonstrating that large smoothing parameters attenuate early-time features and underestimate G'' by erasing subtle phase lags (6). Consistent with i-Rheo theory, conservative or no smoothing, combined with careful window selection and virtual oversampling, provided the most reliable dissipation estimates (9; 35).

Objectives Assessment

O1 – Generalise the analytical framework: Achieved. Geometry-aware deformation mappings $\Lambda(\delta)$ were implemented for multiple indenters, and experiments exercised spherical and cylindrical tips, establishing geometry-agnostic recovery of $G^*(\omega)$.

O2 – Develop a robust Python program: Achieved. The application ingests raw Excel data, auto-detects the relaxation window with manual overrides, exposes numerical controls (interpolation density, oversampling, plotting grid), computes $G'(\omega)$, $G''(\omega)$, $\tan \delta(\omega)$, and exports results; deployment via NGINX enables secure access.

O3 – Acquire validation data: Achieved. PDMS datasets across ratios and indenters verified broadband spectra and cross-geometry consistency in the identified plateau ranges;

the 10:1 vs 5:1 discrepancy was documented and critically interpreted within contact-mechanics/LVE theory rather than masked by fitting.

Chapter 5: Future Considerations

- The present study validated spherical and cylindrical tips only. To complete the geometry-agnostic remit, the deformation mapping $\Lambda(\delta)$ will be implemented and validated for Conical tips and Four-sided pyramids.
- The repeated observation that 10:1 appears stiffer than 5:1 in some conditions remains unresolved. Potential contributors include adhesion at shallow δ , finite-thickness stiffening at larger δ , load-history/Mullins softening, and curing/storage variability. A factorial protocol (ratio \times depth \times site renewal \times adhesion-reduction) together with independent E checks (e.g., tensile/DMA) is required to isolate the dominant factor
- Additional noise-reduction methods will be surveyed and prototyped to complement the current oversampling pipeline. Priority will be given to phase-preserving approaches so that early-time features—and thus G'' —are not attenuated. Candidates include symmetric FIR zero-phase filters, Savitzky–Golay smoothing on a uniform re-sample grid, constrained spline/P-spline smoothing, wavelet shrinkage, total-variation regularisation, and simple state-space (Kalman) filters. Each method will be benchmarked on synthetic and real PDMS traces with controlled noise injection, using common criteria: (i) improvement in SNR; (ii) phase distortion at short times; (iii) bias on $G'(\omega)$, $G''(\omega)$ and $\tan \delta(\omega)$; and (iv) runtime. The best performers will be added to the app as optional, tunable pre-processing steps with sensible defaults and an automatic quality check (e.g., residual whiteness and high-frequency coherence) to guide users away from settings that would distort dissipation.

Bibliography

- [1] M. Baumgärtel and H. H. Winter. Determination of discrete relaxation and retardation time spectra from dynamic mechanical data. *Rheologica Acta*, 28:511–519, 1989.
- [2] Y. H. Chim, L. M. Mason, N. Rath, M. F. Olson, M. Tassieri, and H. Yin. A one-step procedure to probe the viscoelastic properties of cells by atomic force microscopy. *Scientific Reports*, 8(1):14462, 2018.
- [3] J. C. Crocker, M. T. Valentine, E. R. Weeks, T. Gisler, P. D. Kaplan, A. G. Yodh, and D. A. Weitz. Two-point microrheology of inhomogeneous soft materials. *Physical Review Letters*, 85(4):888–891, 2000.
- [4] J. Diani, B. Fayolle, and P. Gilormini. A review on the mullins effect. *European Polymer Journal*, 45(3):601–612, 2009.
- [5] E. K. Dimitriadis, F. Horkay, J. Maresca, B. Kachar, and R. S. Chadwick. Determination of elastic moduli of thin layers of soft material using AFM. *Biophysical Journal*, 82(5):2798–2810, 2002.
- [6] P. H. C. Eilers. A perfect smoother. *Analytical Chemistry*, 75(14):3631–3636, 2003.
- [7] P. H. C. Eilers and H. F. M. Boelens. Baseline correction with asymmetric least squares smoothing. Technical report, Leiden University, 2005. Technical Note.
- [8] P. H. C. Eilers and B. D. Marx. Flexible smoothing with B-splines and penalties (P-splines). *Statistical Science*, 11(2):89–121, 1996.
- [9] R. M. L. Evans, M. Tassieri, D. Auhl, and T. A. Waigh. Direct conversion of rheological compliance measurements into storage and loss moduli. *Physical Review E*, 80(1):012501, 2009.
- [10] J. D. Ferry. *Viscoelastic Properties of Polymers*. John Wiley & Sons, 3rd edition, 1980.
- [11] F. Gittes, B. Schnurr, P. D. Olmsted, F. C. MacKintosh, and C. F. Schmidt. Microscopic viscoelasticity: Shear moduli of soft materials determined from thermal fluctuations. *Physical Review Letters*, 79(17):3286–3289, 1997.
- [12] C. R. Harris, K. J. Millman, S. J. van der Walt, R. Gommers, P. Virtanen, D. Cournapeau, E. Wieser, J. Taylor, S. Berg, N. J. Smith, et al. Array programming with NumPy. *Nature*, 585(7825):357–362, 2020.
- [13] R. Henderson. A new method for graduation. *Transactions of the Faculty of Actuaries*, 8:34–62, 1924.
- [14] H. Hertz. Ueber die Berührung fester elastischer Körper (On the contact of elastic solids). *Journal für die reine und angewandte Mathematik*, 92:156–171, 1882.
- [15] J. Honerkamp and J. Weese. A nonlinear regularization method for the calculation of relaxation spectra. *Rheologica Acta*, 32:65–73, 1993.
- [16] J. D. Hunter. Matplotlib: A 2D graphics environment. *Computing in Science & Engineering*, 9(3):90–95, 2007.

- [17] K. L. Johnson. *Contact Mechanics*. Cambridge University Press, 1985.
- [18] I. D. Johnston, D. K. McCluskey, C. K. L. Tan, and M. C. Tracey. Mechanical characterization of bulk Sylgard 184 for microfluidics and microengineering. *Journal of Micromechanics and Microengineering*, 24(3):035017, 2014.
- [19] K. Kendall, M. Kendall, and F. Rehfeldt. Crack propagation in brittle elastomers. *Journal of Materials Science*, 22(12):4301–4308, 1987.
- [20] L. D. Landau, A. M. Kosevich, L. P. Pitaevskii, and E. M. Lifshitz. *Theory of Elasticity*. Butterworth-Heinemann, Oxford, 3rd edition, 1986.
- [21] E. H. Lee and J. R. M. Radok. The contact problem for viscoelastic bodies. *Journal of Applied Mechanics*, 27:438–444, 1960.
- [22] J. N. Lee, C. Park, and G. M. Whitesides. Solvent compatibility of poly(dimethylsiloxane)-based microfluidic devices. *Analytical Chemistry*, 75(23):6544–6554, 2003. Accessed in 2017.
- [23] A. E. Likhtman and T. C. B. McLeish. Quantitative theory for linear dynamics of linear entangled polymers. *Macromolecules*, 35:6332–6343, 2002.
- [24] C. W. Macosko. *Rheology: Principles, Measurements, and Applications*. VCH Publishers, 1994.
- [25] T. G. Mason and D. A. Weitz. Optical measurements of frequency-dependent linear viscoelastic moduli of complex fluids. *Physical Review Letters*, 74(7):1250–1253, 1995.
- [26] W. C. Oliver and G. M. Pharr. An improved technique for determining hardness and elastic modulus using load and displacement sensing indentation experiments. *Journal of Materials Research*, 7(6):1564–1583, 1992.
- [27] W. C. Oliver and G. M. Pharr. Measurement of hardness and elastic modulus by instrumented indentation: Advances in understanding and refinements to methodology. *Journal of Materials Research*, 19(1):3–20, 2004.
- [28] R. N. Palchesko, L. Zhang, Y. Sun, and A. W. Feinberg. Development of polydimethylsiloxane substrates with tunable elastic modulus to study cell mechanobiology. *PLoS ONE*, 7(12):e51499, 2012.
- [29] J. Park, S. J. Yoo, J. Lee, and J. Kim. Effect of curing conditions on the mechanical properties of polydimethylsiloxane. *Journal of Micromechanics and Microengineering*, 20(5):055004, 2010.
- [30] Valentin L. Popov, Markus Heß, and Emanuel Willert. *Handbook of Contact Mechanics*. Springer, 2019.
- [31] M. Rubinstein and R. H. Colby. *Polymer Physics*. Oxford University Press, 2003.
- [32] I. N. Sneddon. The relation between load and penetration in the axisymmetric boussinesq problem for a punch of arbitrary profile. *International Journal of Engineering Science*, 3(1):47–57, 1965.
- [33] C. Storm, J. J. Pastore, F. C. MacKintosh, T. C. Lubensky, and P. A. Janmey. Nonlinear elasticity in biological gels. *Nature*, 435(7039):191–194, 2005.

- [34] M. Tassieri, R. M. L. Evans, R. L. Warren, N. J. Bailey, and J. M. Cooper. Microrheology with optical tweezers: data analysis. *New Journal of Physics*, 14(11):115032, 2012.
- [35] M. Tassieri, M. Laurati, D. J. Curtis, D. W. Auhl, S. Coppola, A. Scalfati, K. Hawkins, P. R. Williams, and J. M. Cooper. i-Rheo: Measuring the materials' linear viscoelastic properties "in a step"! *Journal of Rheology*, 60(4):649–660, 2016.
- [36] T. C. T. Ting. The contact stresses between a rigid indenter and a viscoelastic half-space. *Journal of Applied Mechanics*, 33(4):845–854, 1966.
- [37] L. R. G. Treloar. *The Physics of Rubber Elasticity*. Oxford University Press, 3rd edition, 1975.
- [38] S. Tripathy and E. J. Berger. Measuring viscoelasticity of soft samples using atomic force microscopy. *Journal of Biomechanical Engineering*, 131(6), 2009.
- [39] N. W. Tschoegl. *The Phenomenological Theory of Linear Viscoelastic Behavior*. Springer, 1989.
- [40] P. Virtanen, R. Gommers, T. E. Oliphant, M. Haberland, T. Reddy, D. Cournapeau, E. Burovski, P. Peterson, W. Weckesser, J. Bright, et al. SciPy 1.0: fundamental algorithms for scientific computing in Python. *Nature Methods*, 17(3):261–272, 2020.
- [41] Z. Wang, A. A. Volinsky, and N. D. Gallant. Crosslinking effect on polydimethylsiloxane elastic modulus measured by custom-built compression instrument. *Journal of Applied Polymer Science*, 131(22), 2014.
- [42] E. T. Whittaker. On a new method of graduation. *Proceedings of the Edinburgh Mathematical Society*, 41:63–75, 1923.

Appendix A: First appendix

A.1 Implementation repository

The active website application is available [here](#)

The source code for the program is available [here](#)

The Dataset gathered is available [here](#)

Appendix B: Second appendix

B.1 Data collection

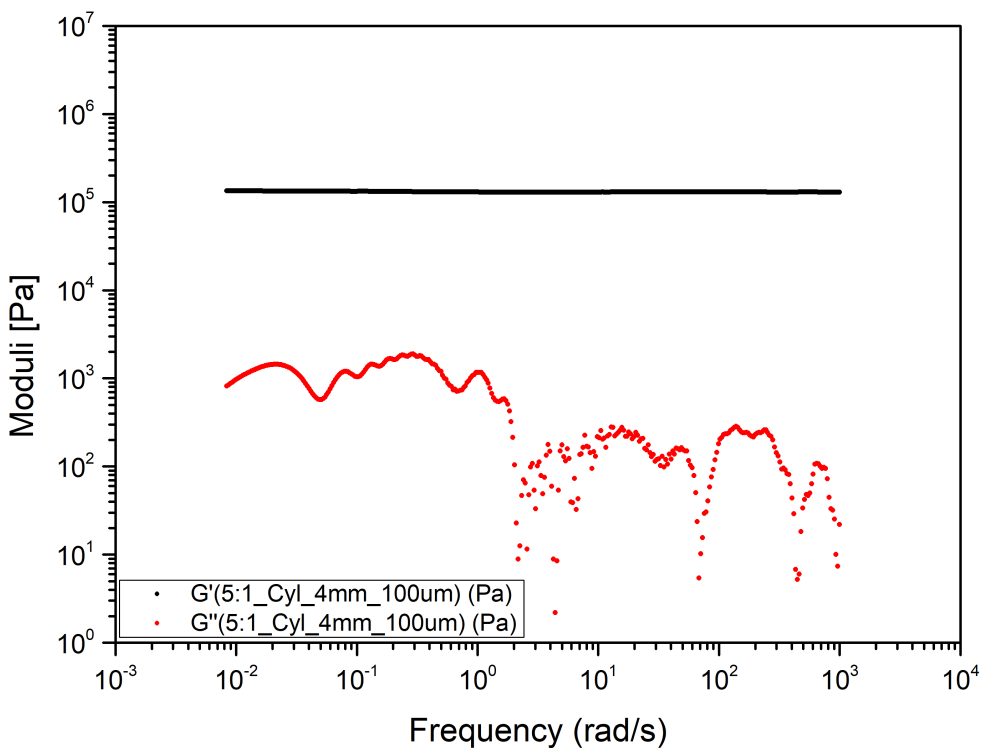


Figure B.1: the 5:1 PDMS sample's viscoelastic moduli derived by means of i-Rheo indentation using cylindrical indenter with 4mm in diameter and applying 0.1mm depth

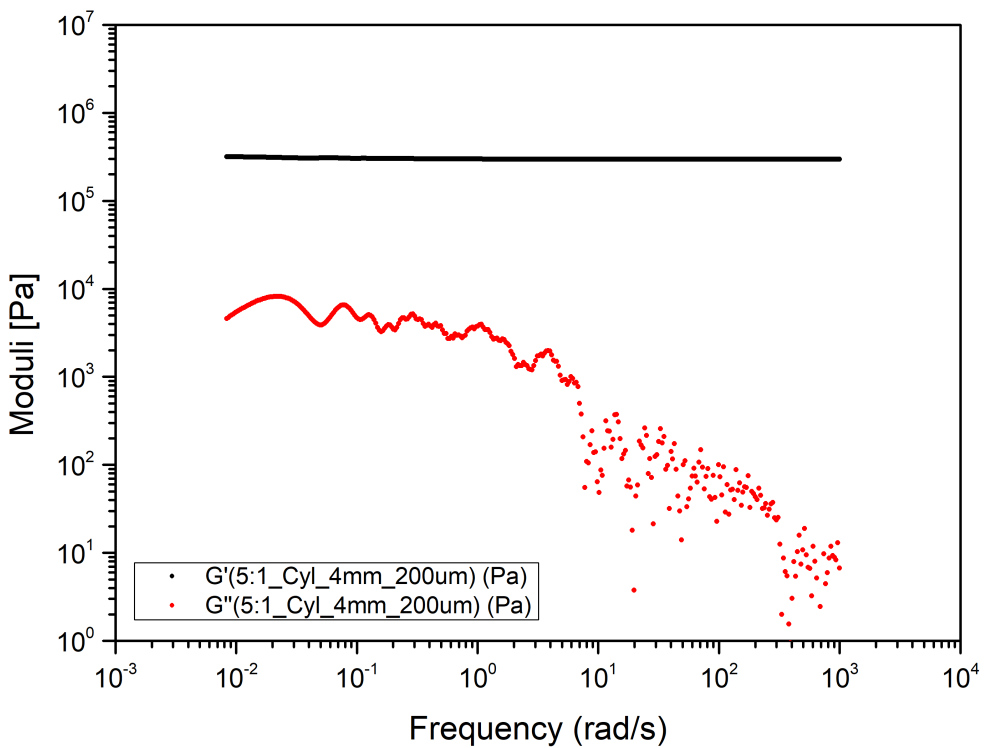


Figure B.2: the 5:1 PDMS sample's viscoelastic moduli derived by means of i-Rheo indentation using cylindrical indenter with 4mm in diameter and applying 0.2mm depth

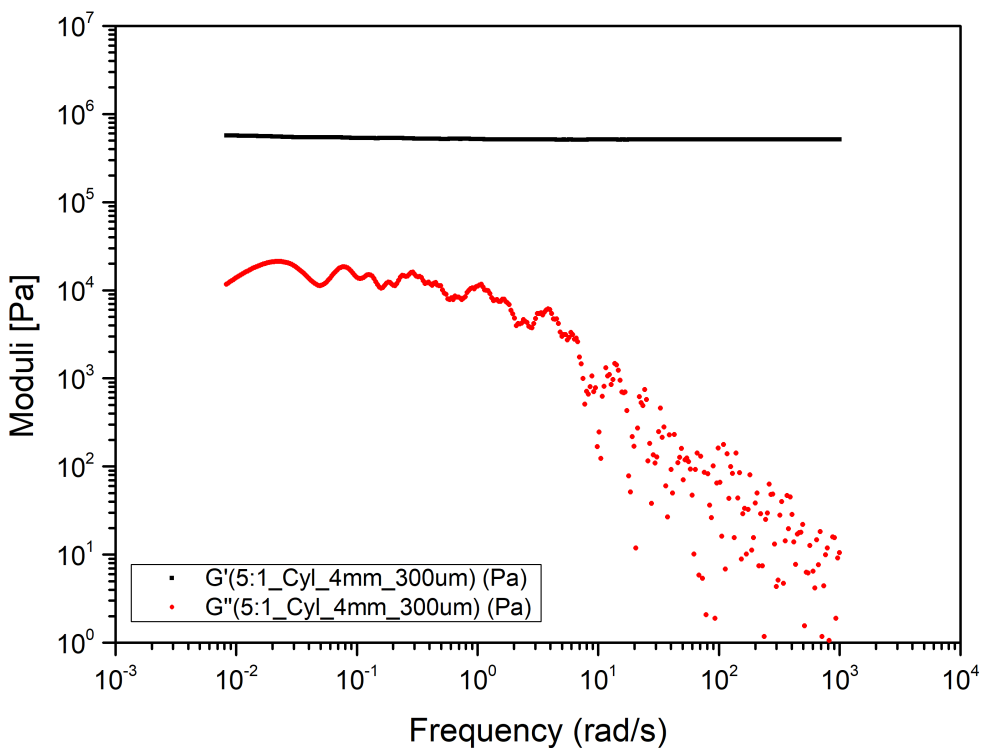


Figure B.3: the 5:1 PDMS sample's viscoelastic moduli derived by means of i-Rheo indentation using cylindrical indenter with 4mm in diameter and applying 0.3mm depth

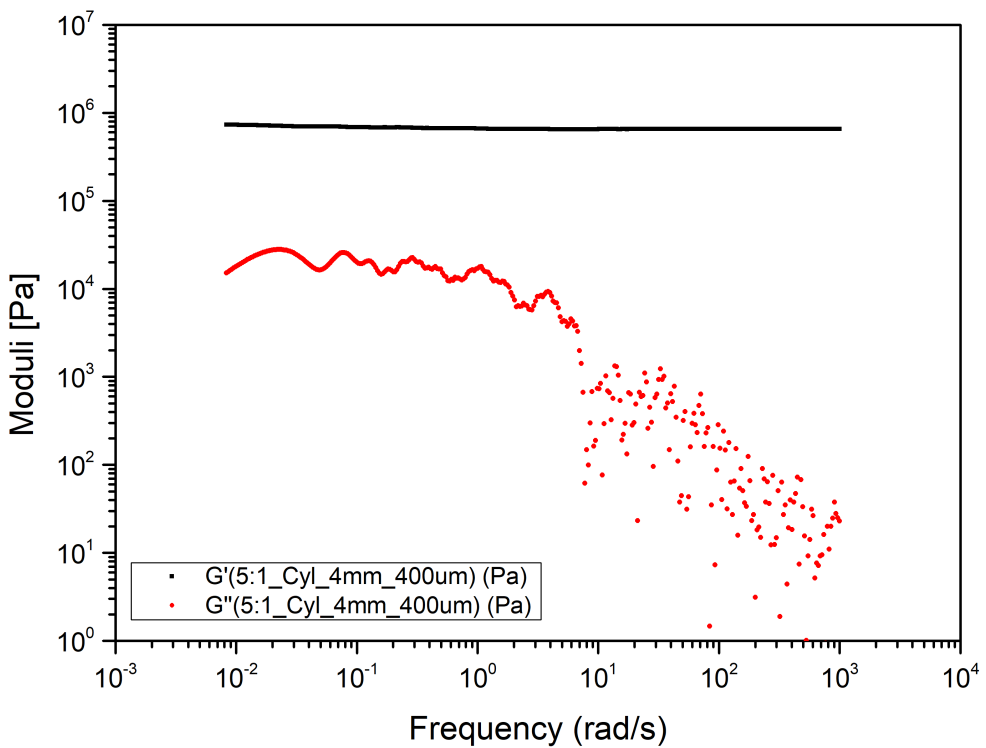


Figure B.4: the 5:1 PDMS sample's viscoelastic moduli derived by means of i-Rheo indentation using cylindrical indenter with 4mm in diameter and applying 0.4mm depth

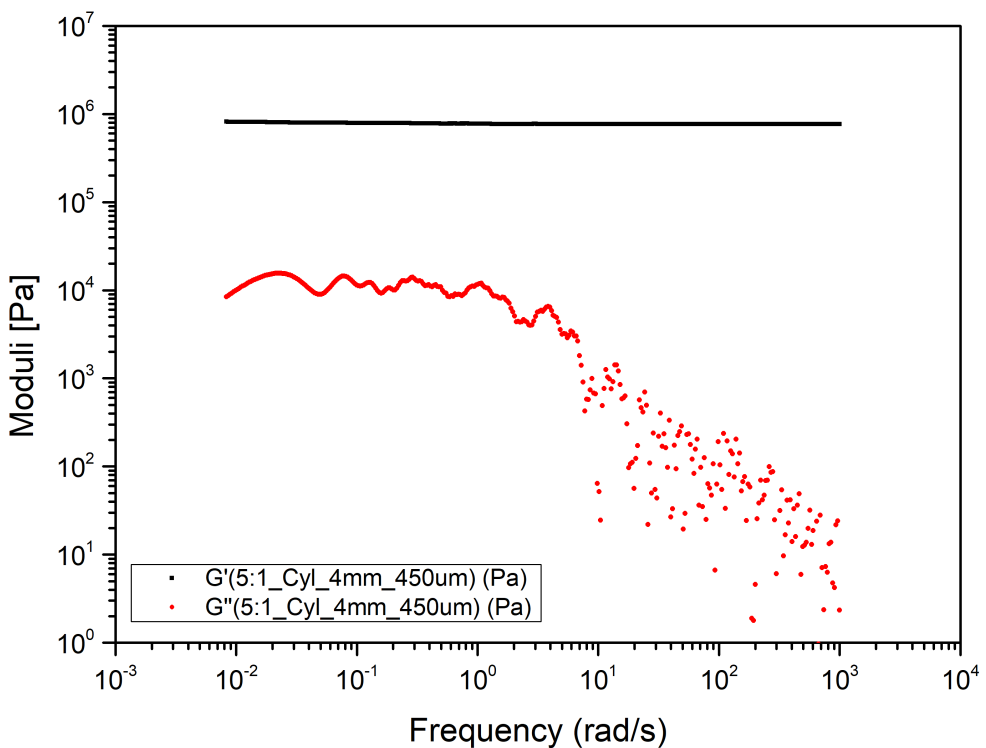


Figure B.5: the 5:1 PDMS sample's viscoelastic moduli derived by means of i-Rheo indentation using cylindrical indenter with 4mm in diameter and applying 0.45mm depth

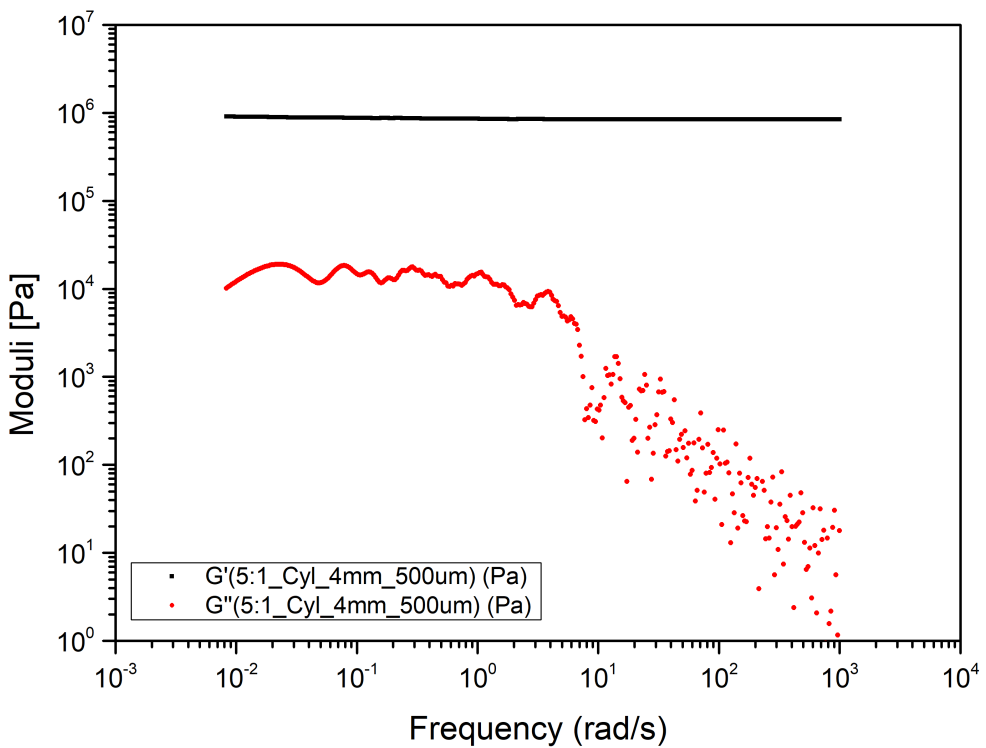


Figure B.6: the 5:1 PDMS sample's viscoelastic moduli derived by means of i-Rheo indentation using cylindrical indenter with 4mm in diameter and applying 0.5mm depth

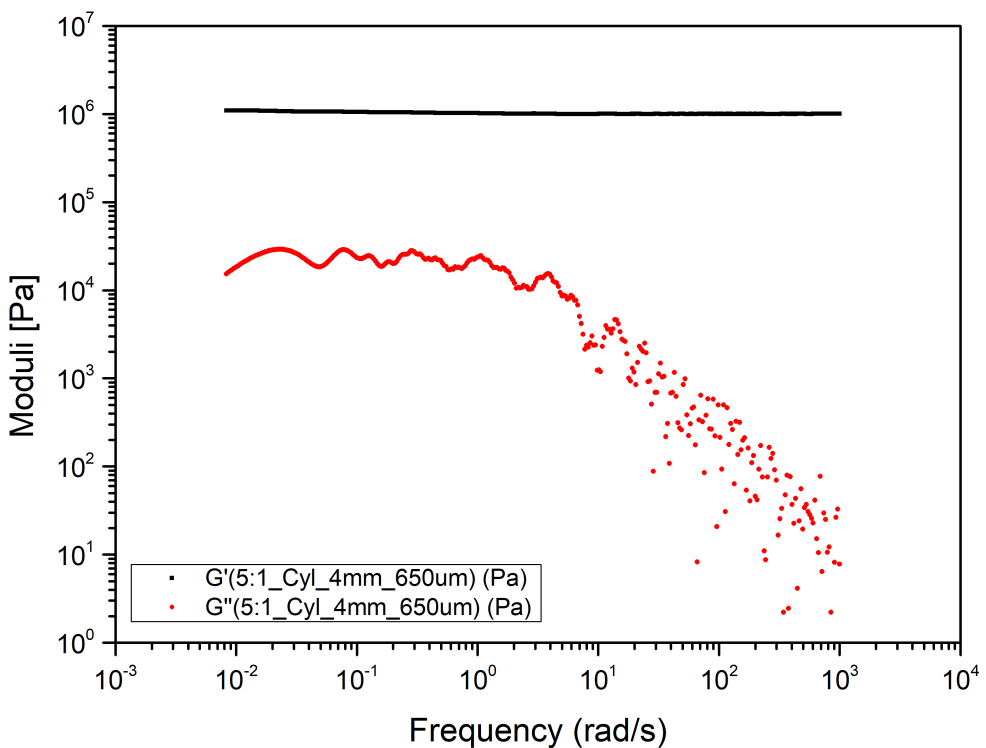


Figure B.7: the 5:1 PDMS sample's viscoelastic moduli derived by means of i-Rheo indentation using cylindrical indenter with 4mm in diameter and applying 0.65mm depth

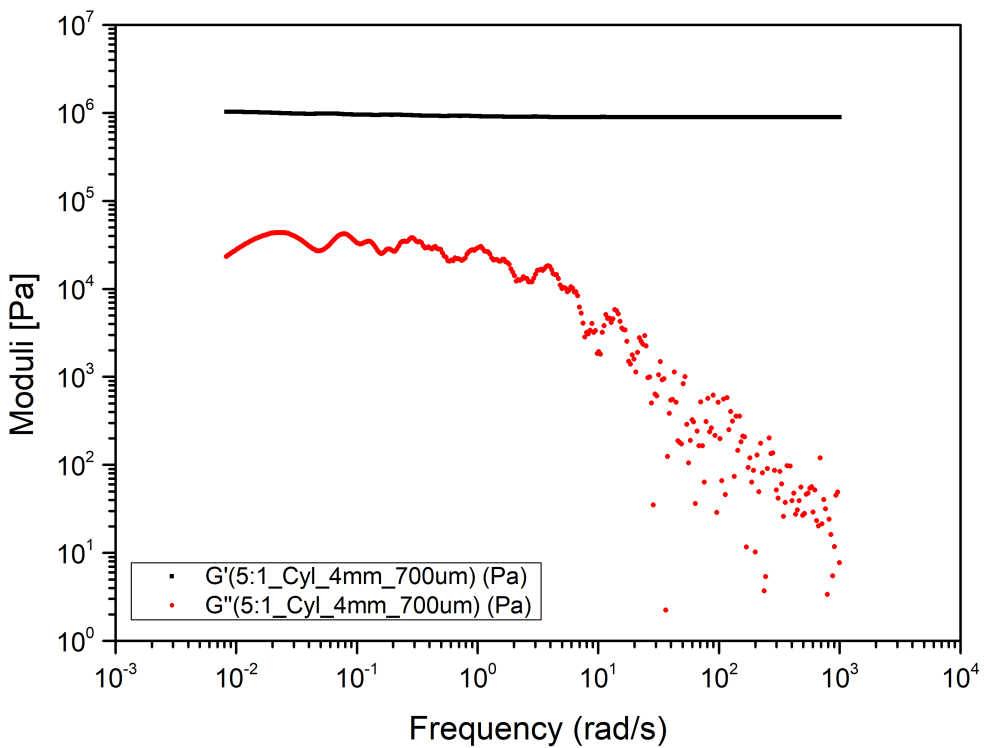


Figure B.8: the 5:1 PDMS sample's viscoelastic moduli derived by means of i-Rheo indentation using cylindrical indenter with 4mm in diameter and applying 0.7mm depth

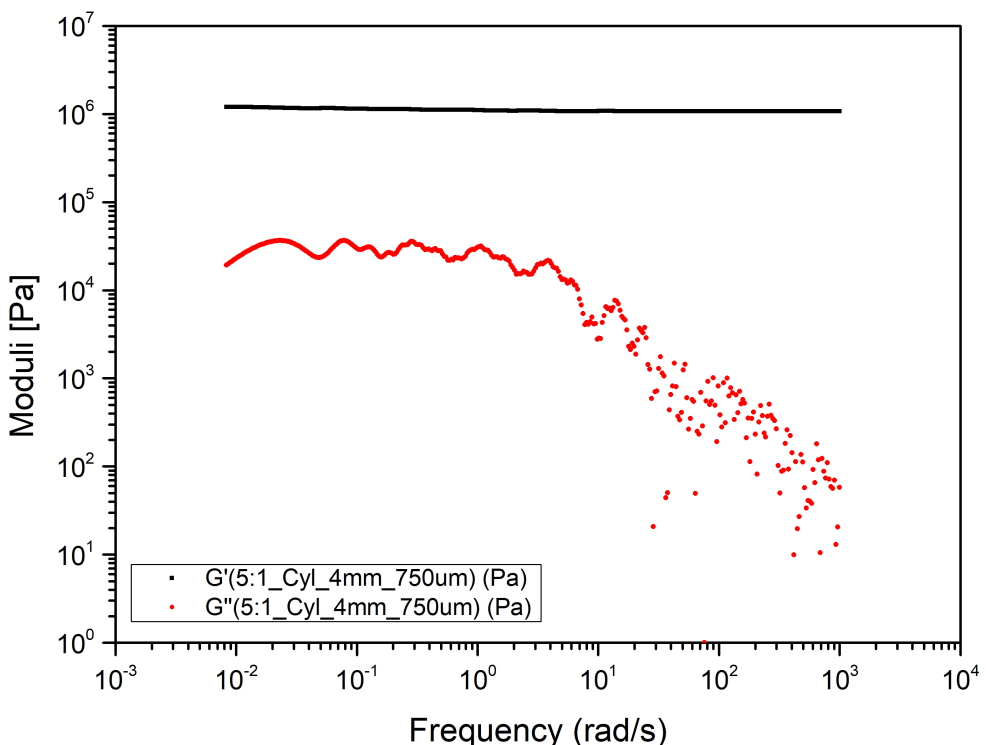


Figure B.9: the 5:1 PDMS sample's viscoelastic moduli derived by means of i-Rheo indentation using cylindrical indenter with 4mm in diameter and applying 0.75mm depth

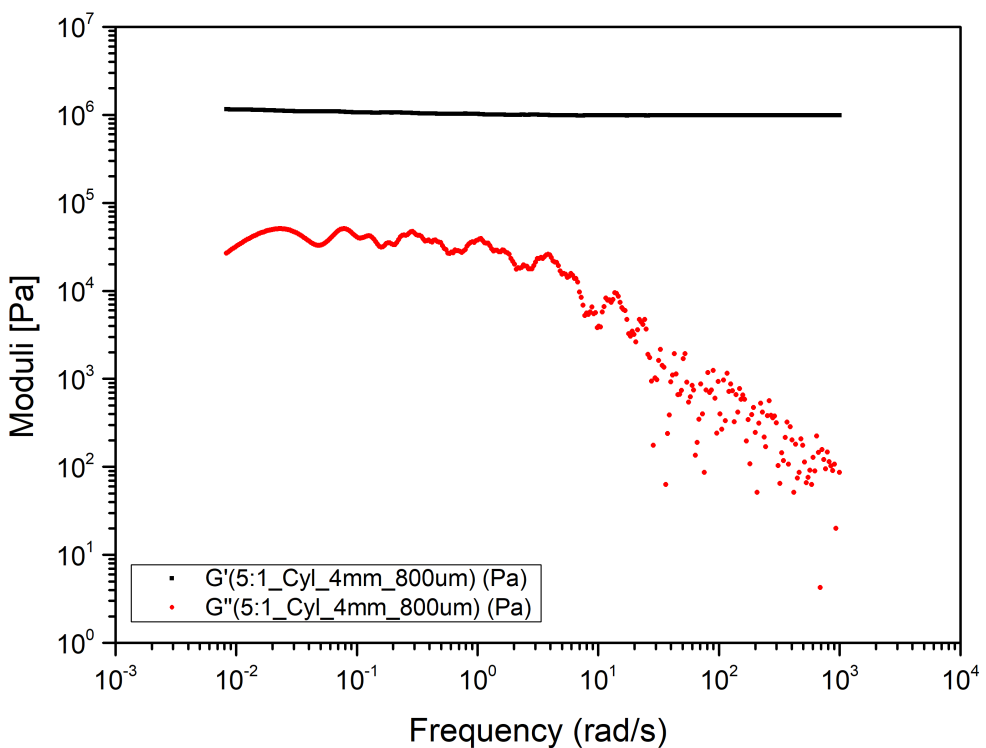


Figure B.10: the 5:1 PDMS sample's viscoelastic moduli derived by means of i-Rheo indentation using cylindrical indenter with 4mm in diameter and applying 0.8mm depth

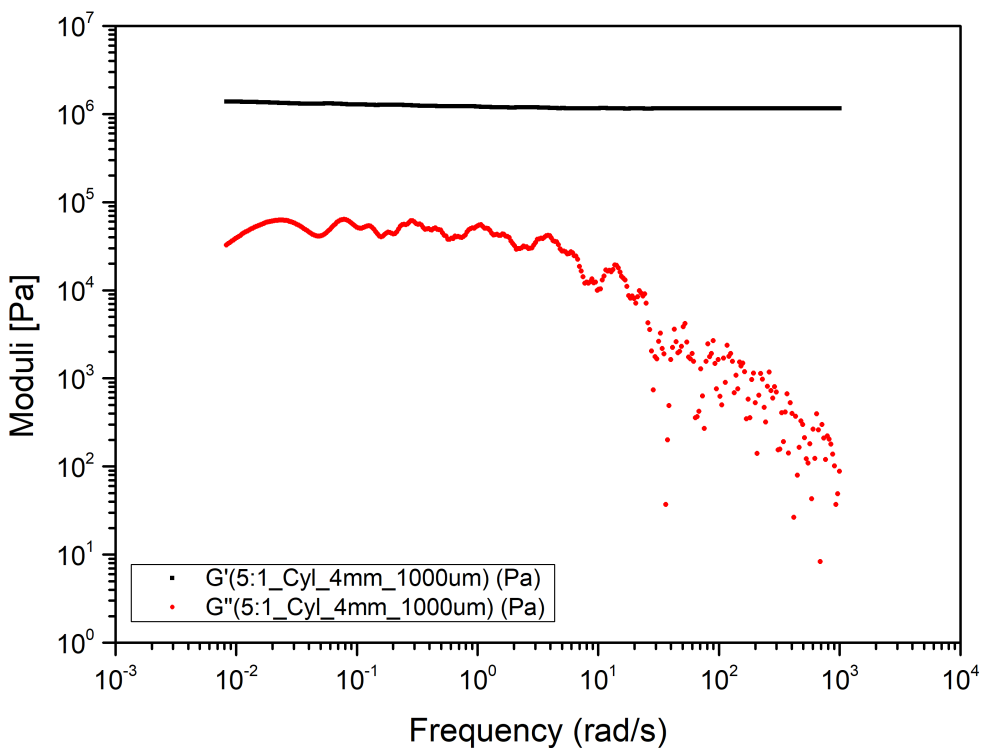


Figure B.11: the 5:1 PDMS sample's viscoelastic moduli derived by means of i-Rheo indentation using cylindrical indenter with 4mm in diameter and applying 1mm depth

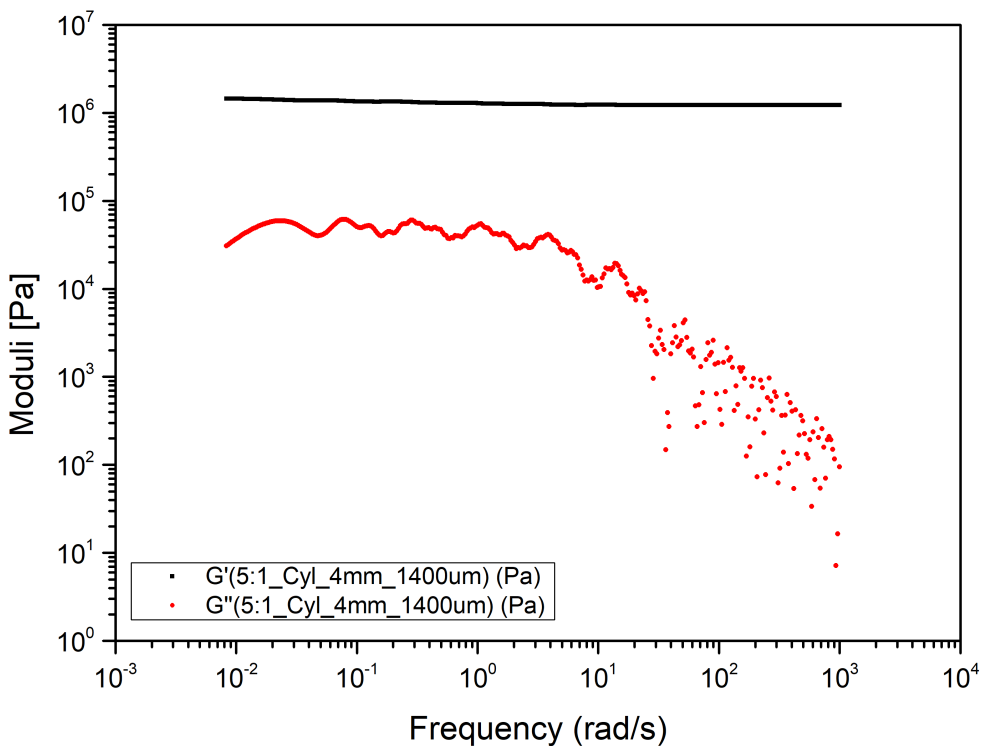


Figure B.12: the 5:1 PDMS sample's viscoelastic moduli derived by means of i-Rheo indentation using cylindrical indenter with 4mm in diameter and applying 1.4mm depth

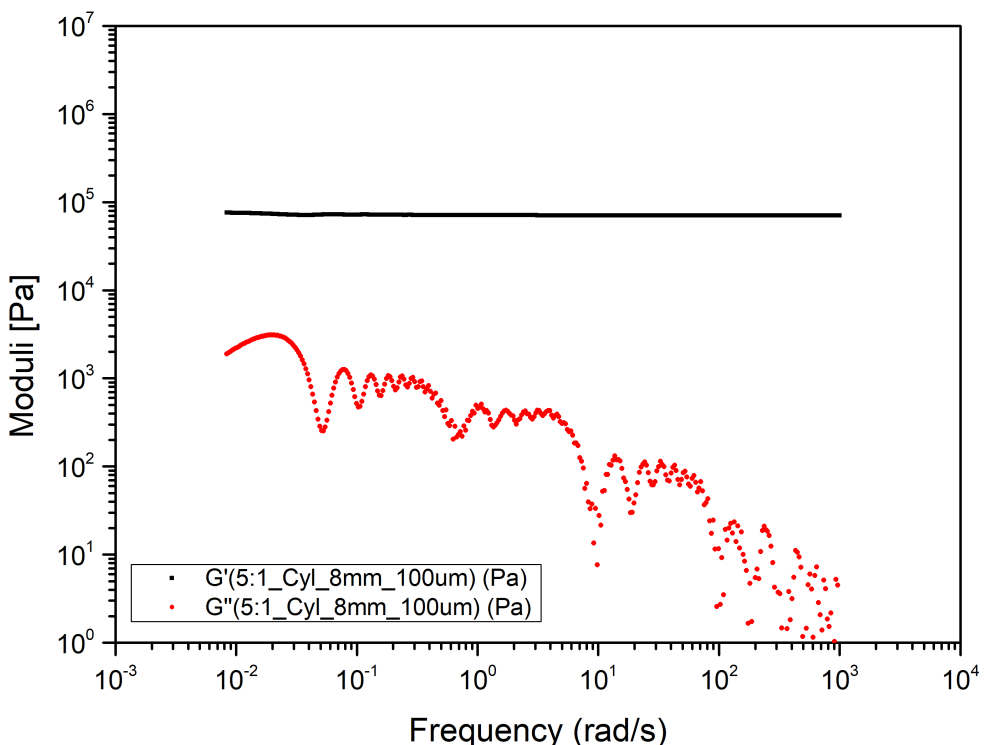


Figure B.13: the 5:1 PDMS sample's viscoelastic moduli derived by means of i-Rheo indentation using cylindrical indenter with 8mm in diameter and applying 0.1mm depth

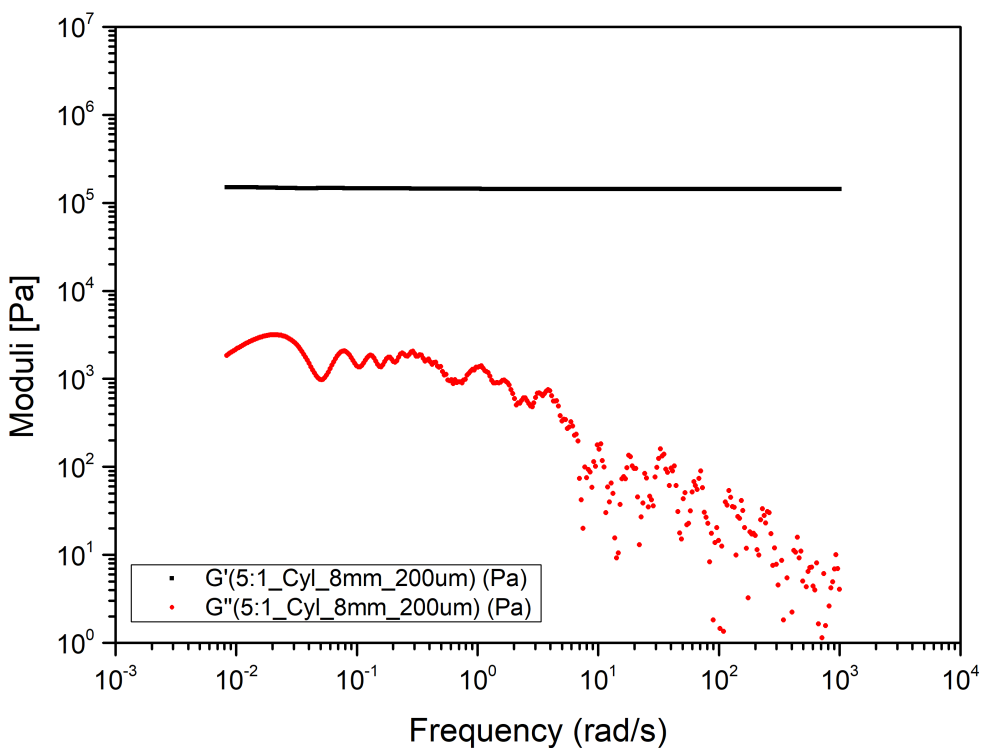


Figure B.14: the 5:1 PDMS sample's viscoelastic moduli derived by means of i-Rheo indentation using cylindrical indenter with 8mm in diameter and applying 0.2mm depth

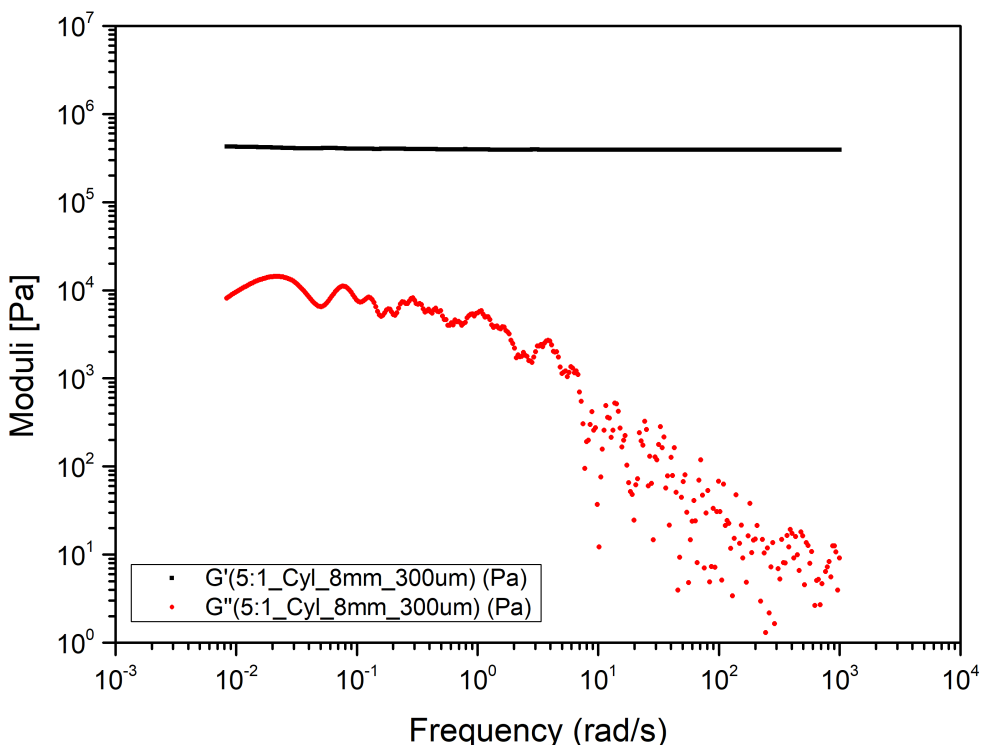


Figure B.15: the 5:1 PDMS sample's viscoelastic moduli derived by means of i-Rheo indentation using cylindrical indenter with 8mm in diameter and applying 0.3mm depth

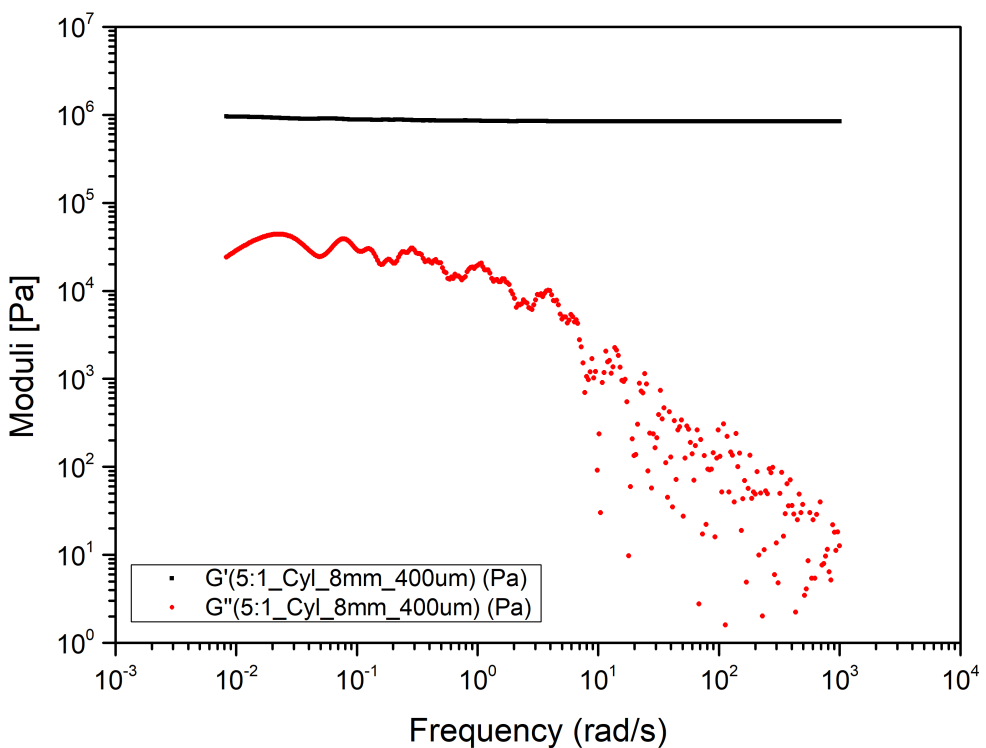


Figure B.16: the 5:1 PDMS sample's viscoelastic moduli derived by means of i-Rheo indentation using cylindrical indenter with 8mm in diameter and applying 0.4mm depth

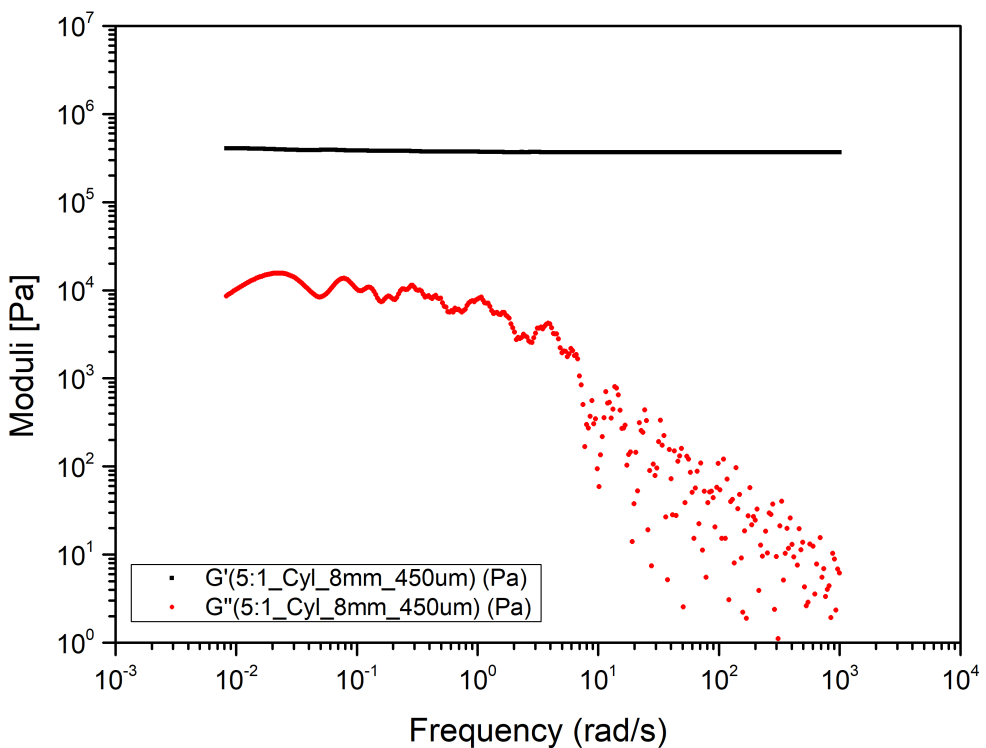


Figure B.17: the 5:1 PDMS sample's viscoelastic moduli derived by means of i-Rheo indentation using cylindrical indenter with 8mm in diameter and applying 0.45mm depth

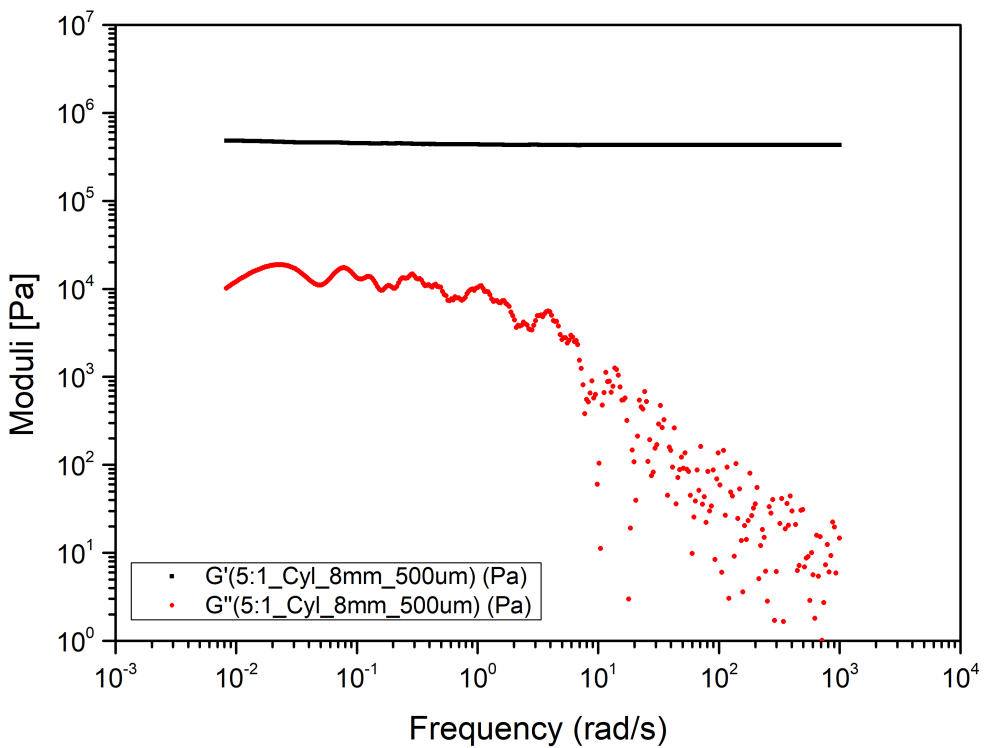


Figure B.18: the 5:1 PDMS sample's viscoelastic moduli derived by means of i-Rheo indentation using cylindrical indenter with 8mm in diameter and applying 0.5mm depth

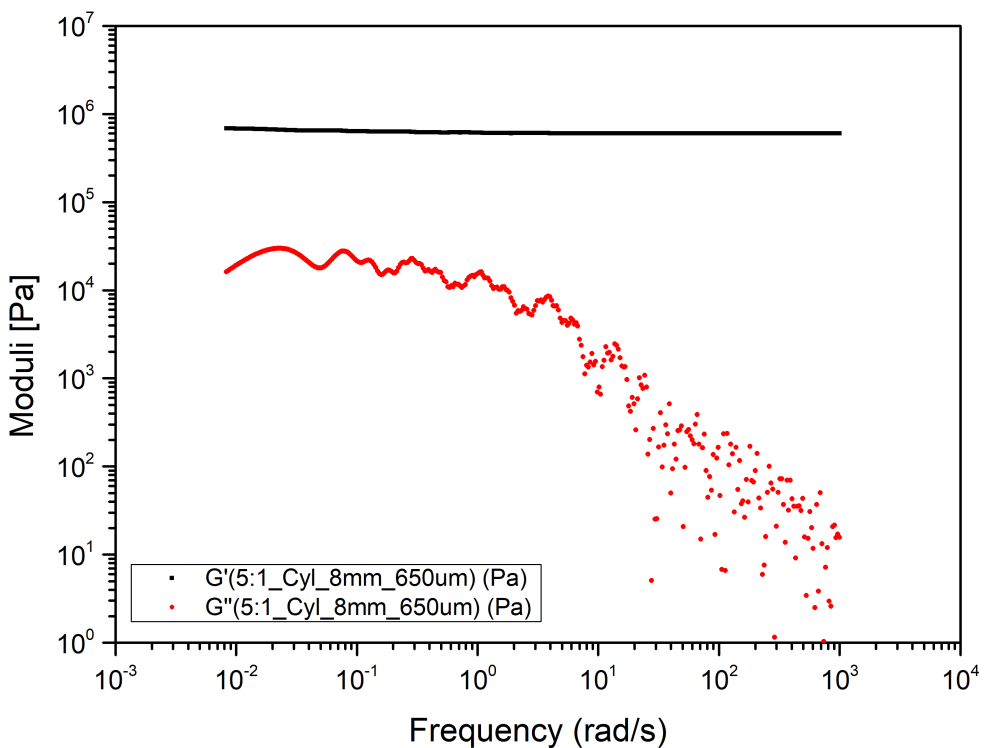


Figure B.19: the 5:1 PDMS sample's viscoelastic moduli derived by means of i-Rheo indentation using cylindrical indenter with 8mm in diameter and applying 0.65mm depth

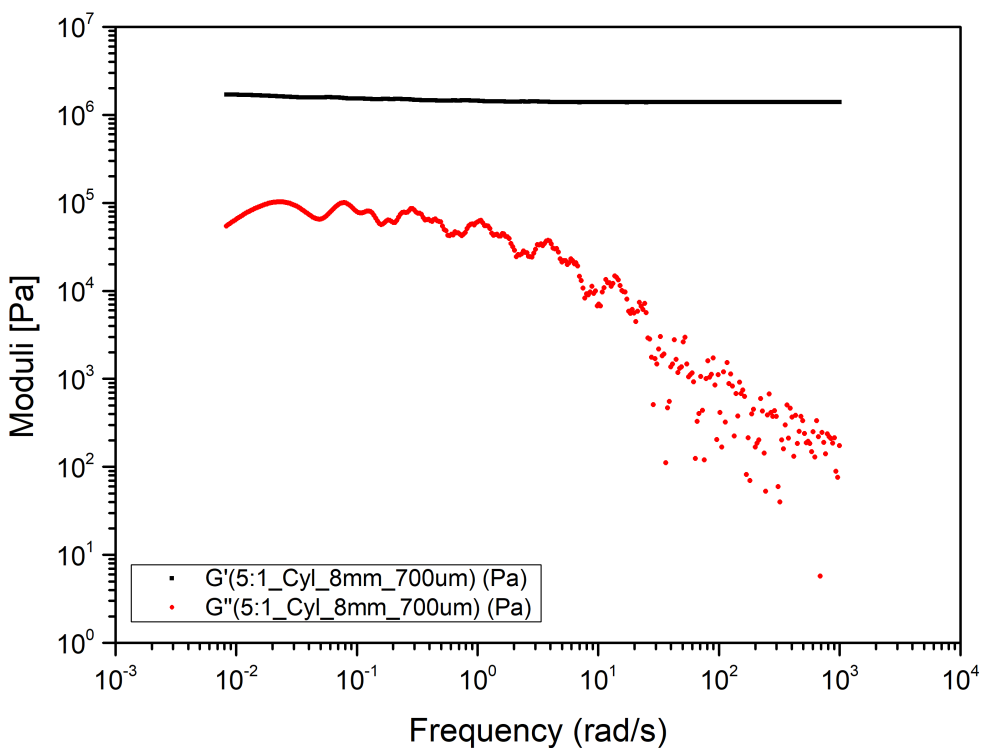


Figure B.20: the 5:1 PDMS sample's viscoelastic moduli derived by means of i-Rheo indentation using cylindrical indenter with 8mm in diameter and applying 0.7mm depth

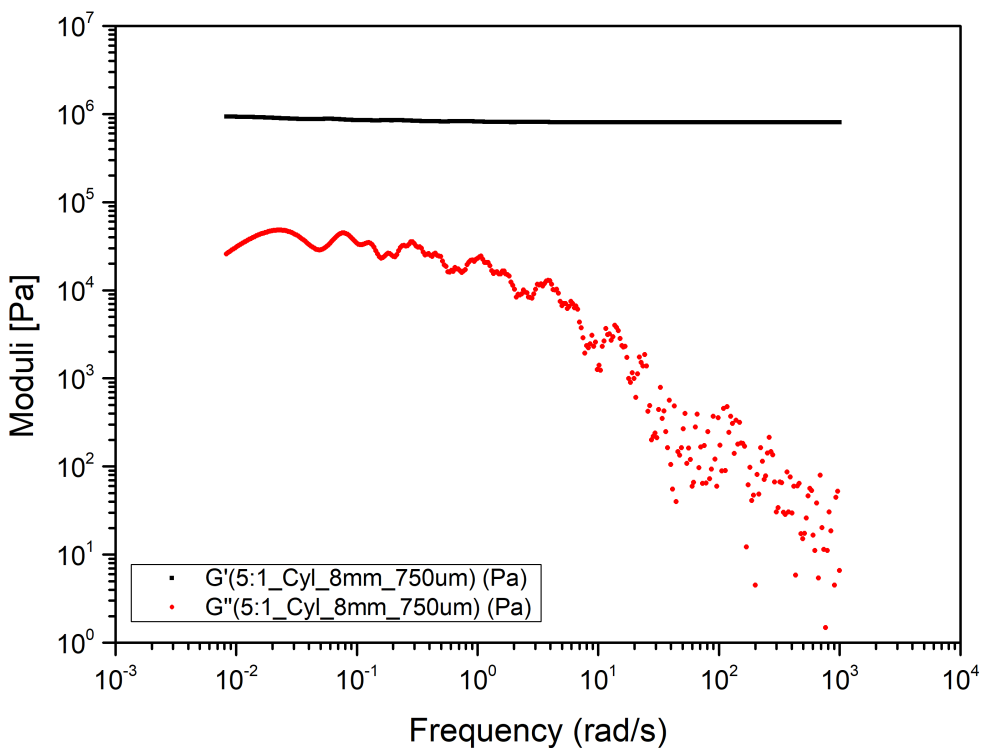


Figure B.21: the 5:1 PDMS sample's viscoelastic moduli derived by means of i-Rheo indentation using cylindrical indenter with 8mm in diameter and applying 0.75mm depth

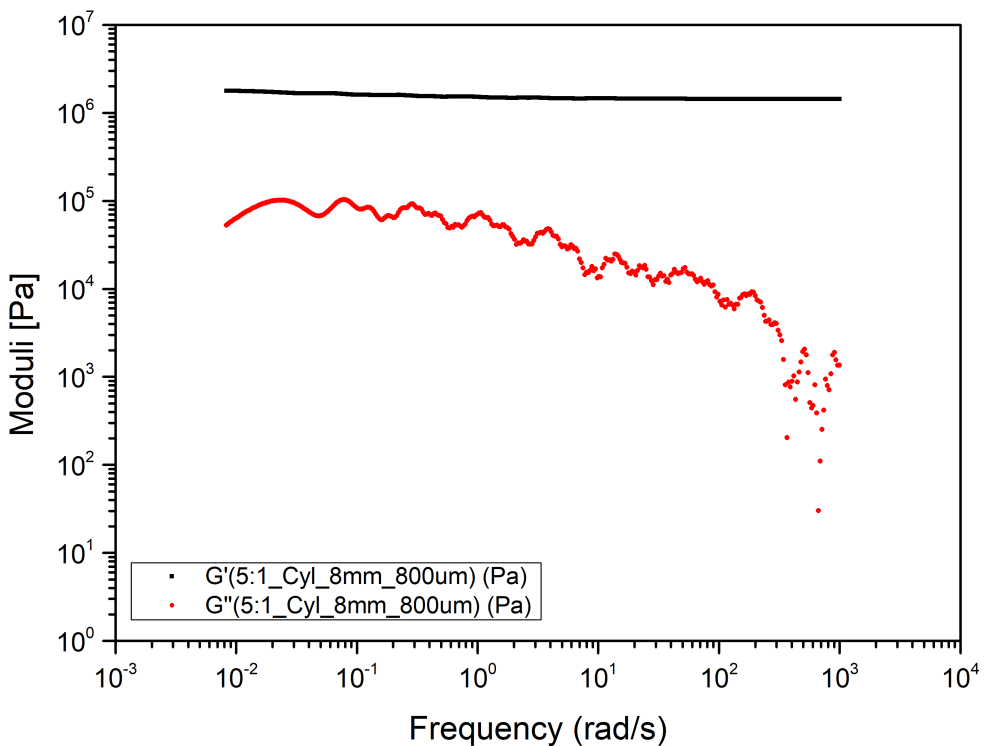


Figure B.22: the 5:1 PDMS sample's viscoelastic moduli derived by means of i-Rheo indentation using cylindrical indenter with 8mm in diameter and applying 0.8mm depth

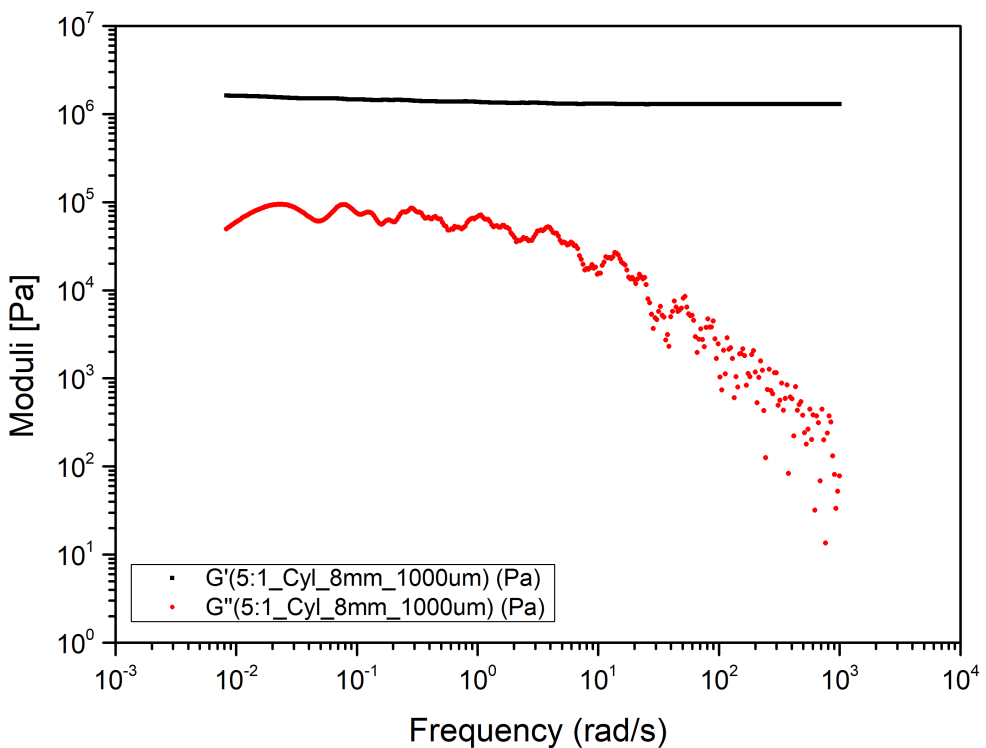


Figure B.23: the 5:1 PDMS sample's viscoelastic moduli derived by means of i-Rheo indentation using cylindrical indenter with 8mm in diameter and applying 1mm depth

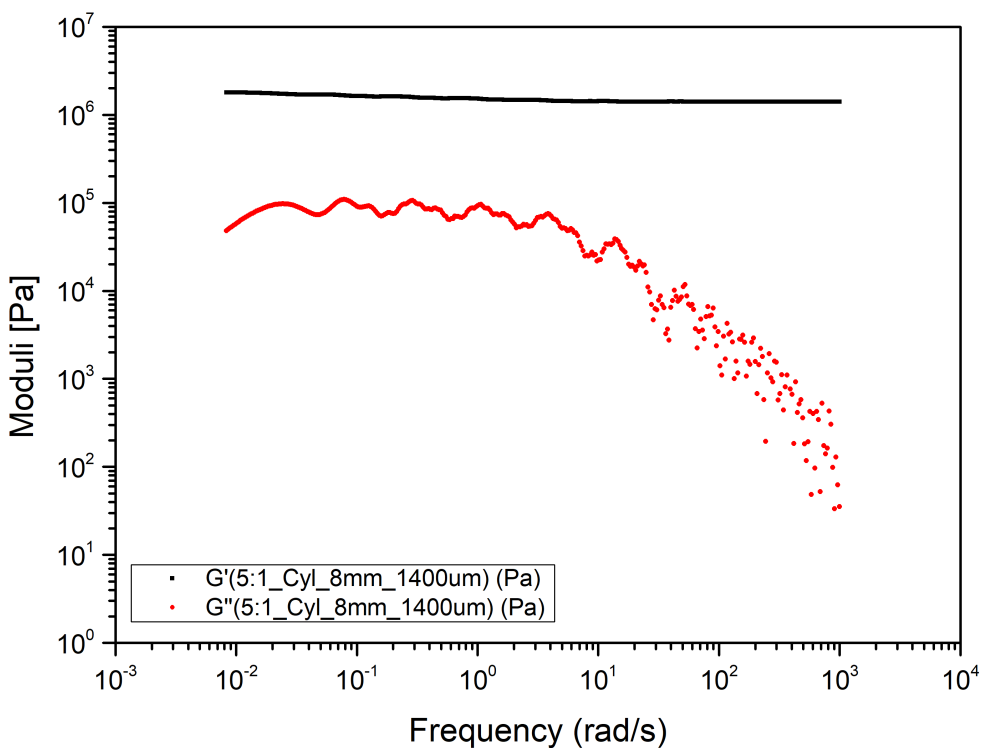


Figure B.24: the 5:1 PDMS sample's viscoelastic moduli derived by means of i-Rheo indentation using cylindrical indenter with 8mm in diameter and applying 1.4mm depth

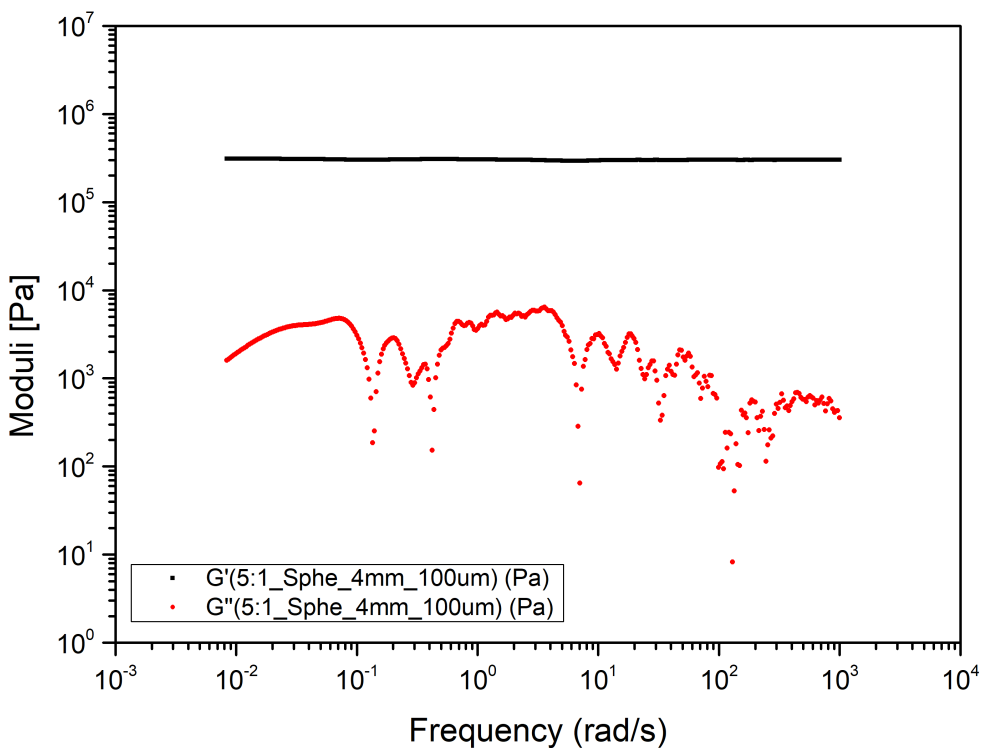


Figure B.25: the 5:1 PDMS sample's viscoelastic moduli derived by means of i-Rheo indentation using spherical indenter with 4mm in diameter and applying 0.1mm depth

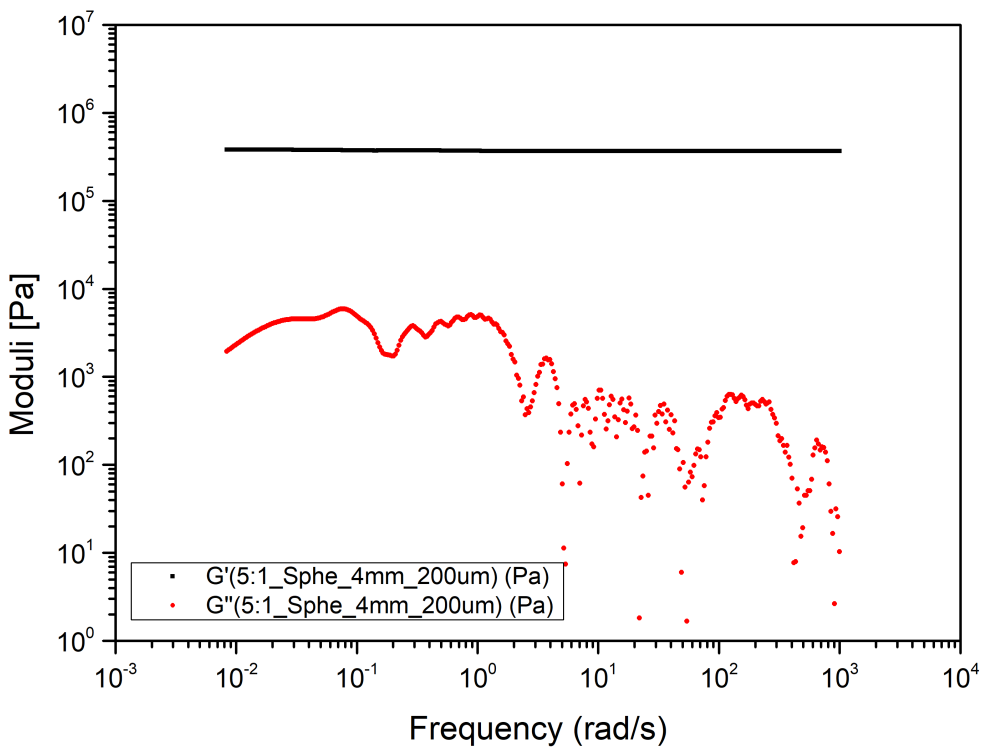


Figure B.26: the 5:1 PDMS sample's viscoelastic moduli derived by means of i-Rheo indentation using spherical indenter with 4mm in diameter and applying 0.2mm depth

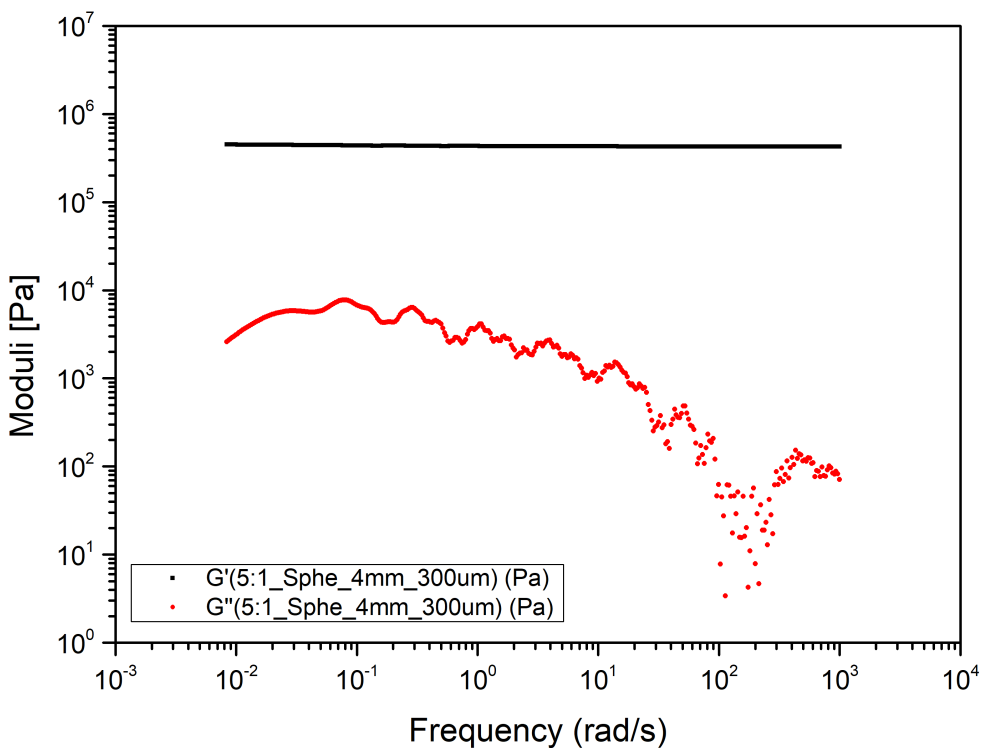


Figure B.27: the 5:1 PDMS sample's viscoelastic moduli derived by means of i-Rheo indentation using spherical indenter with 4mm in diameter and applying 0.3mm depth

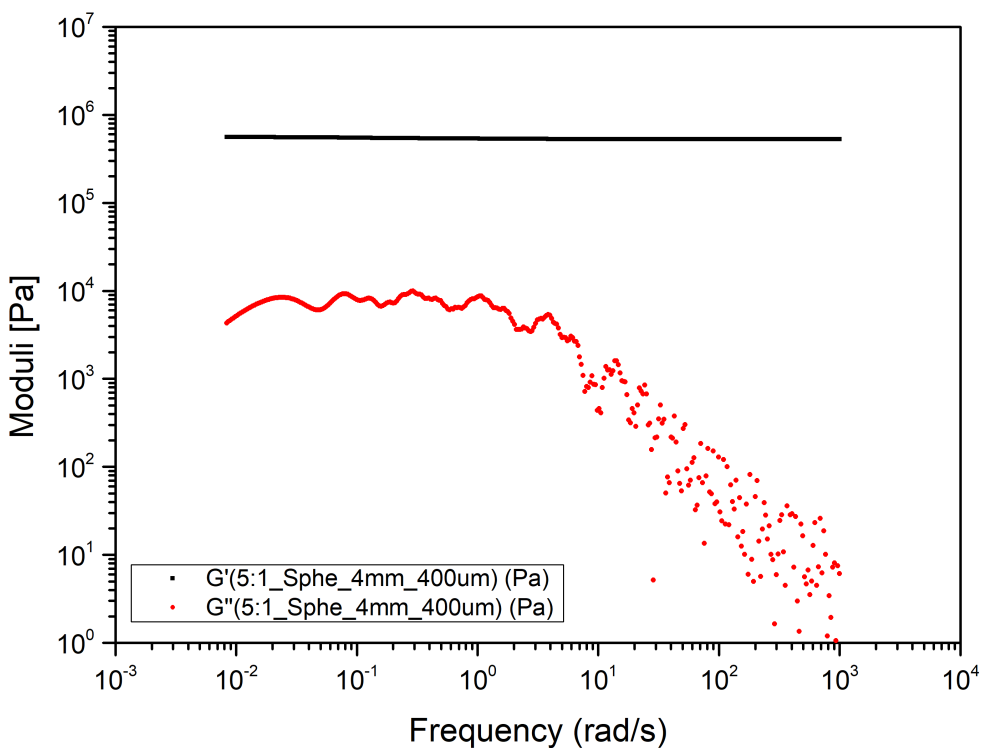


Figure B.28: the 5:1 PDMS sample's viscoelastic moduli derived by means of i-Rheo indentation using spherical indenter with 4mm in diameter and applying 0.4mm depth

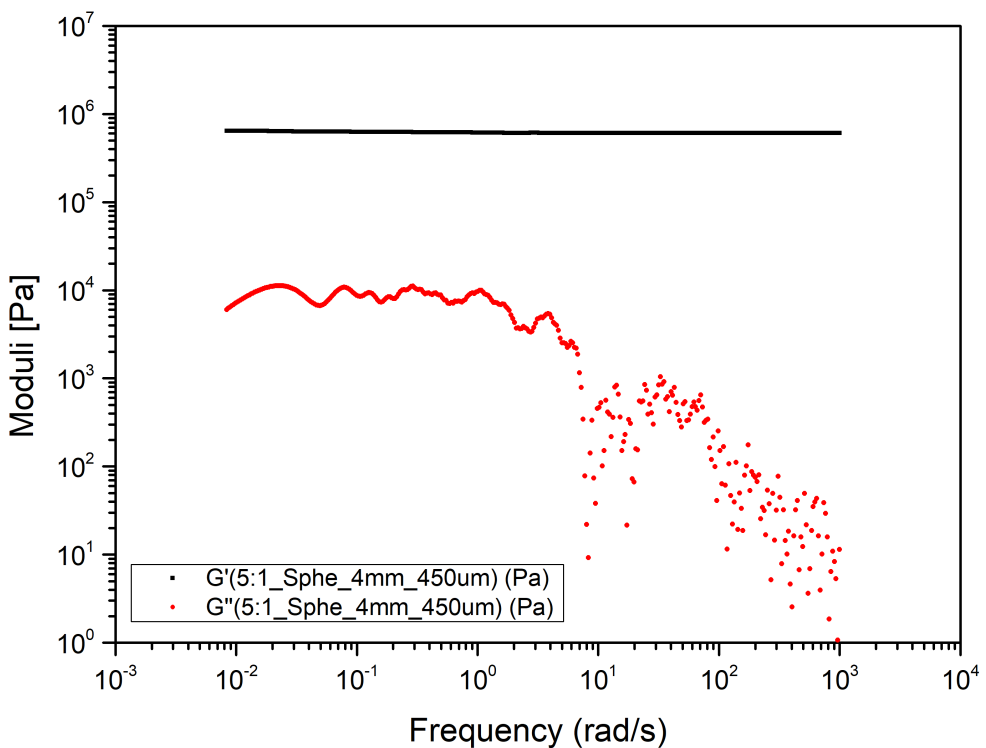


Figure B.29: the 5:1 PDMS sample's viscoelastic moduli derived by means of i-Rheo indentation using spherical indenter with 4mm in diameter and applying 0.45mm depth

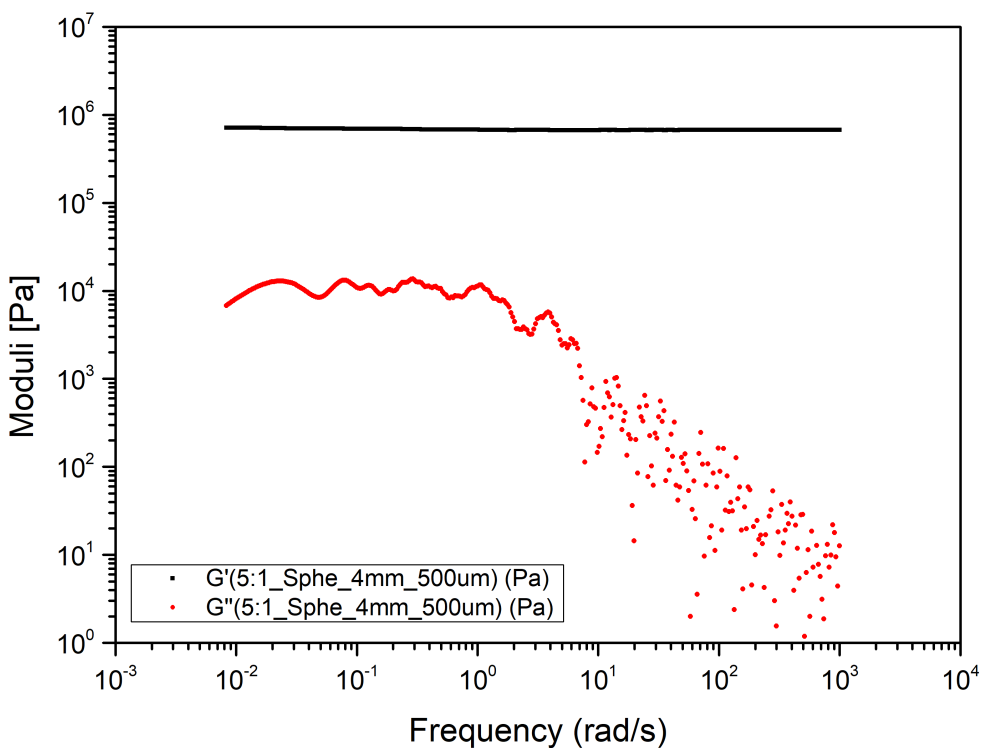


Figure B.30: the 5:1 PDMS sample's viscoelastic moduli derived by means of i-Rheo indentation using spherical indenter with 4mm in diameter and applying 0.5mm depth

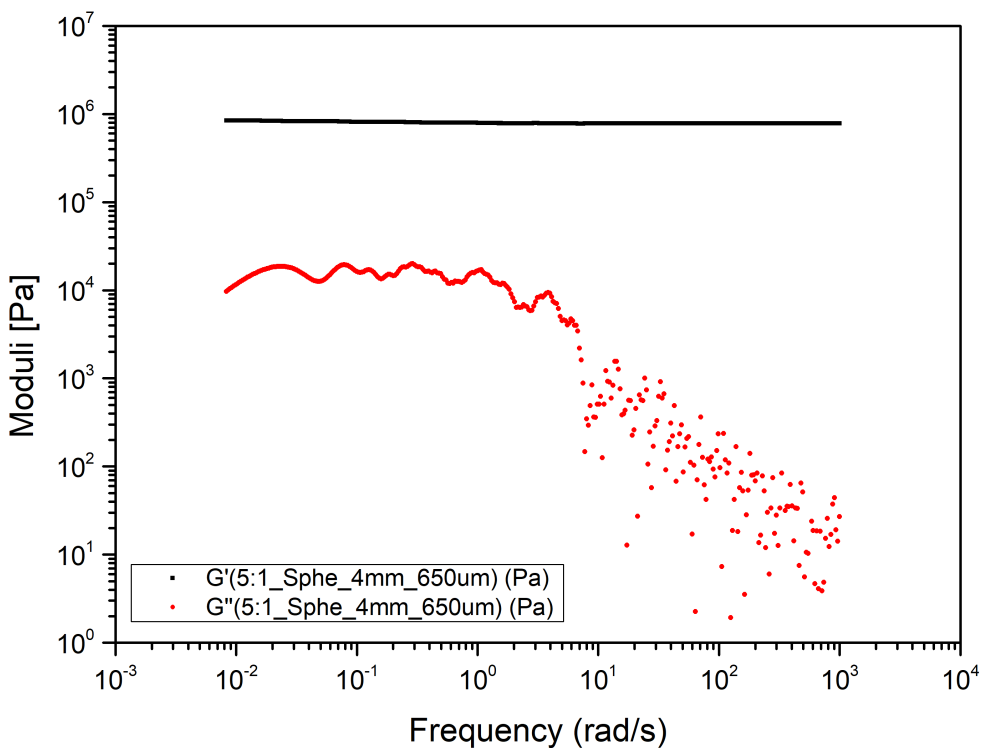


Figure B.31: the 5:1 PDMS sample's viscoelastic moduli derived by means of i-Rheo indentation using spherical indenter with 4mm in diameter and applying 0.65mm depth

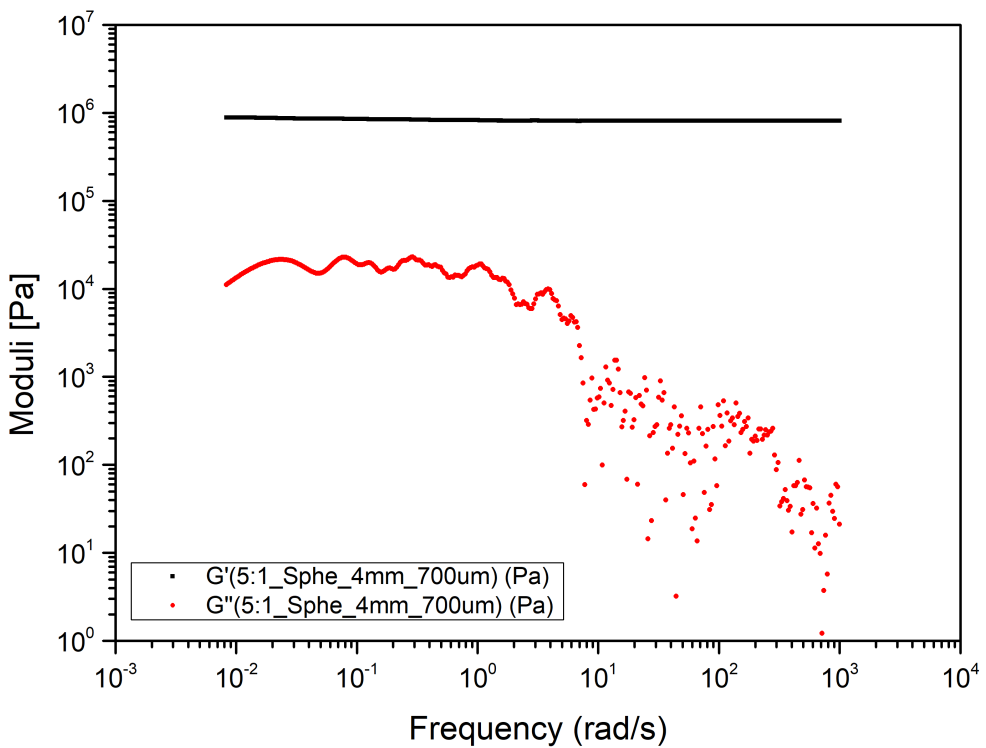


Figure B.32: the 5:1 PDMS sample's viscoelastic moduli derived by means of i-Rheo indentation using spherical indenter with 4mm in diameter and applying 0.7mm depth

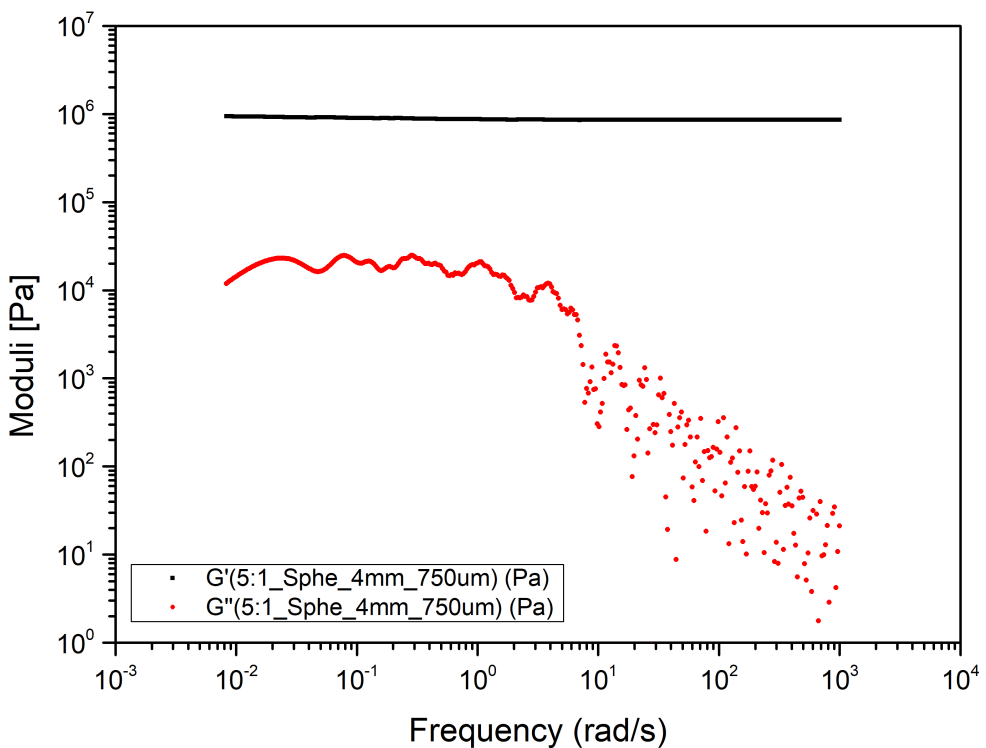


Figure B.33: the 5:1 PDMS sample's viscoelastic moduli derived by means of i-Rheo indentation using spherical indenter with 4mm in diameter and applying 0.75mm depth

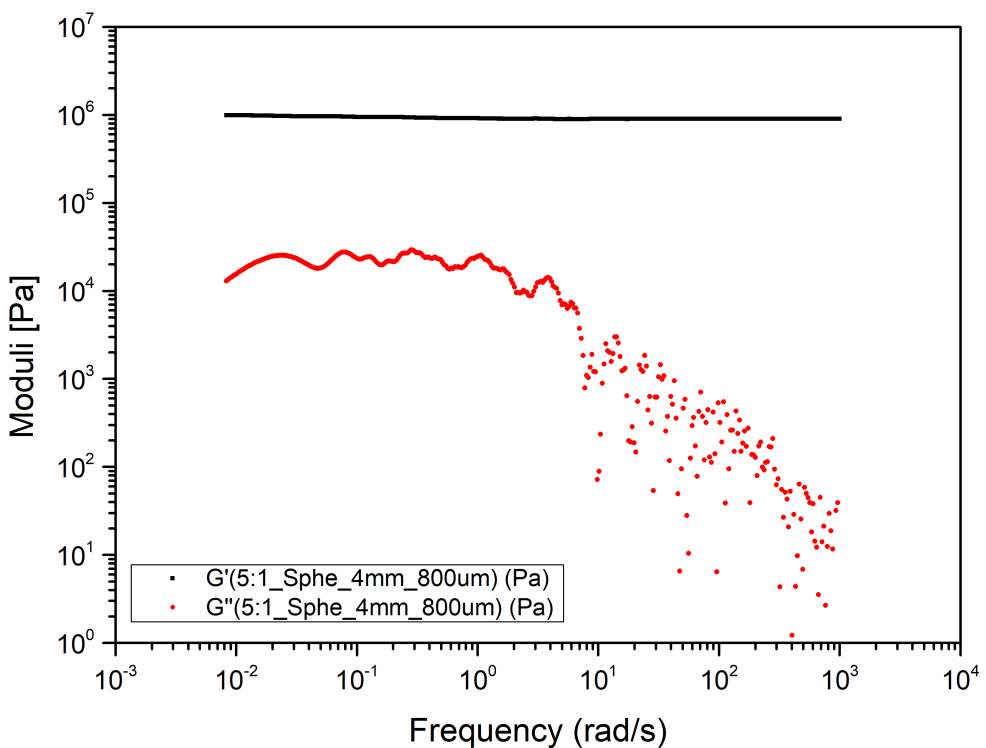


Figure B.34: the 5:1 PDMS sample's viscoelastic moduli derived by means of i-Rheo indentation using spherical indenter with 4mm in diameter and applying 0.8mm depth

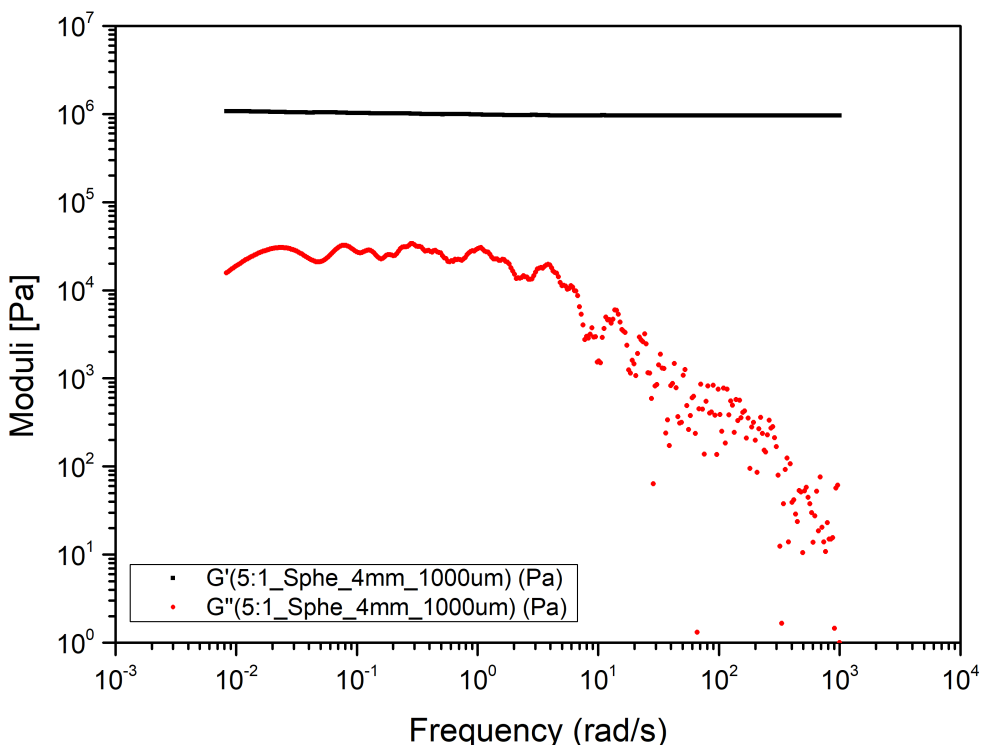


Figure B.35: the 5:1 PDMS sample's viscoelastic moduli derived by means of i-Rheo indentation using spherical indenter with 4mm in diameter and applying 1mm depth

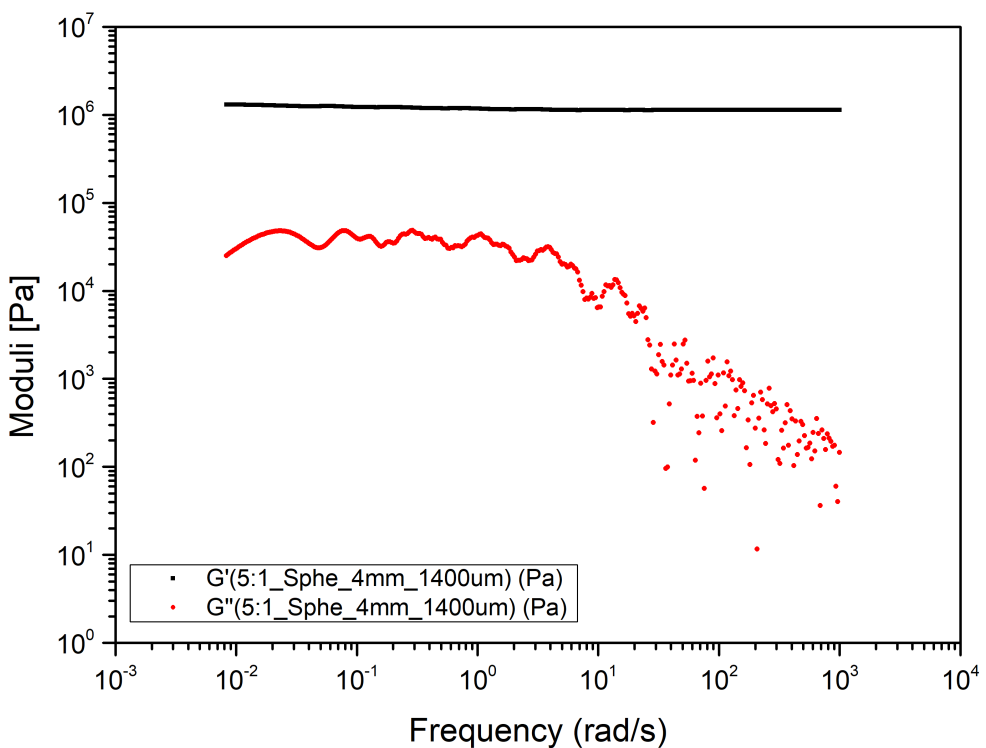


Figure B.36: the 5:1 PDMS sample's viscoelastic moduli derived by means of i-Rheo indentation using spherical indenter with 4mm in diameter and applying 1.4mm depth

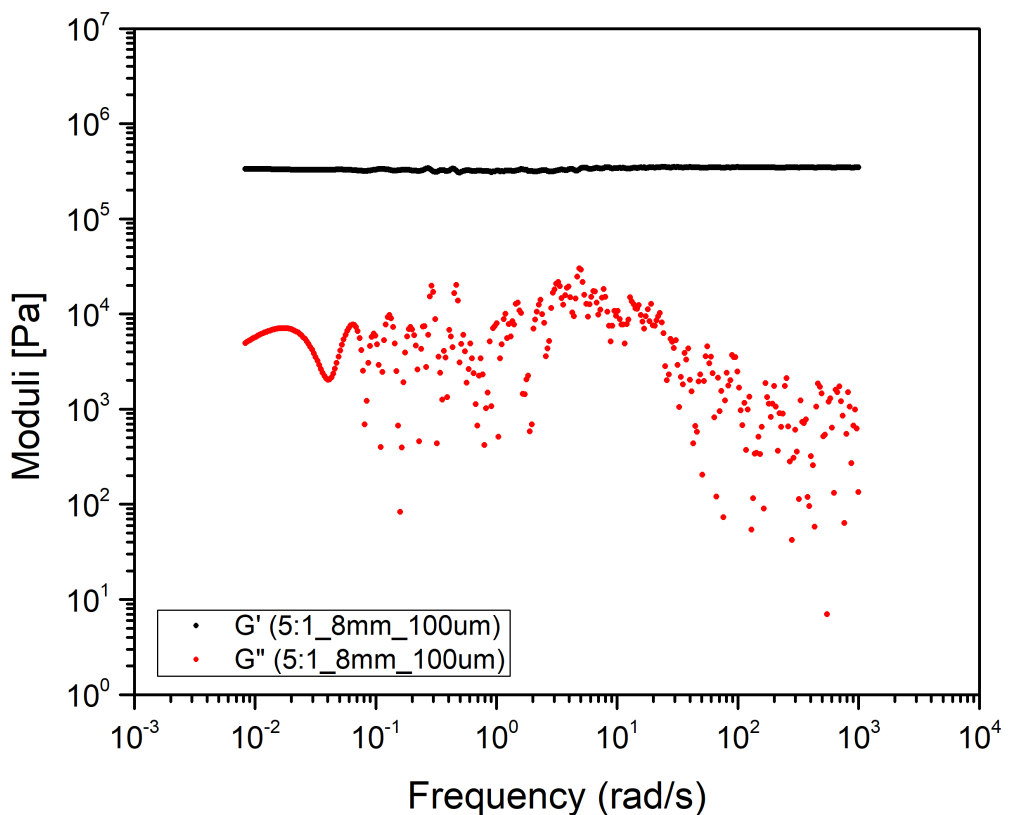


Figure B.37: the 5:1 PDMS sample's viscoelastic moduli derived by means of i-Rheo indentation using spherical indenter with 8mm in diameter and applying 0.1mm depth

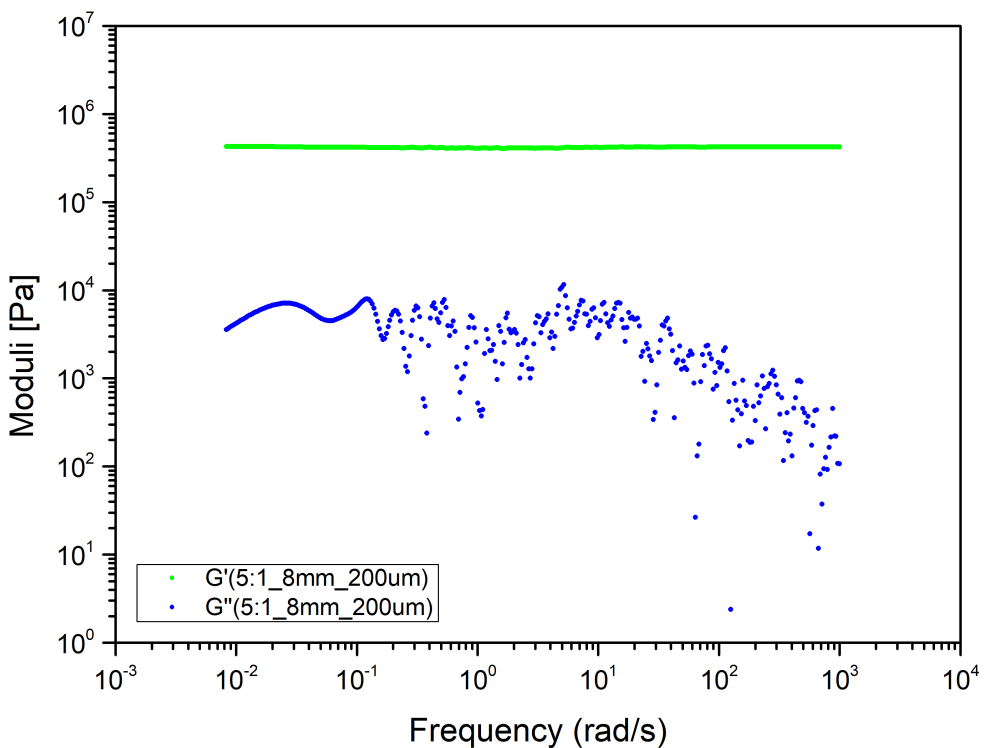


Figure B.38: the 5:1 PDMS sample's viscoelastic moduli derived by means of i-Rheo indentation using spherical indenter with 8mm in diameter and applying 0.2mm depth

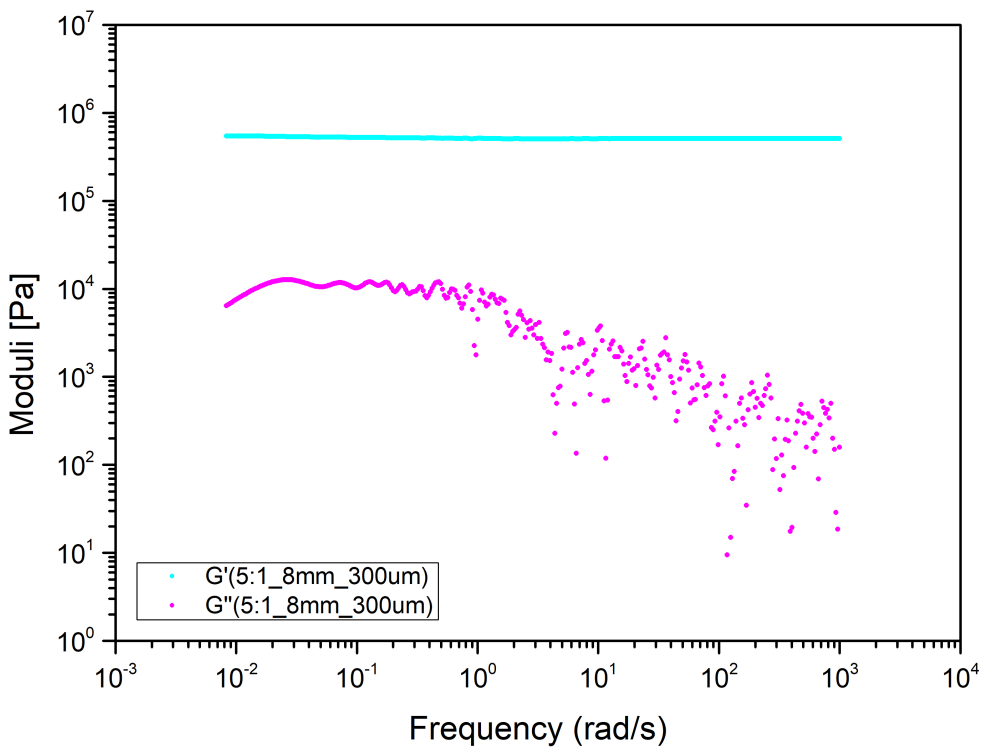


Figure B.39: the 5:1 PDMS sample's viscoelastic moduli derived by means of i-Rheo indentation using spherical indenter with 8mm in diameter and applying 0.3mm depth

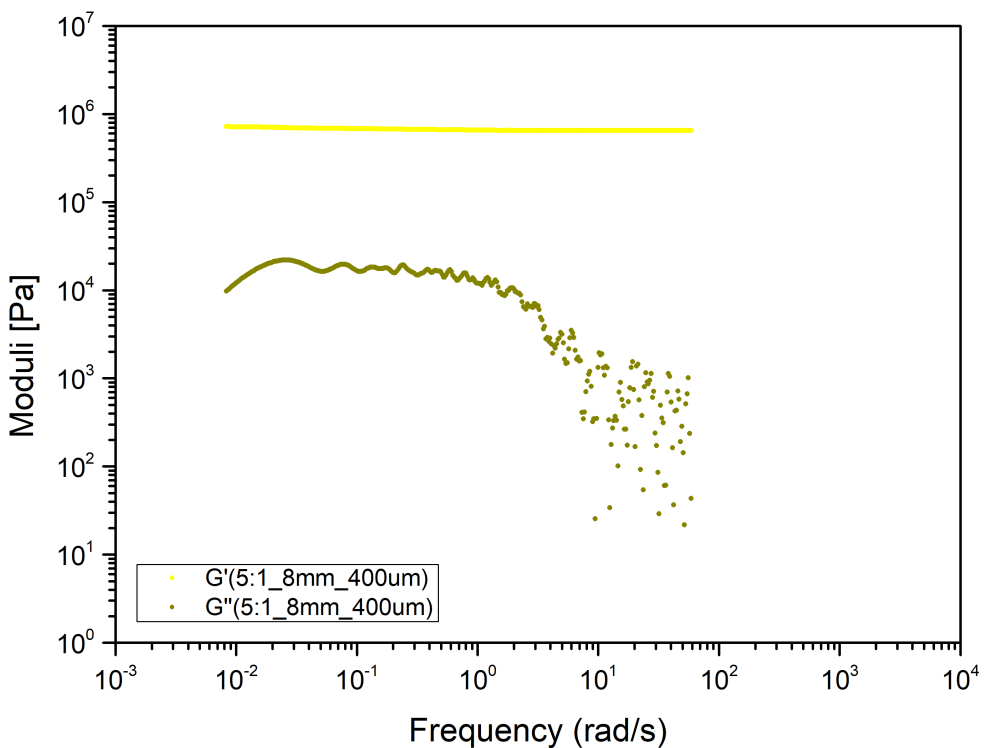


Figure B.40: the 5:1 PDMS sample's viscoelastic moduli derived by means of i-Rheo indentation using spherical indenter with 8mm in diameter and applying 0.4mm depth

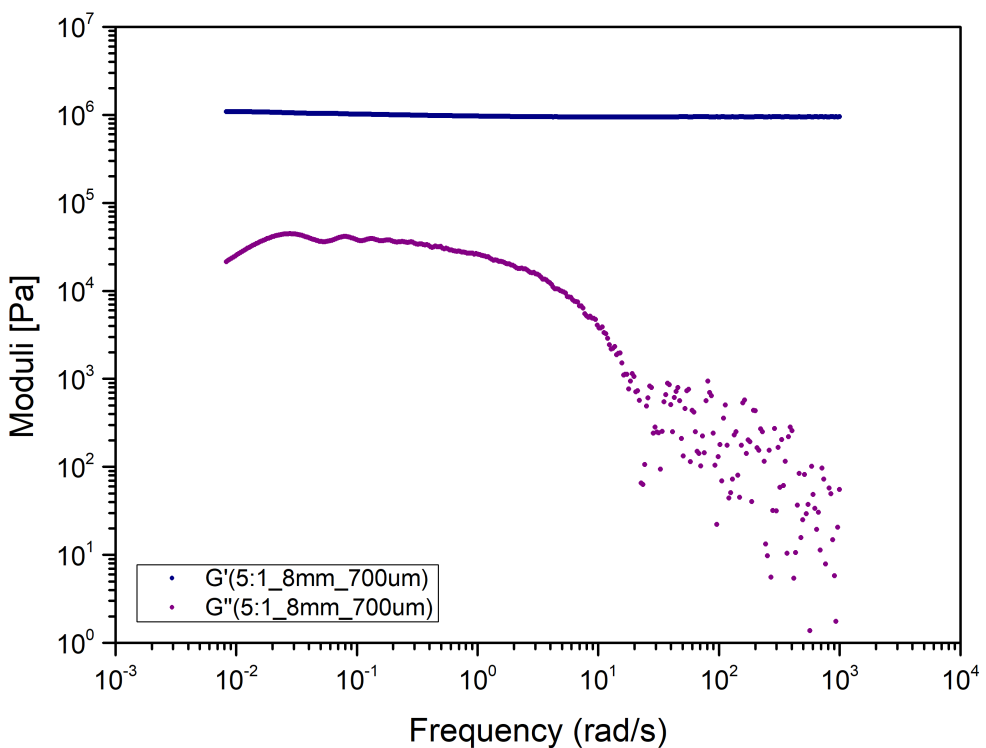


Figure B.41: the 5:1 PDMS sample's viscoelastic moduli derived by means of i-Rheo indentation using spherical indenter with 8mm in diameter and applying 0.7mm depth

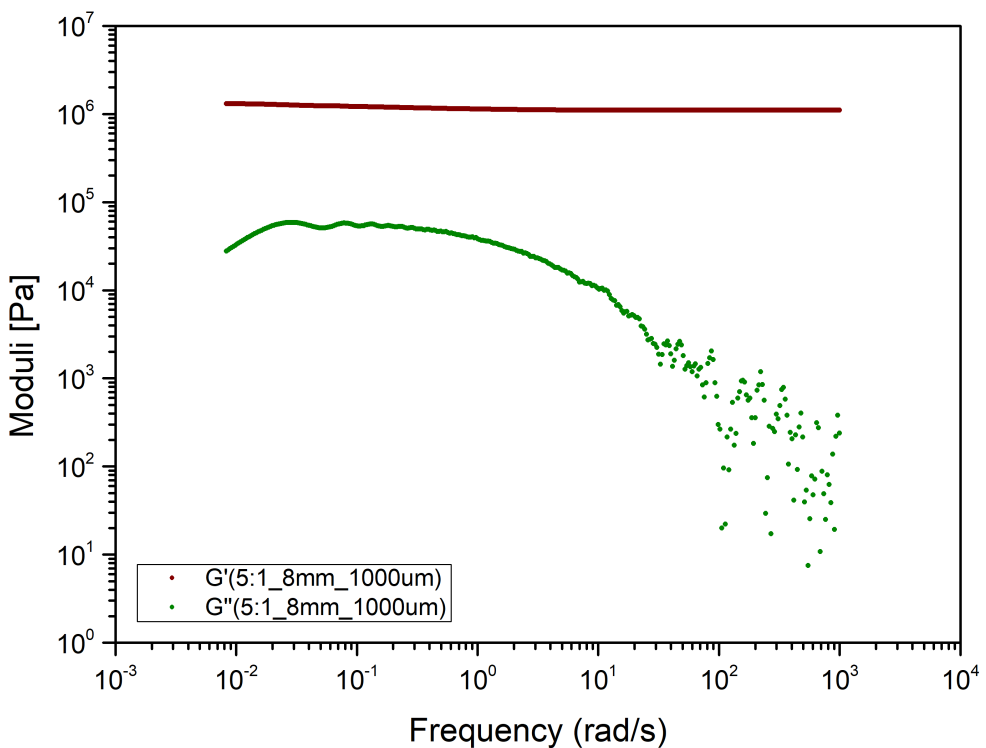


Figure B.42: the 5:1 PDMS sample's viscoelastic moduli derived by means of i-Rheo indentation using spherical indenter with 8mm in diameter and applying 1mm depth

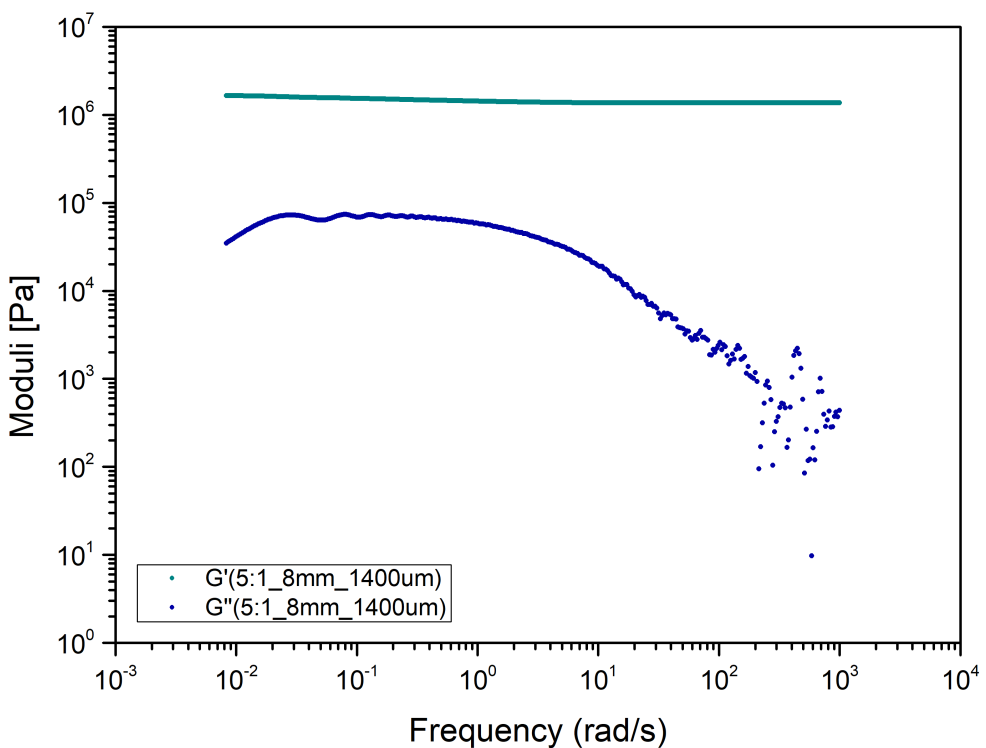


Figure B.43: the 5:1 PDMS sample's viscoelastic moduli derived by means of i-Rheo indentation using spherical indenter with 8mm in diameter and applying 1.4mm depth

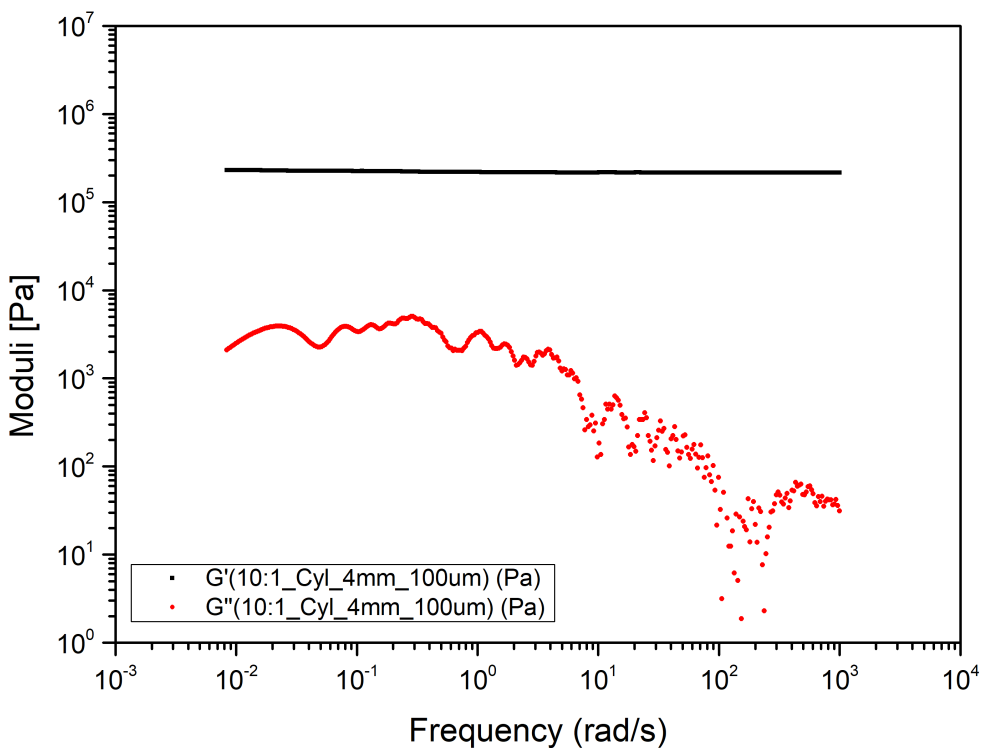


Figure B.44: the 10:1 PDMS sample's viscoelastic moduli derived by means of i-Rheo indentation using cylindrical indenter with 4mm in diameter and applying 0.1mm depth

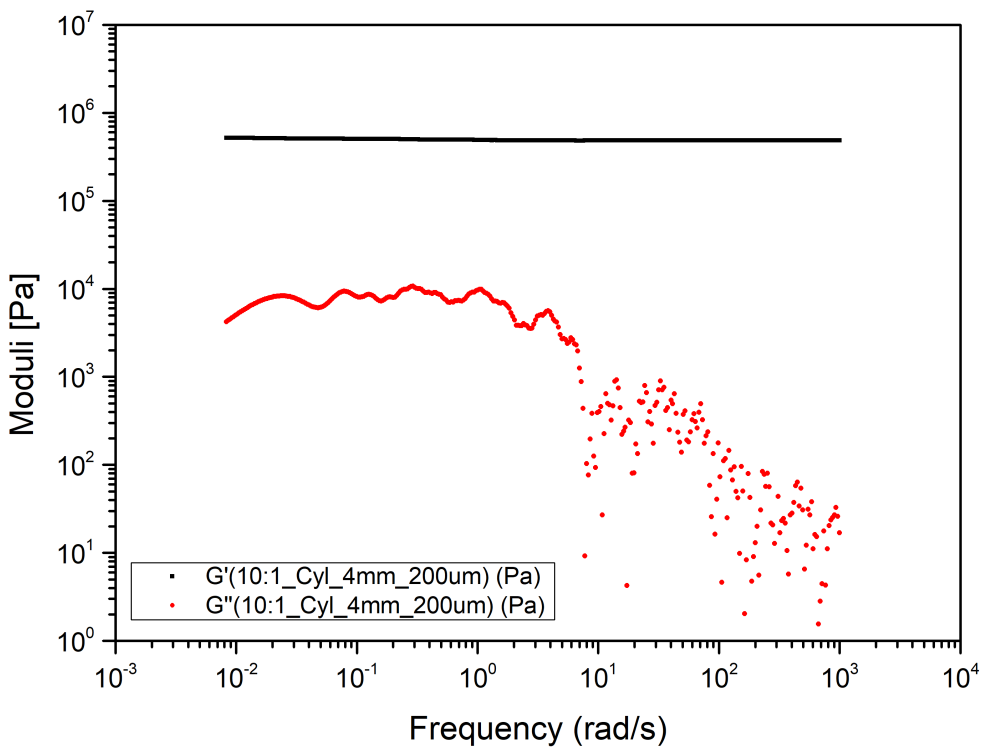


Figure B.45: the 10:1 PDMS sample's viscoelastic moduli derived by means of i-Rheo indentation using cylindrical indenter with 4mm in diameter and applying 0.2mm depth

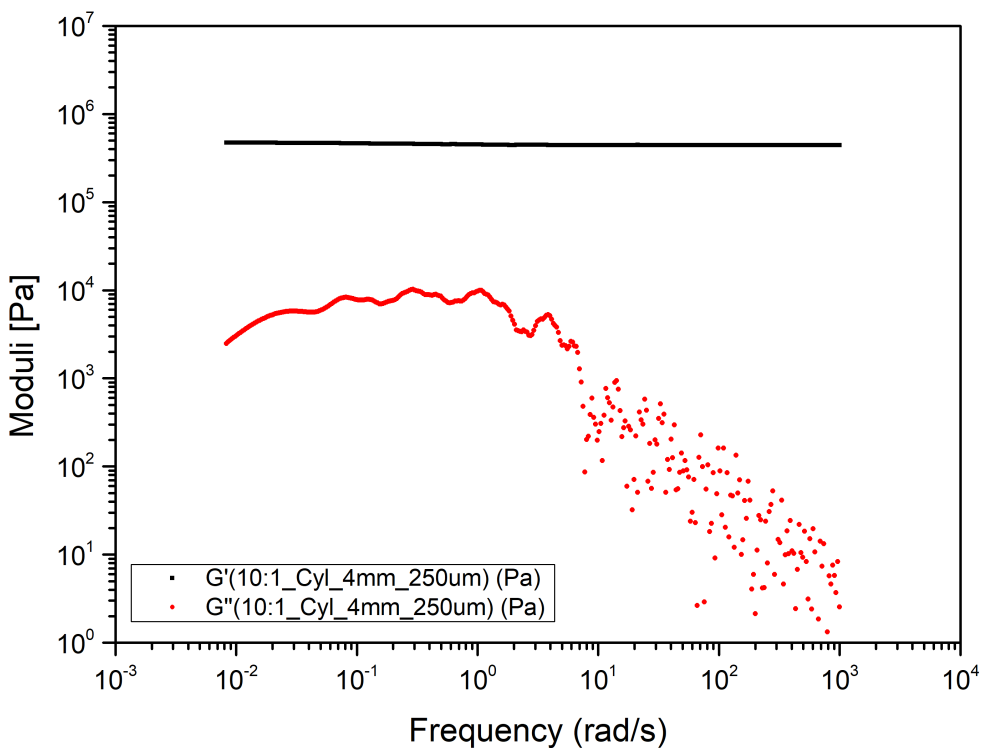


Figure B.46: the 10:1 PDMS sample's viscoelastic moduli derived by means of i-Rheo indentation using cylindrical indenter with 4mm in diameter and applying 0.25mm depth

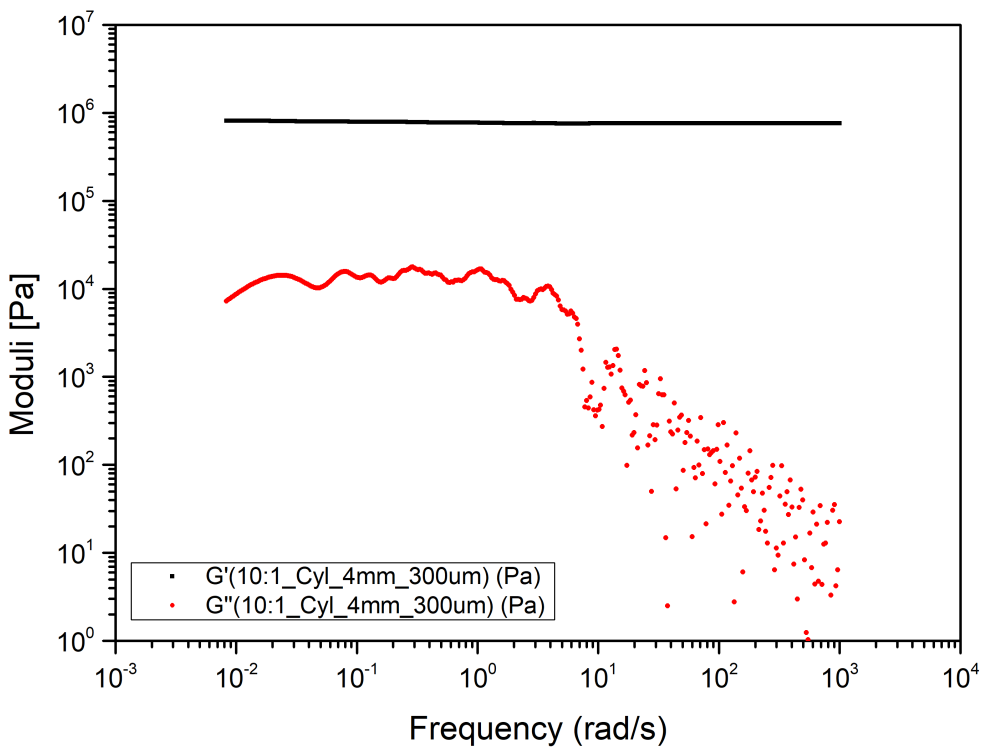


Figure B.47: the 10:1 PDMS sample's viscoelastic moduli derived by means of i-Rheo indentation using cylindrical indenter with 4mm in diameter and applying 0.3mm depth

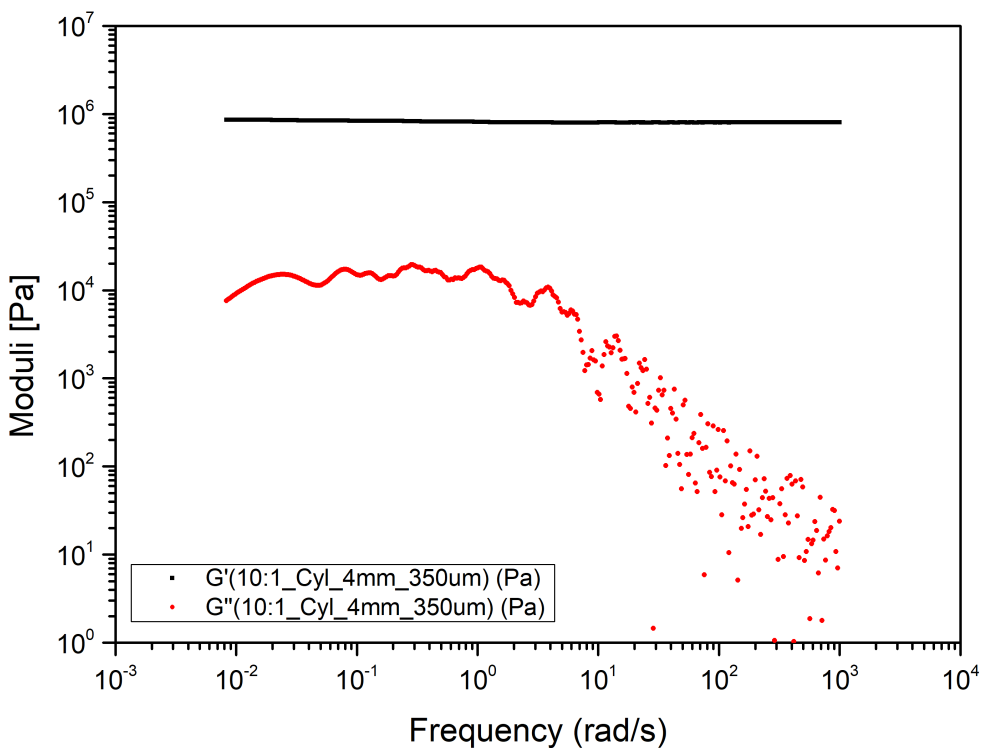


Figure B.48: the 10:1 PDMS sample's viscoelastic moduli derived by means of i-Rheo indentation using cylindrical indenter with 4mm in diameter and applying 0.35mm depth

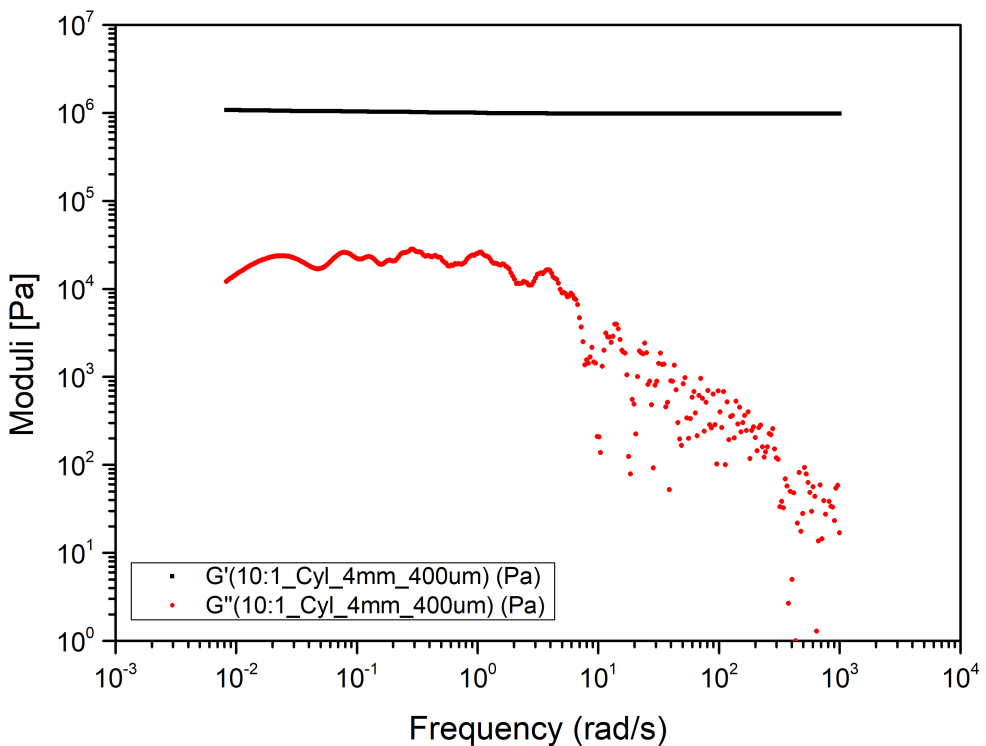


Figure B.49: the 10:1 PDMS sample's viscoelastic moduli derived by means of i-Rheo indentation using cylindrical indenter with 4mm in diameter and applying 0.4mm depth

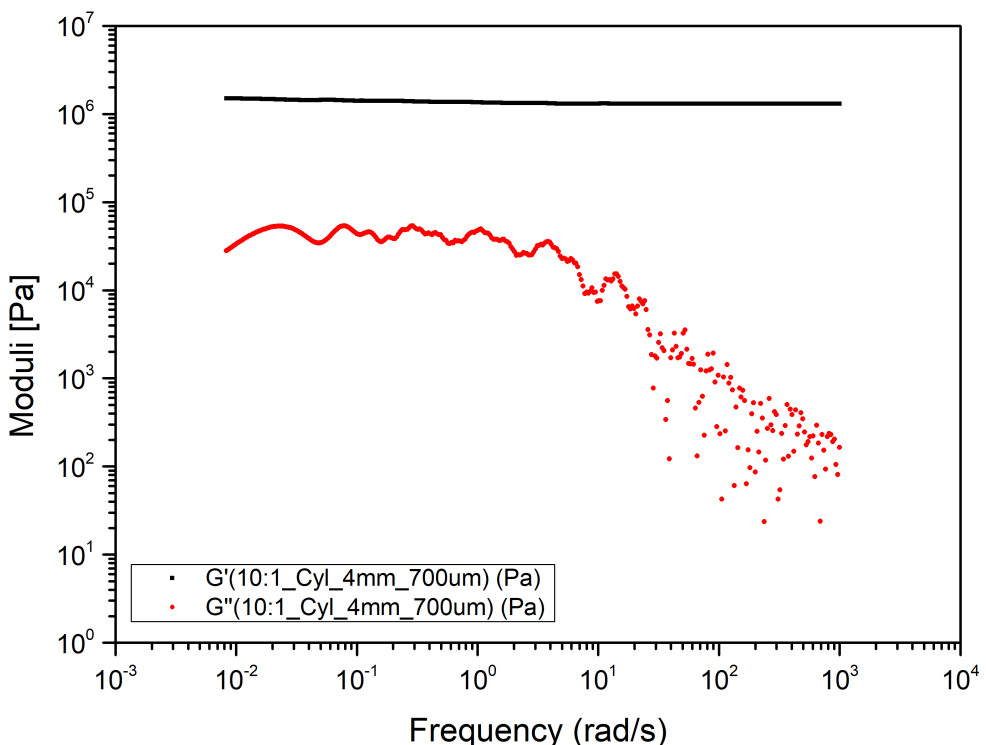


Figure B.50: the 10:1 PDMS sample's viscoelastic moduli derived by means of i-Rheo indentation using cylindrical indenter with 4mm in diameter and applying 0.7mm depth

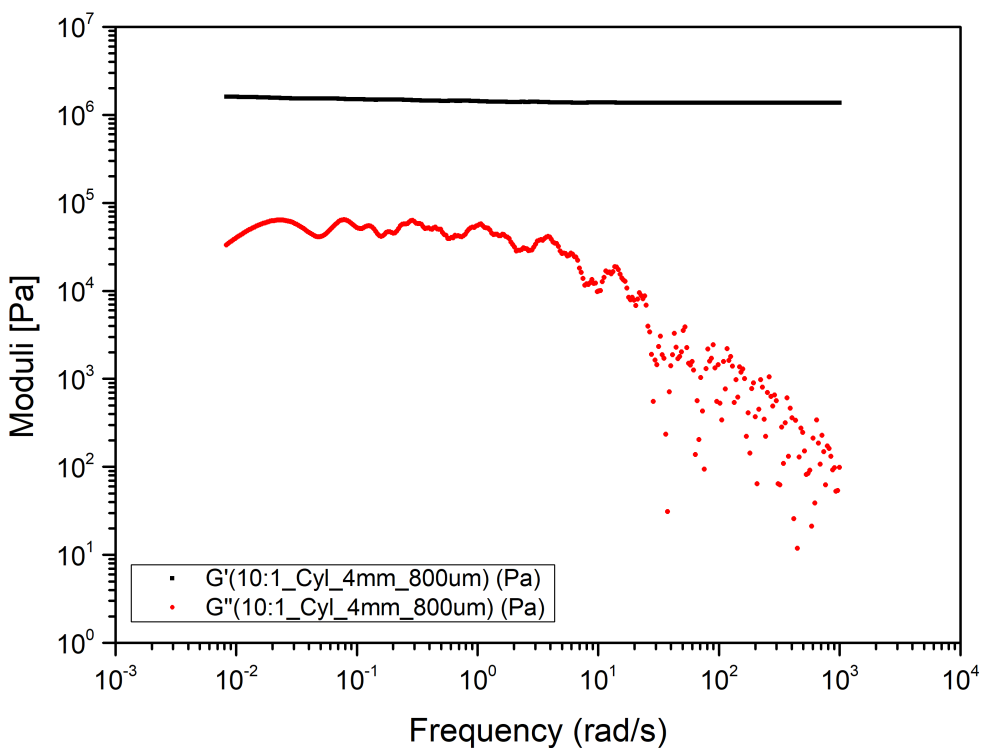


Figure B.51: the 10:1 PDMS sample's viscoelastic moduli derived by means of i-Rheo indentation using cylindrical indenter with 4mm in diameter and applying 0.8mm depth

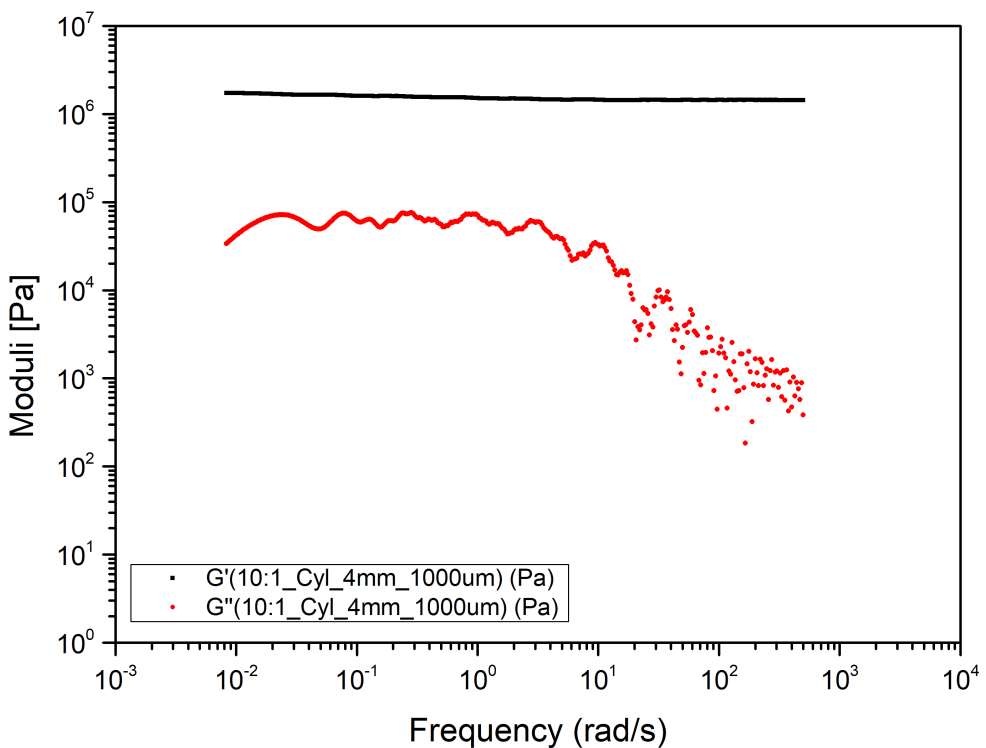


Figure B.52: the 10:1 PDMS sample's viscoelastic moduli derived by means of i-Rheo indentation using cylindrical indenter with 4mm in diameter and applying 1mm depth

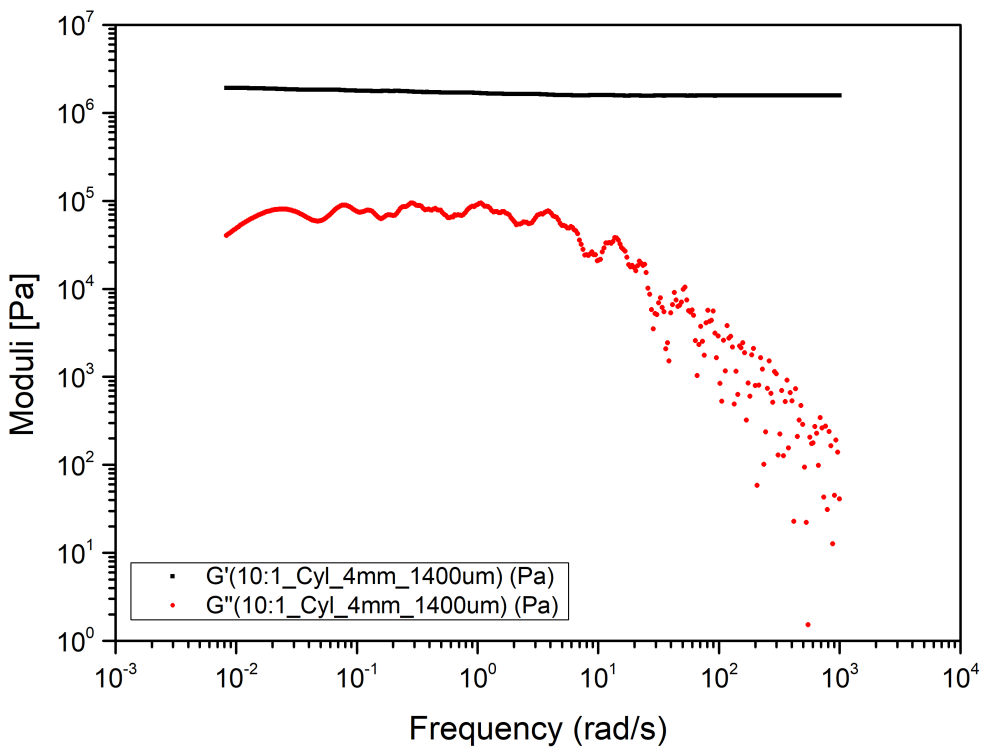


Figure B.53: the 10:1 PDMS sample's viscoelastic moduli derived by means of i-Rheo indentation using cylindrical indenter with 4mm in diameter and applying 1.4mm depth

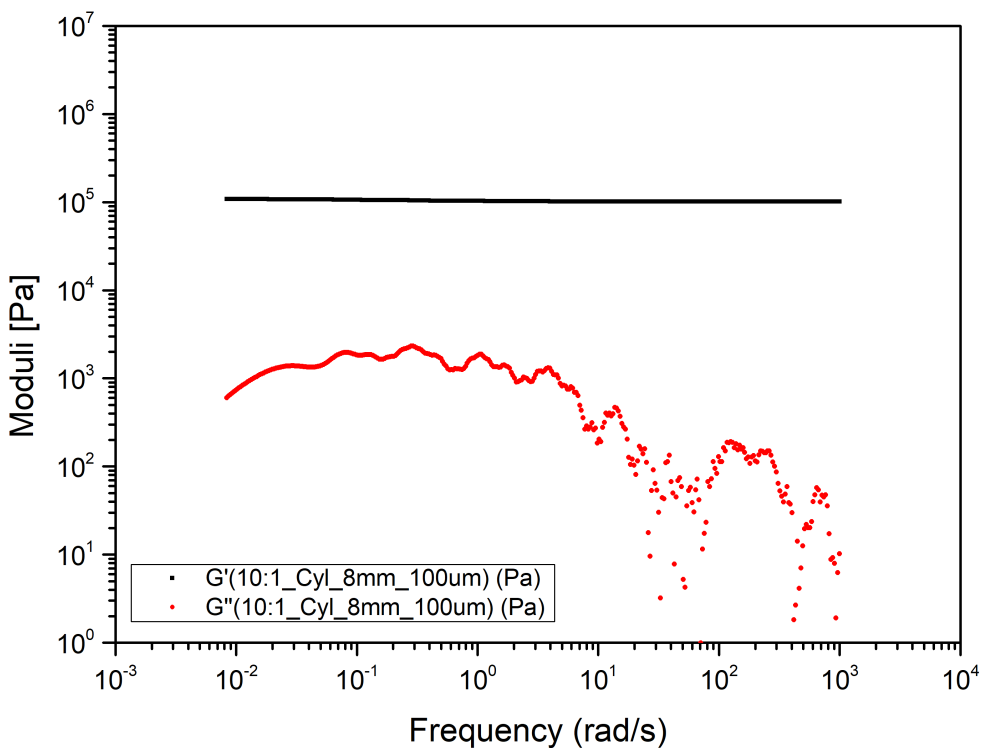


Figure B.54: the 10:1 PDMS sample's viscoelastic moduli derived by means of i-Rheo indentation using cylindrical indenter with 8mm in diameter and applying 0.1mm depth

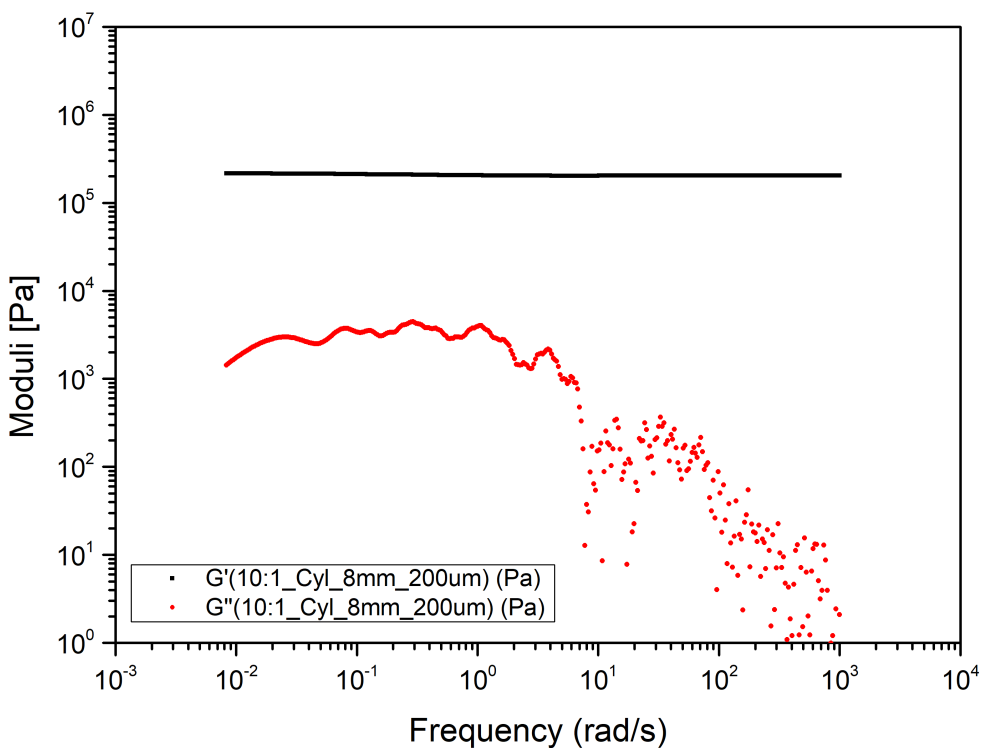


Figure B.55: the 10:1 PDMS sample's viscoelastic moduli derived by means of i-Rheo indentation using cylindrical indenter with 8mm in diameter and applying 0.2mm depth

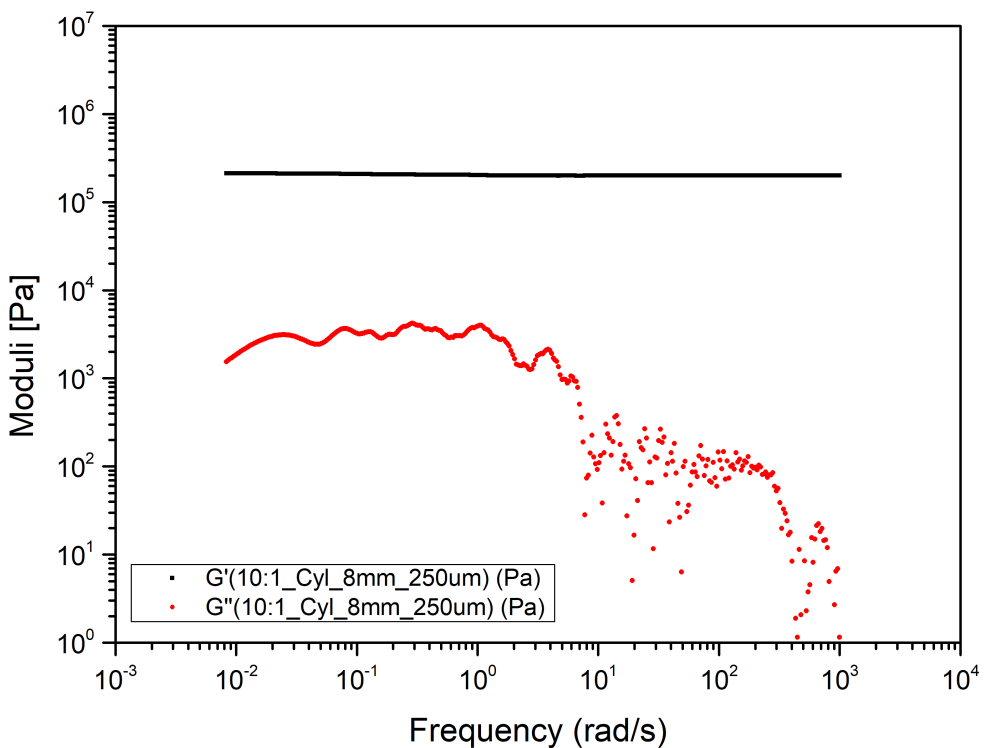


Figure B.56: the 10:1 PDMS sample's viscoelastic moduli derived by means of i-Rheo indentation using cylindrical indenter with 8mm in diameter and applying 0.25mm depth

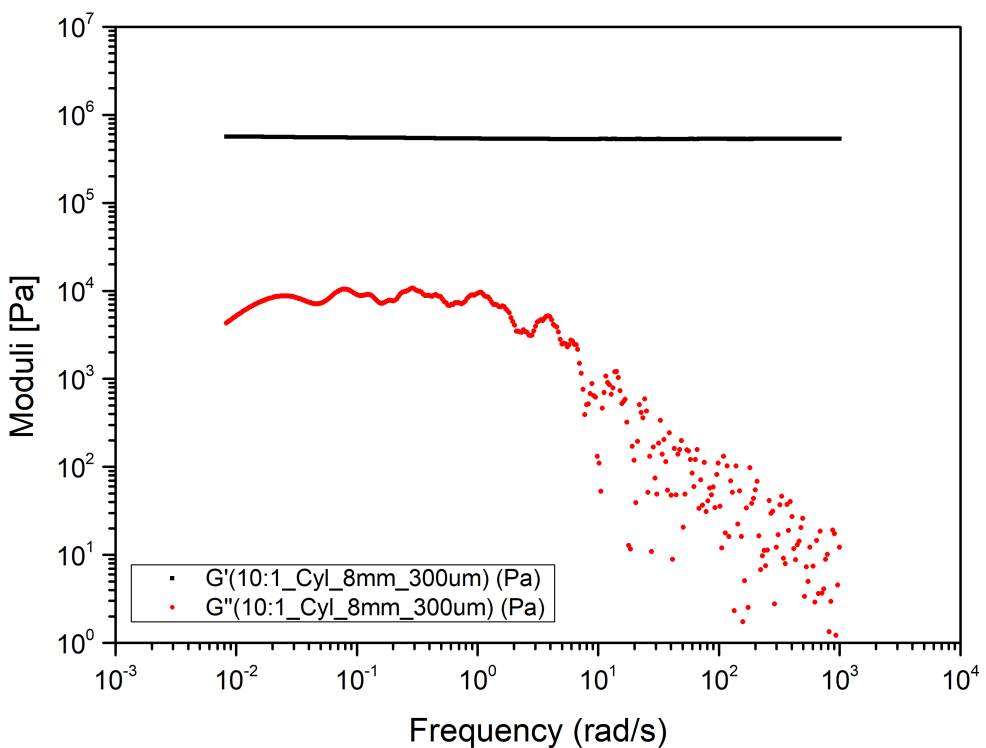


Figure B.57: the 10:1 PDMS sample's viscoelastic moduli derived by means of i-Rheo indentation using cylindrical indenter with 8mm in diameter and applying 0.3mm depth

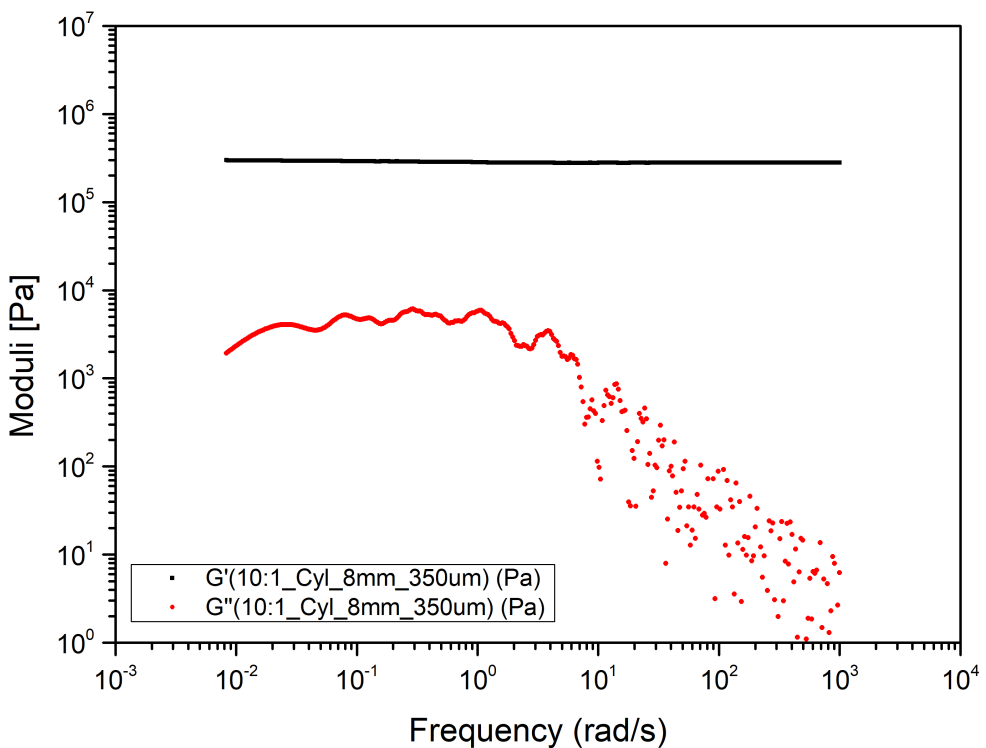


Figure B.58: the 10:1 PDMS sample's viscoelastic moduli derived by means of i-Rheo indentation using cylindrical indenter with 8mm in diameter and applying 0.35mm depth

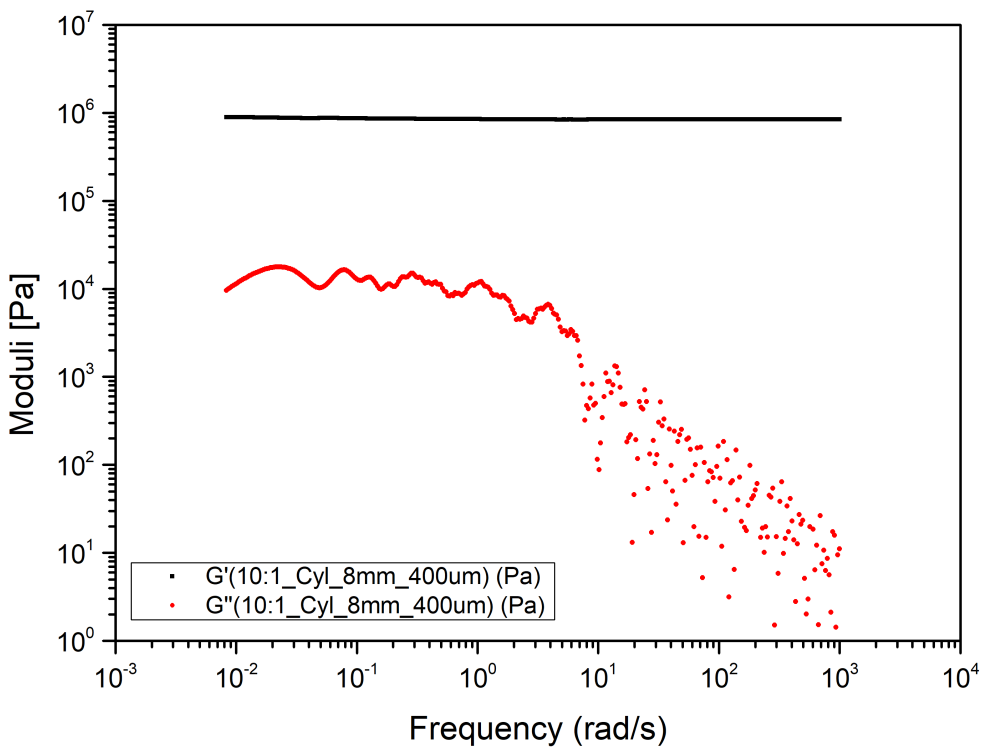


Figure B.59: the 10:1 PDMS sample's viscoelastic moduli derived by means of i-Rheo indentation using cylindrical indenter with 8mm in diameter and applying 0.4mm depth

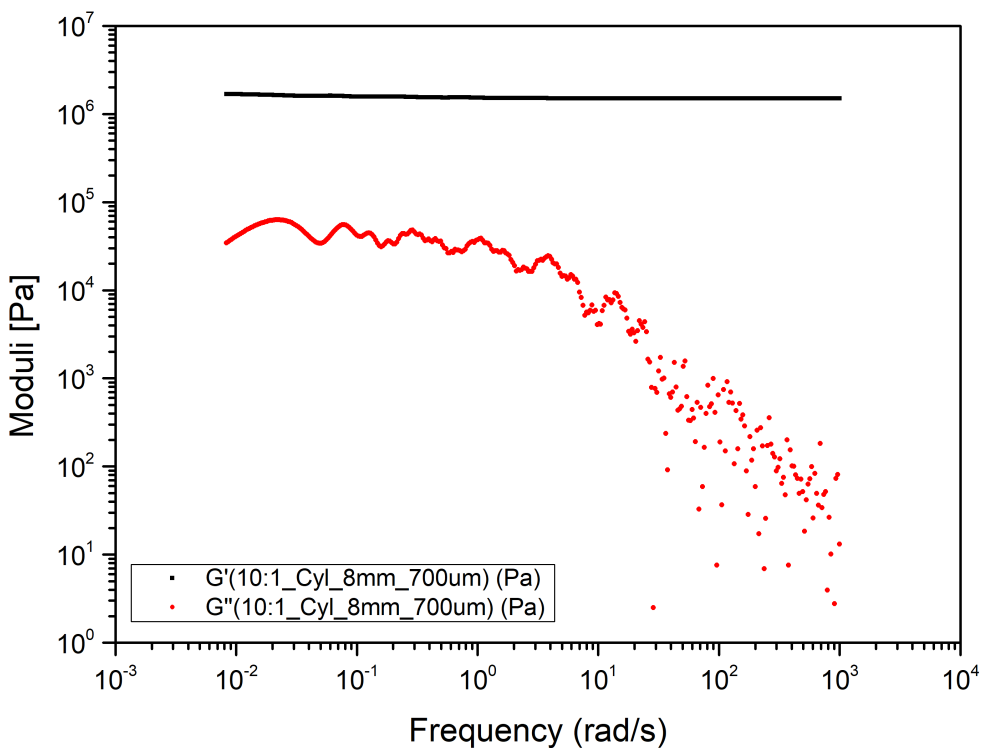


Figure B.60: the 10:1 PDMS sample's viscoelastic moduli derived by means of i-Rheo indentation using cylindrical indenter with 8mm in diameter and applying 0.7mm depth

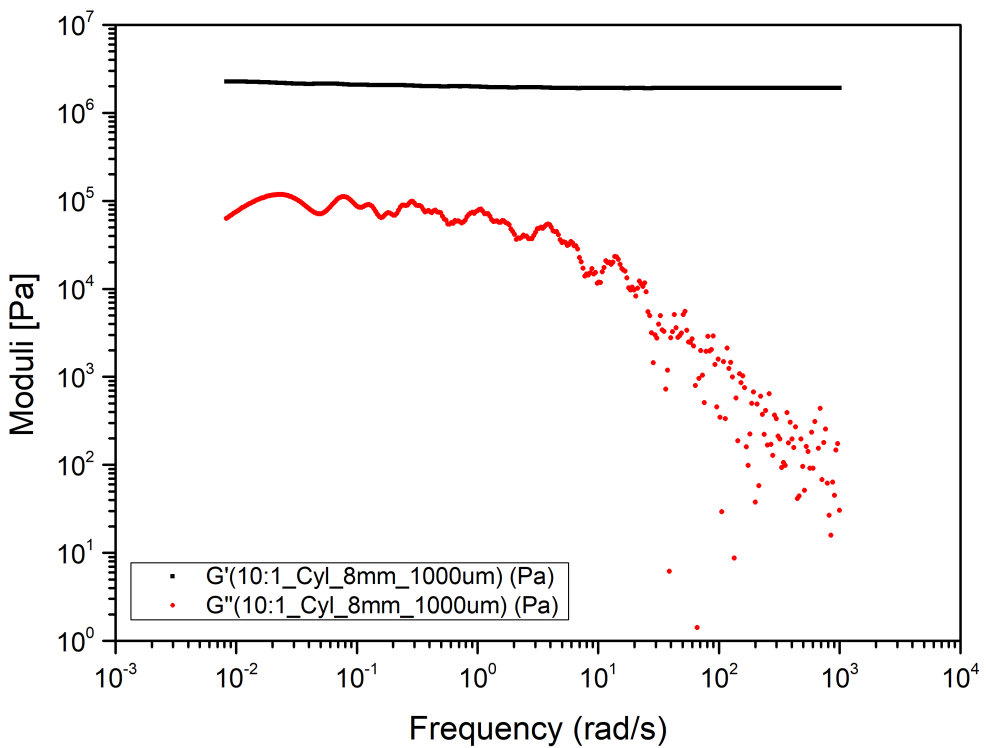


Figure B.61: the 10:1 PDMS sample's viscoelastic moduli derived by means of i-Rheo indentation using cylindrical indenter with 8mm in diameter and applying 1mm depth

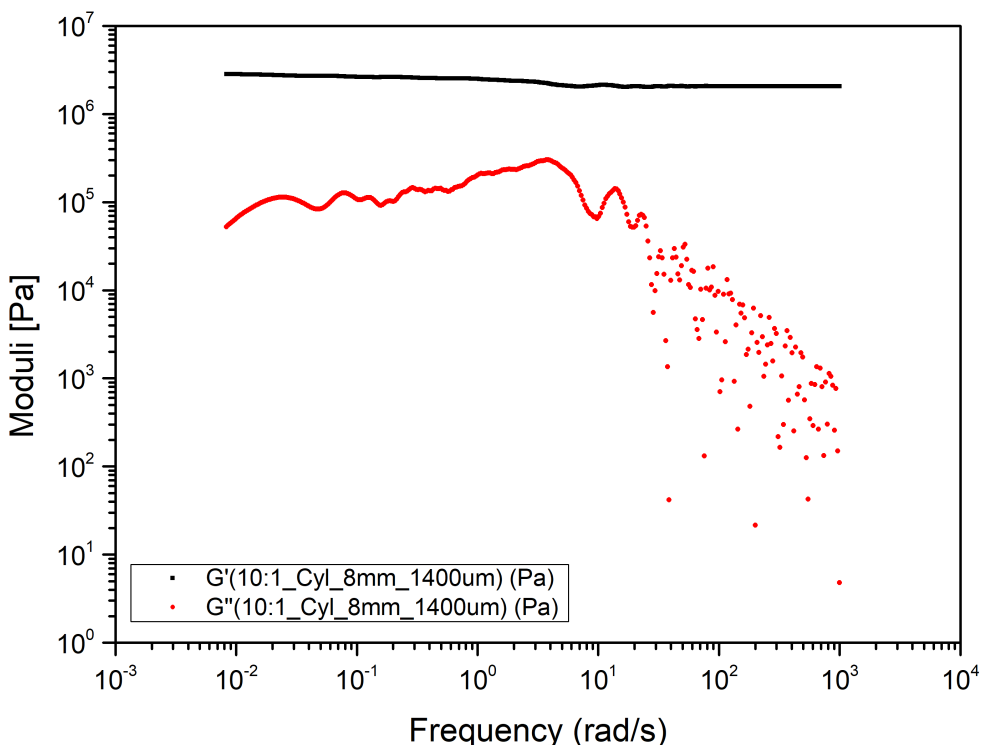


Figure B.62: the 10:1 PDMS sample's viscoelastic moduli derived by means of i-Rheo indentation using cylindrical indenter with 8mm in diameter and applying 1.4mm depth

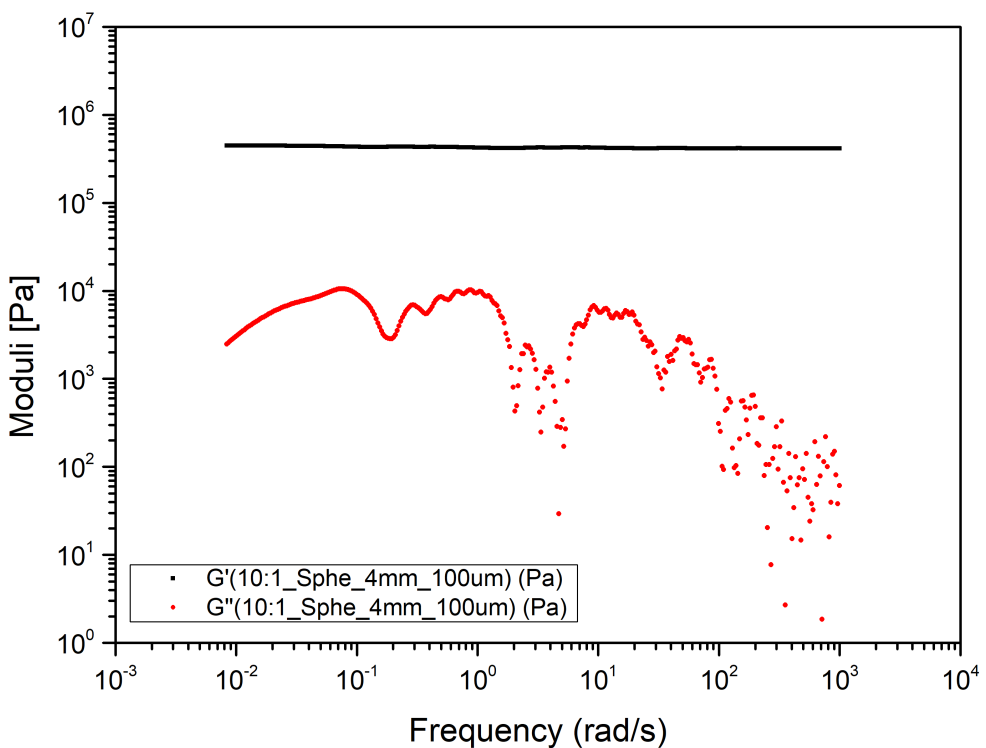


Figure B.63: the 10:1 PDMS sample's viscoelastic moduli derived by means of i-Rheo indentation using spherical indenter with 4mm in diameter and applying 0.1mm depth

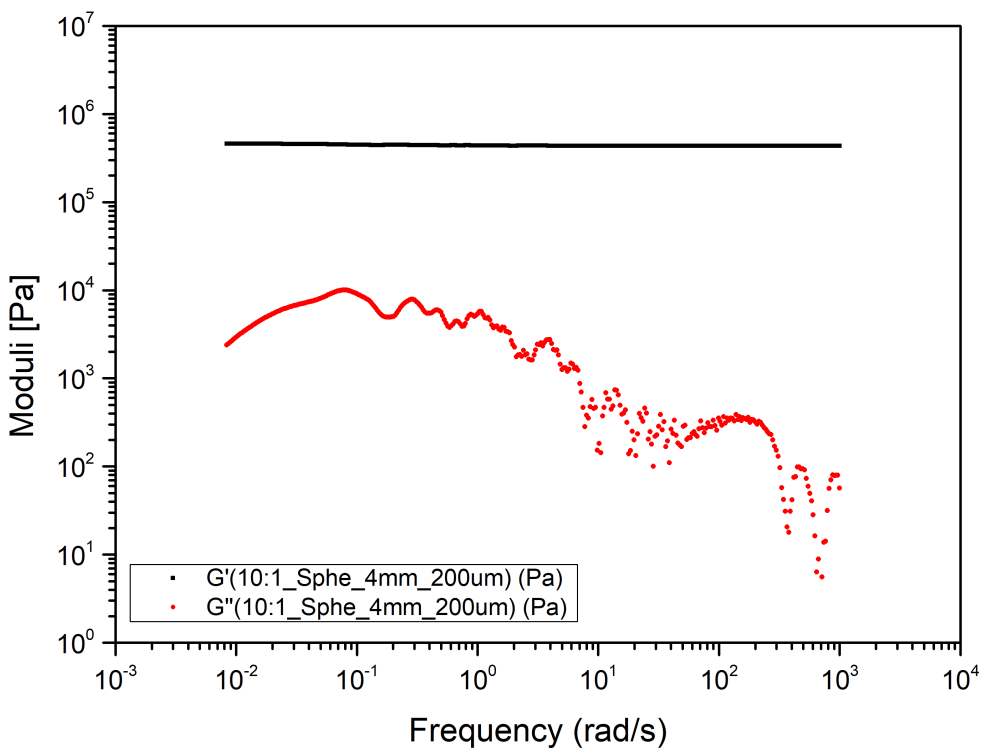


Figure B.64: the 10:1 PDMS sample's viscoelastic moduli derived by means of i-Rheo indentation using spherical indenter with 4mm in diameter and applying 0.2mm depth

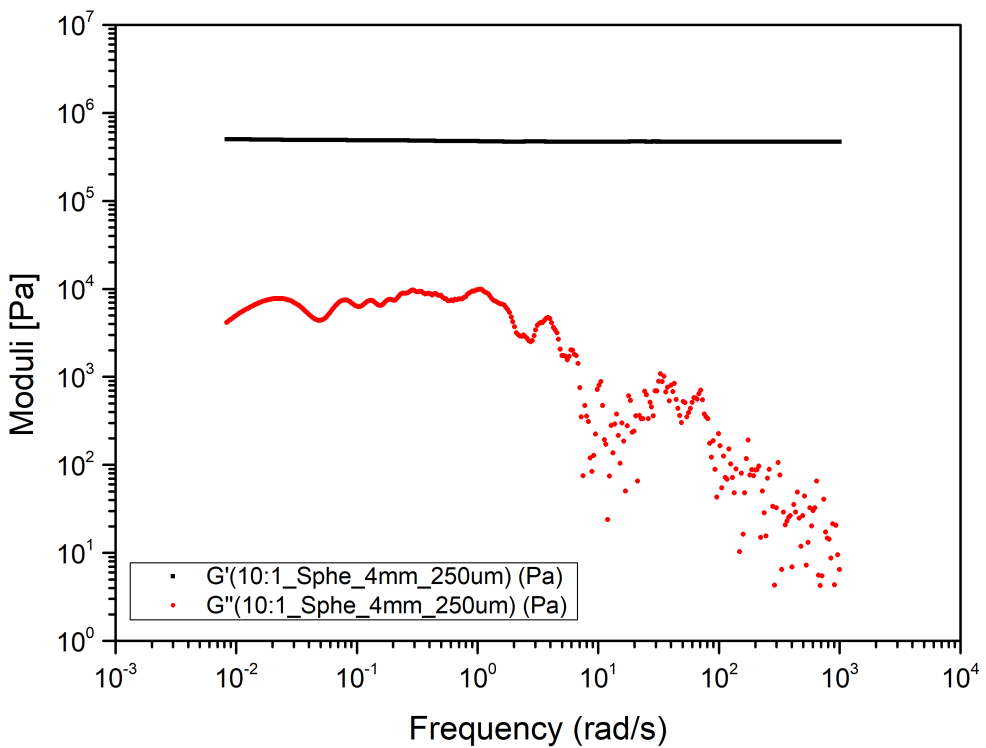


Figure B.65: the 10:1 PDMS sample's viscoelastic moduli derived by means of i-Rheo indentation using spherical indenter with 4mm in diameter and applying 0.25mm depth

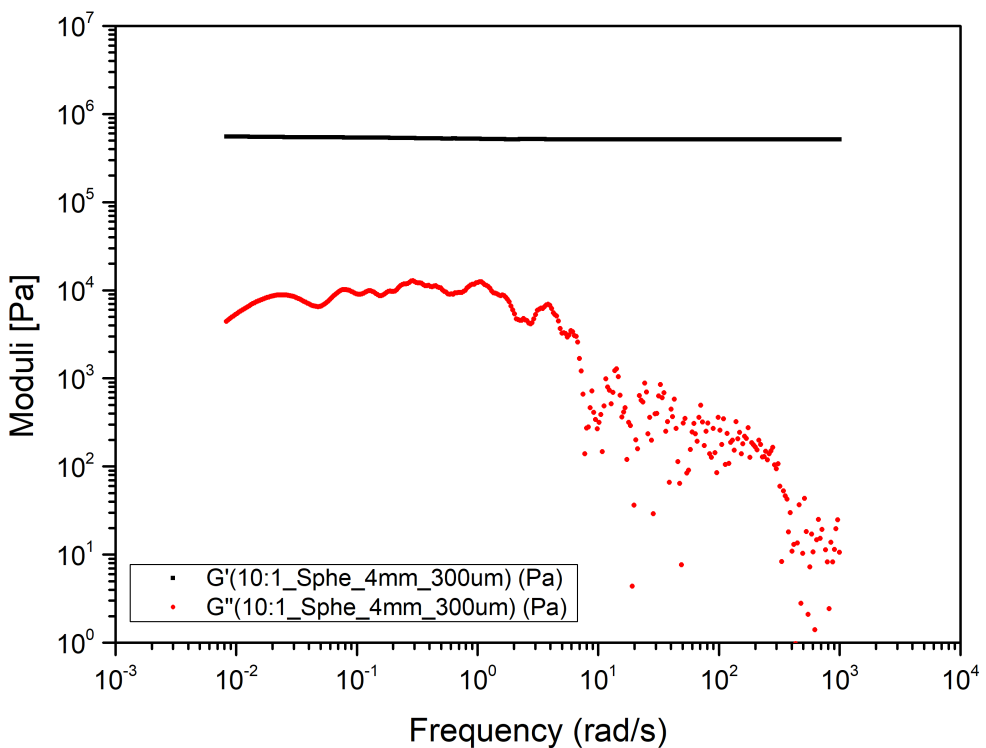


Figure B.66: the 10:1 PDMS sample's viscoelastic moduli derived by means of i-Rheo indentation using spherical indenter with 4mm in diameter and applying 0.3mm depth

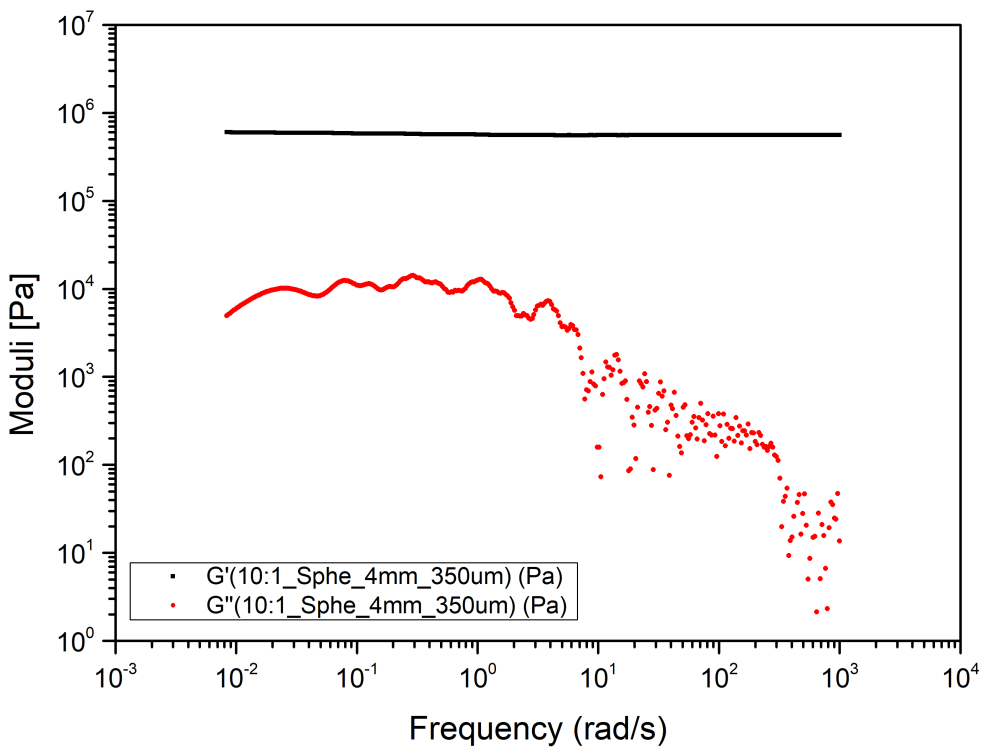


Figure B.67: the 10:1 PDMS sample's viscoelastic moduli derived by means of i-Rheo indentation using spherical indenter with 4mm in diameter and applying 0.35mm depth

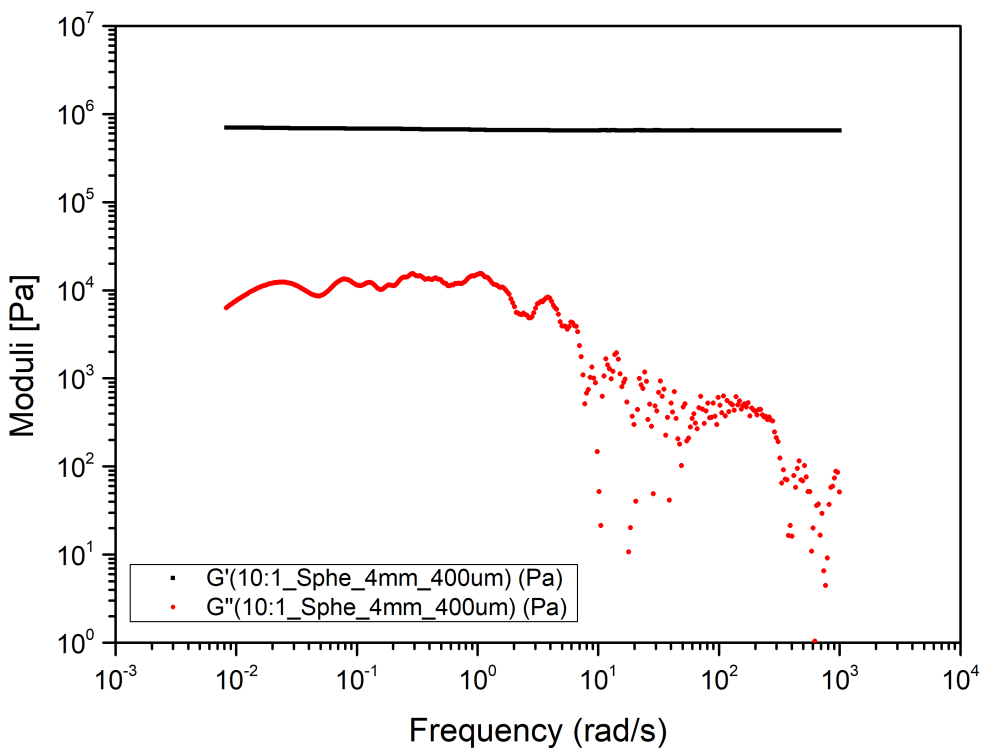


Figure B.68: the 10:1 PDMS sample's viscoelastic moduli derived by means of i-Rheo indentation using spherical indenter with 4mm in diameter and applying 0.4mm depth

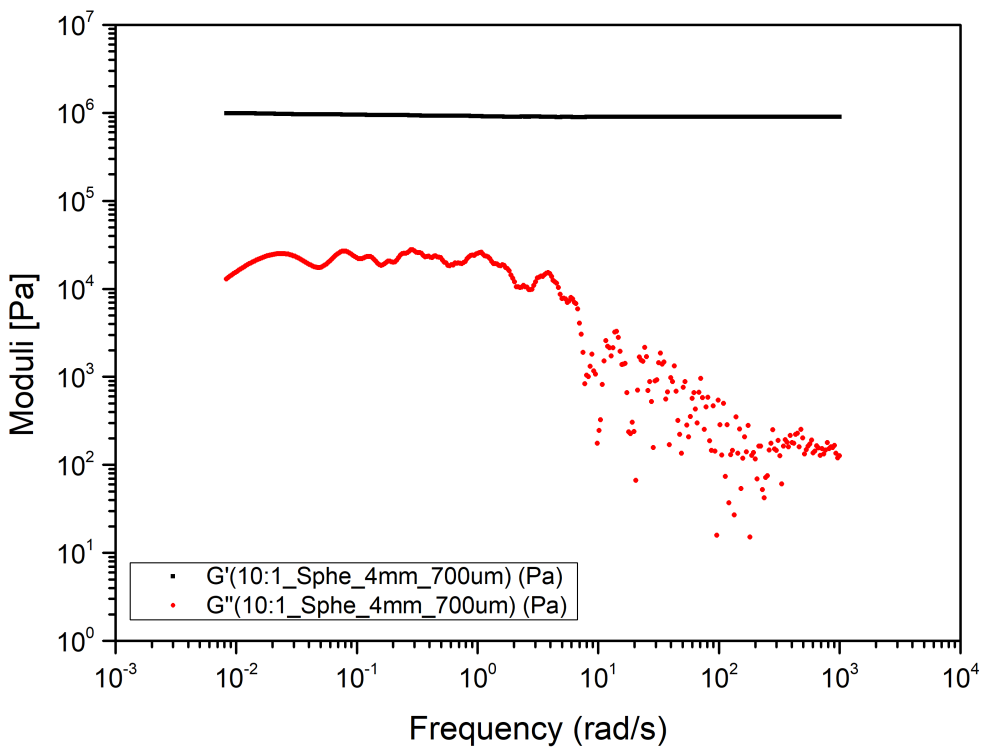


Figure B.69: the 10:1 PDMS sample's viscoelastic moduli derived by means of i-Rheo indentation using spherical indenter with 4mm in diameter and applying 0.7mm depth

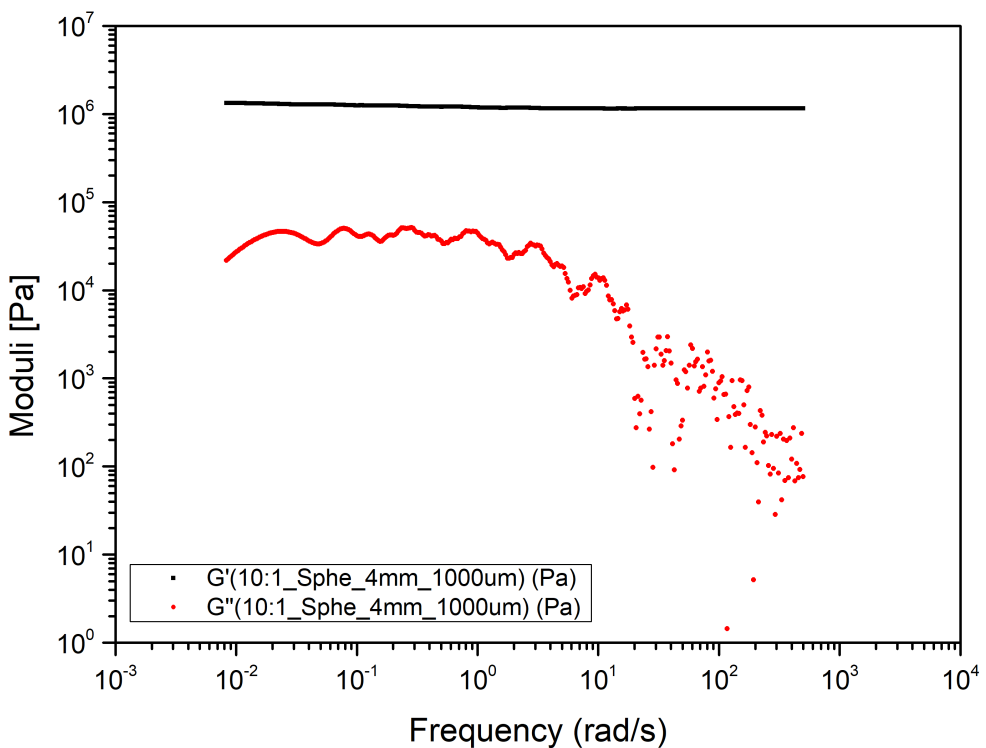


Figure B.70: the 10:1 PDMS sample's viscoelastic moduli derived by means of i-Rheo indentation using spherical indenter with 4mm in diameter and applying 1mm depth

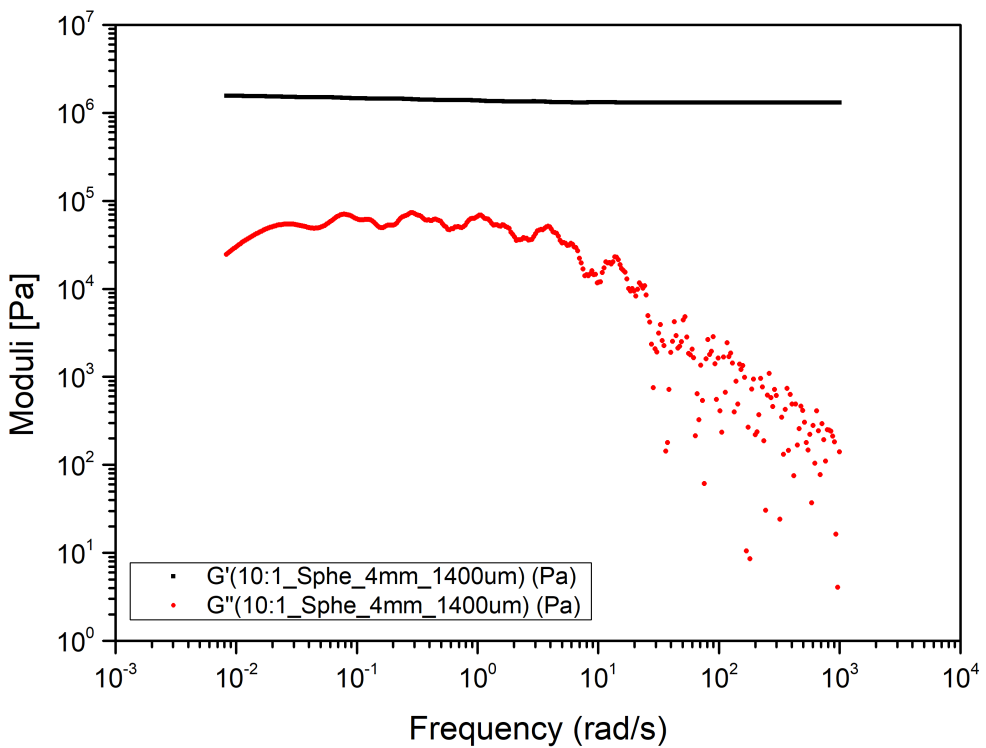


Figure B.71: the 10:1 PDMS sample's viscoelastic moduli derived by means of i-Rheo indentation using spherical indenter with 4mm in diameter and applying 1.4mm depth

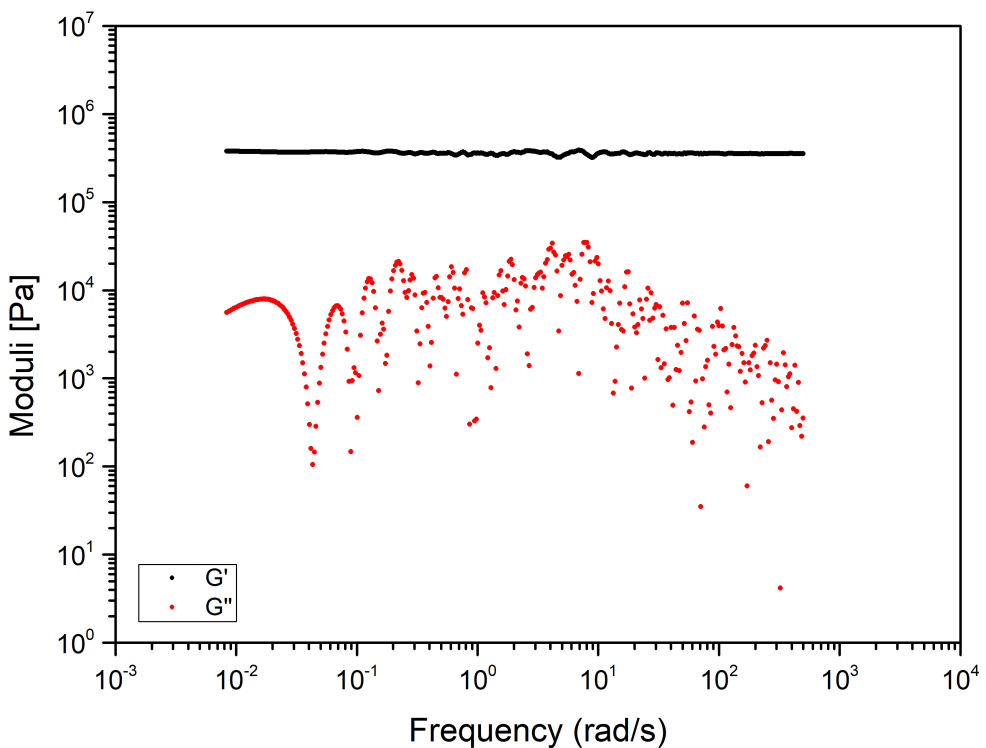


Figure B.72: the 10:1 PDMS sample's viscoelastic moduli derived by means of i-Rheo indentation using spherical indenter with 8mm in diameter and applying 0.1mm depth

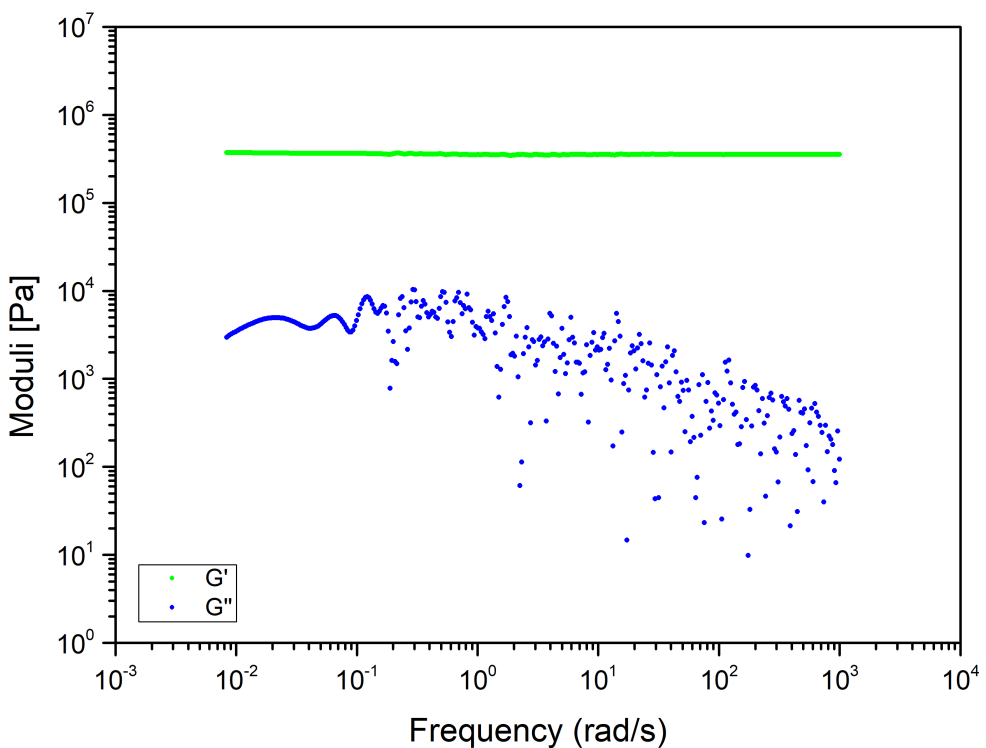


Figure B.73: the 10:1 PDMS sample's viscoelastic moduli derived by means of i-Rheo indentation using spherical indenter with 8mm in diameter and applying 0.2mm depth

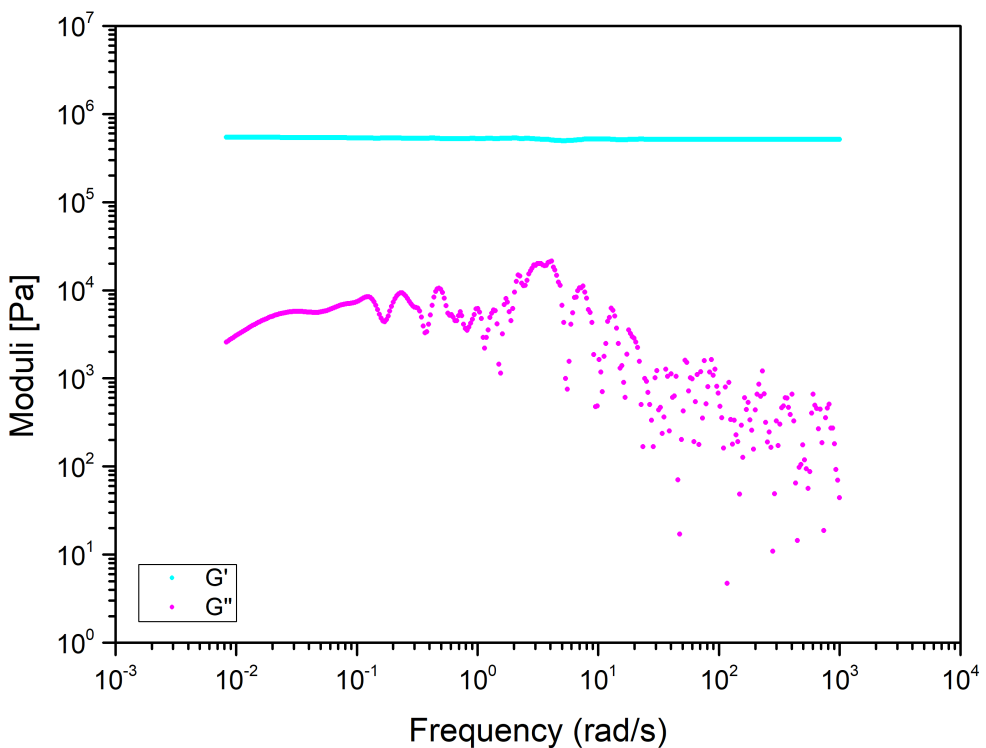


Figure B.74: the 10:1 PDMS sample's viscoelastic moduli derived by means of i-Rheo indentation using spherical indenter with 8mm in diameter and applying 0.3mm depth

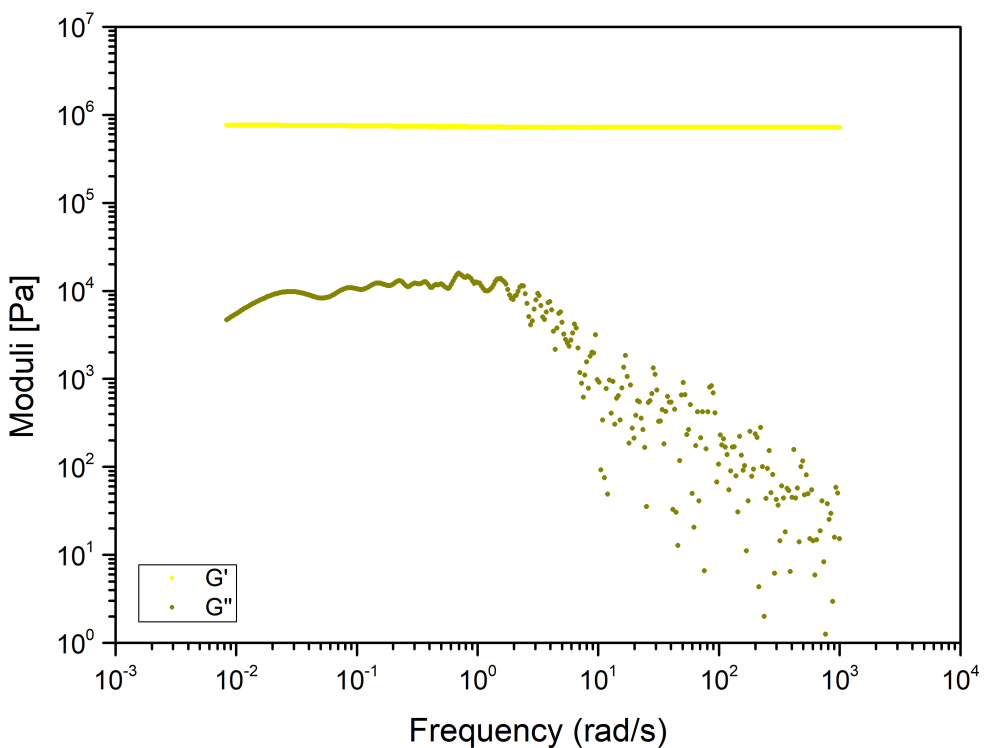


Figure B.75: the 10:1 PDMS sample's viscoelastic moduli derived by means of i-Rheo indentation using spherical indenter with 8mm in diameter and applying 0.4mm depth

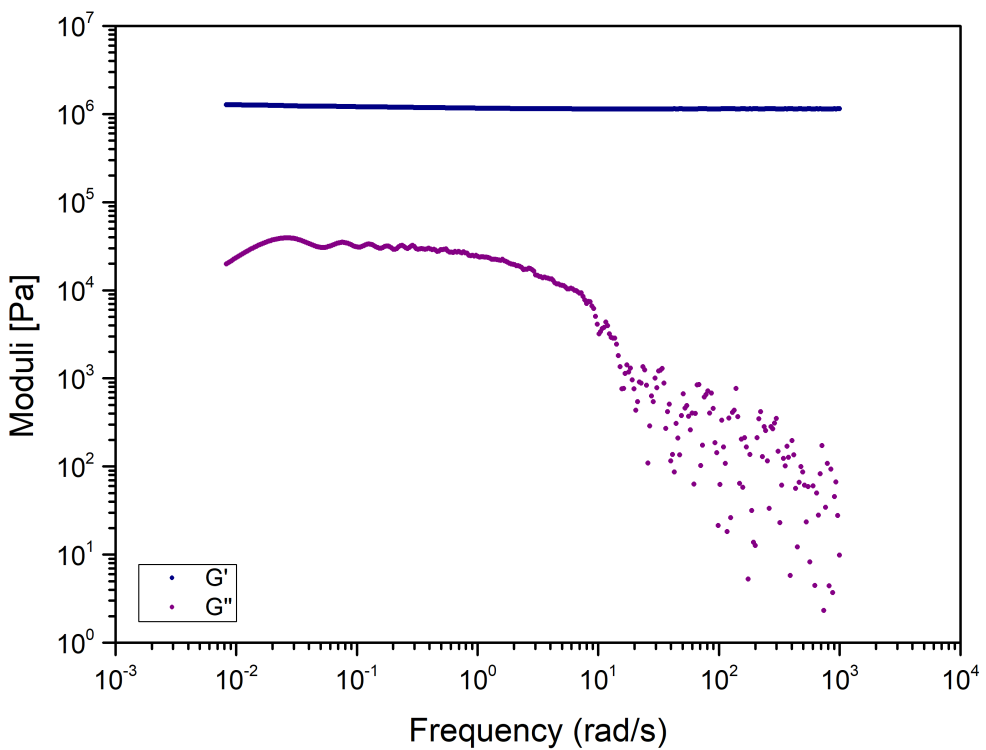


Figure B.76: the 10:1 PDMS sample's viscoelastic moduli derived by means of i-Rheo indentation using spherical indenter with 8mm in diameter and applying 0.7mm depth

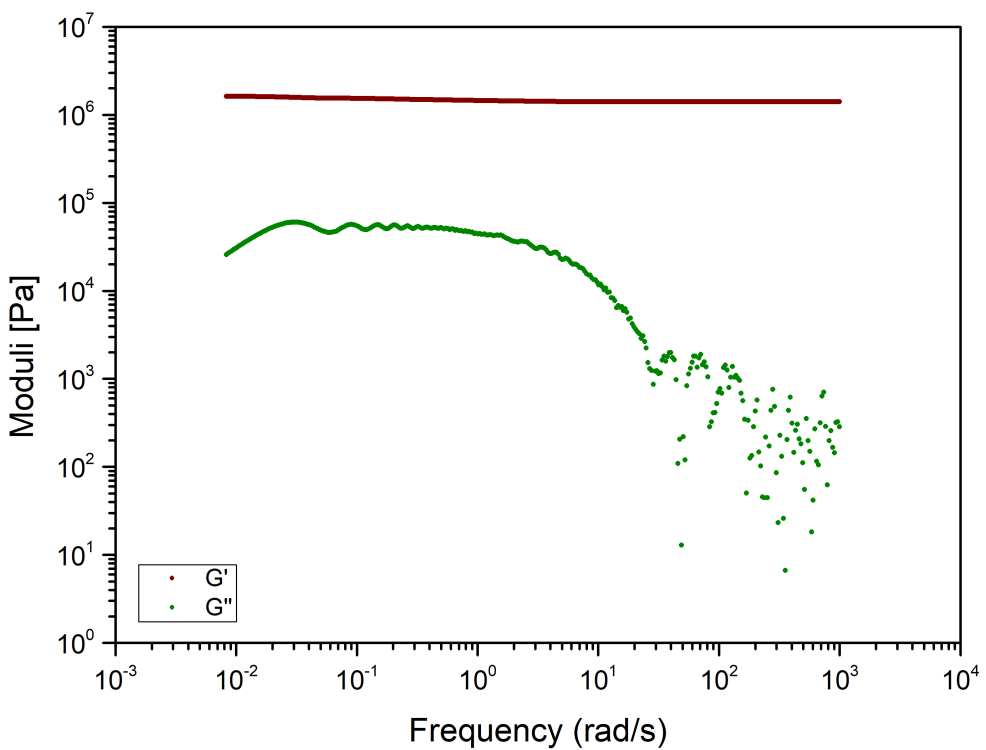


Figure B.77: the 10:1 PDMS sample's viscoelastic moduli derived by means of i-Rheo indentation using spherical indenter with 8mm in diameter and applying 1mm depth

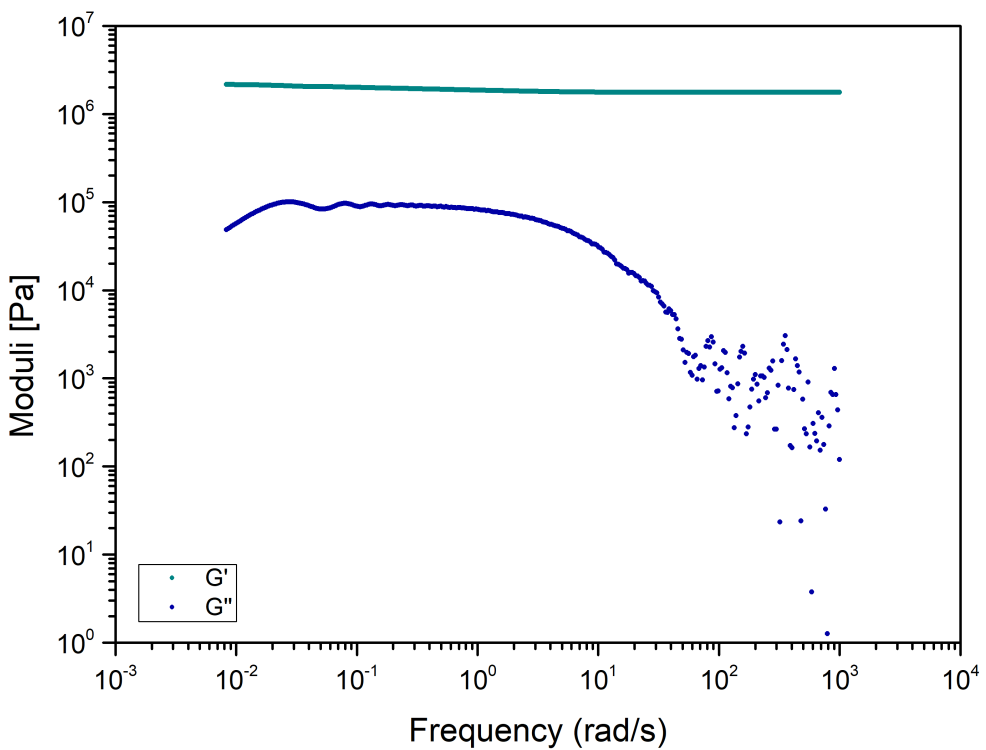


Figure B.78: the 10:1 PDMS sample's viscoelastic moduli derived by means of i-Rheo indentation using spherical indenter with 8mm in diameter and applying 1.4mm depth

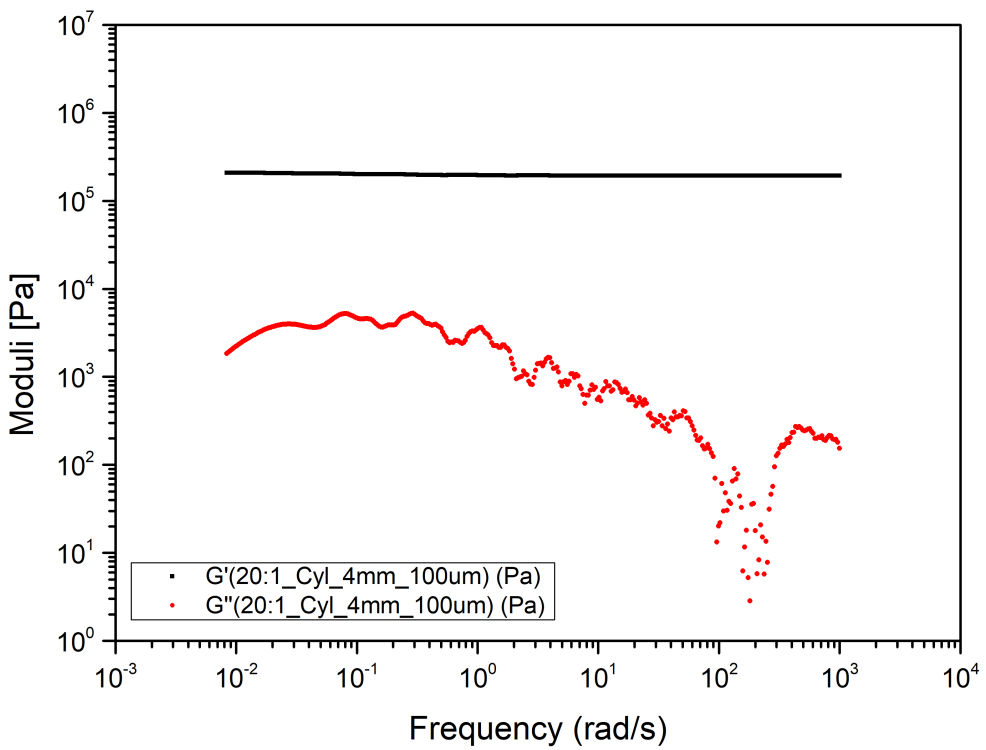


Figure B.79: the 20:1 PDMS sample's viscoelastic moduli derived by means of i-Rheo indentation using cylindrical indenter with 4mm in diameter and applying 0.1mm depth

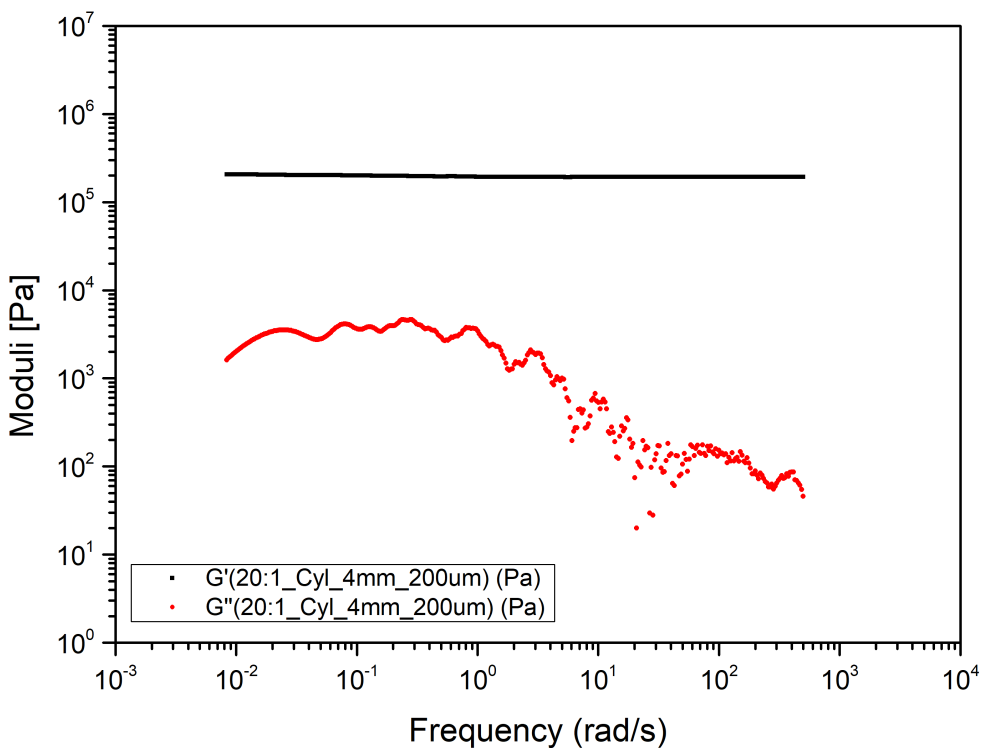


Figure B.80: the 20:1 PDMS sample's viscoelastic moduli derived by means of i-Rheo indentation using cylindrical indenter with 4mm in diameter and applying 0.2mm depth

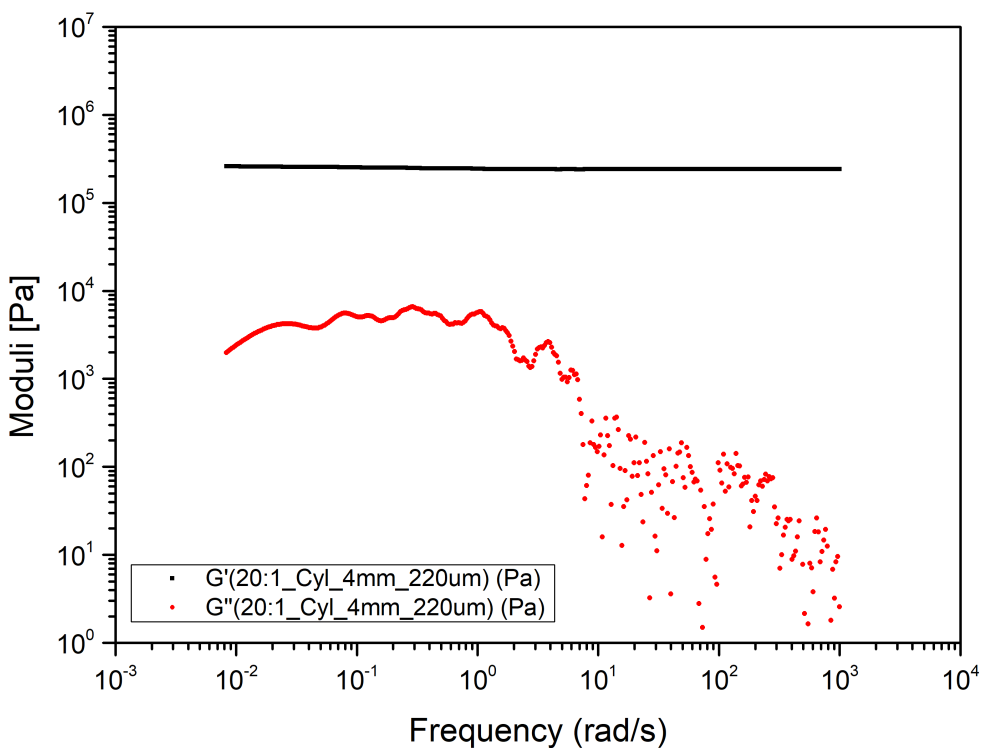


Figure B.81: the 20:1 PDMS sample's viscoelastic moduli derived by means of i-Rheo indentation using cylindrical indenter with 4mm in diameter and applying 0.22mm depth

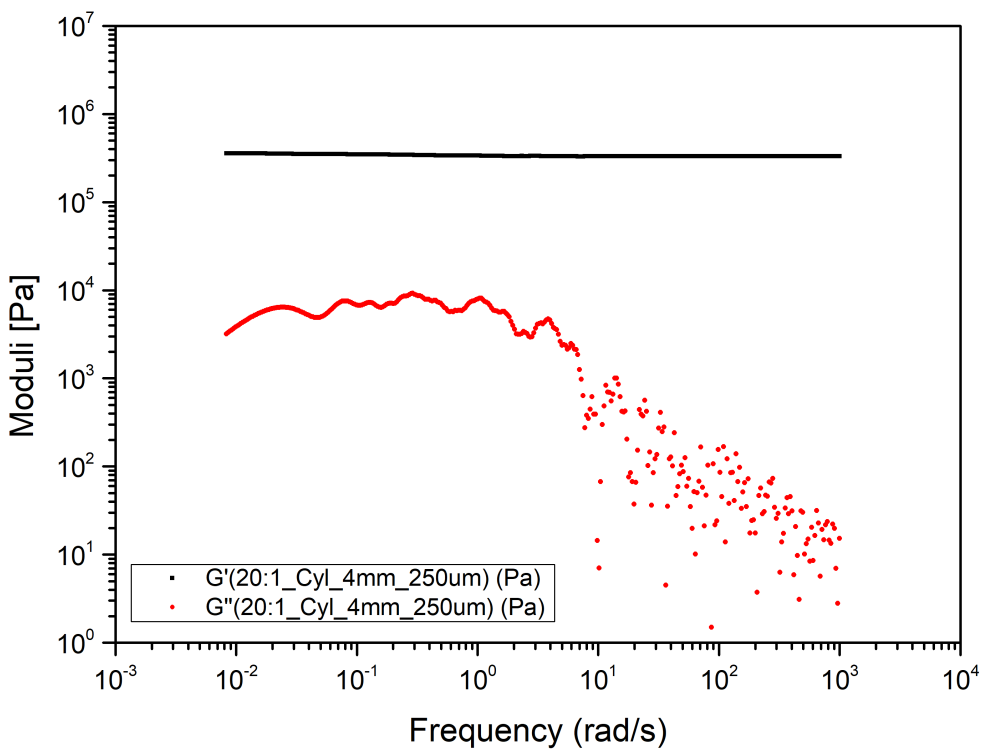


Figure B.82: the 20:1 PDMS sample's viscoelastic moduli derived by means of i-Rheo indentation using cylindrical indenter with 4mm in diameter and applying 0.25mm depth

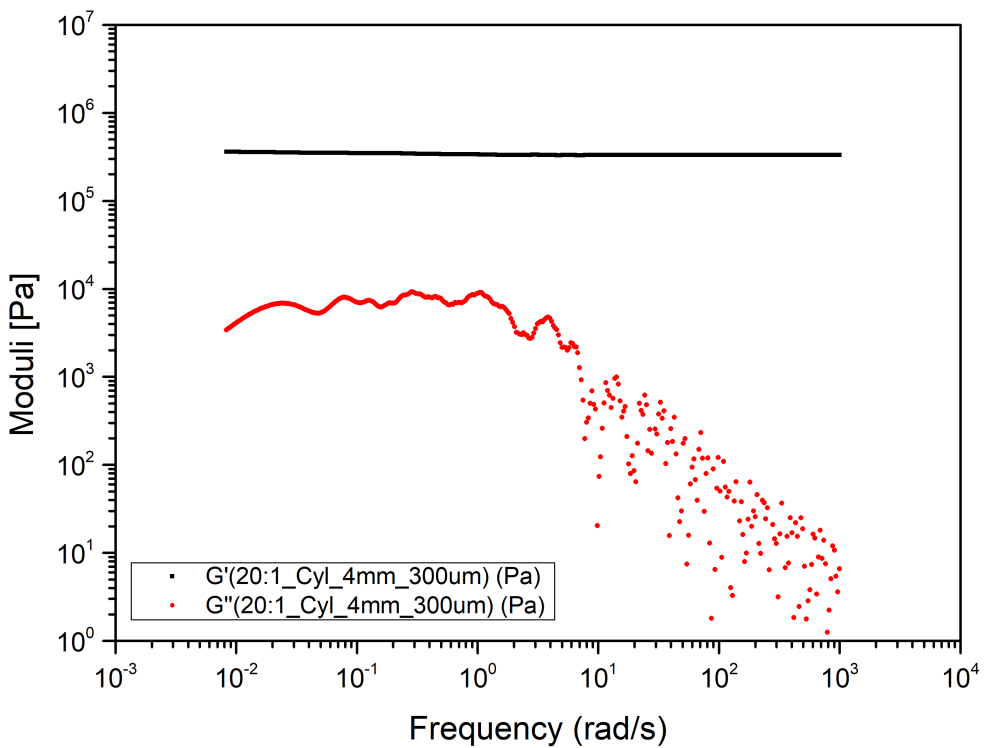


Figure B.83: the 20:1 PDMS sample's viscoelastic moduli derived by means of i-Rheo indentation using cylindrical indenter with 4mm in diameter and applying 0.3mm depth

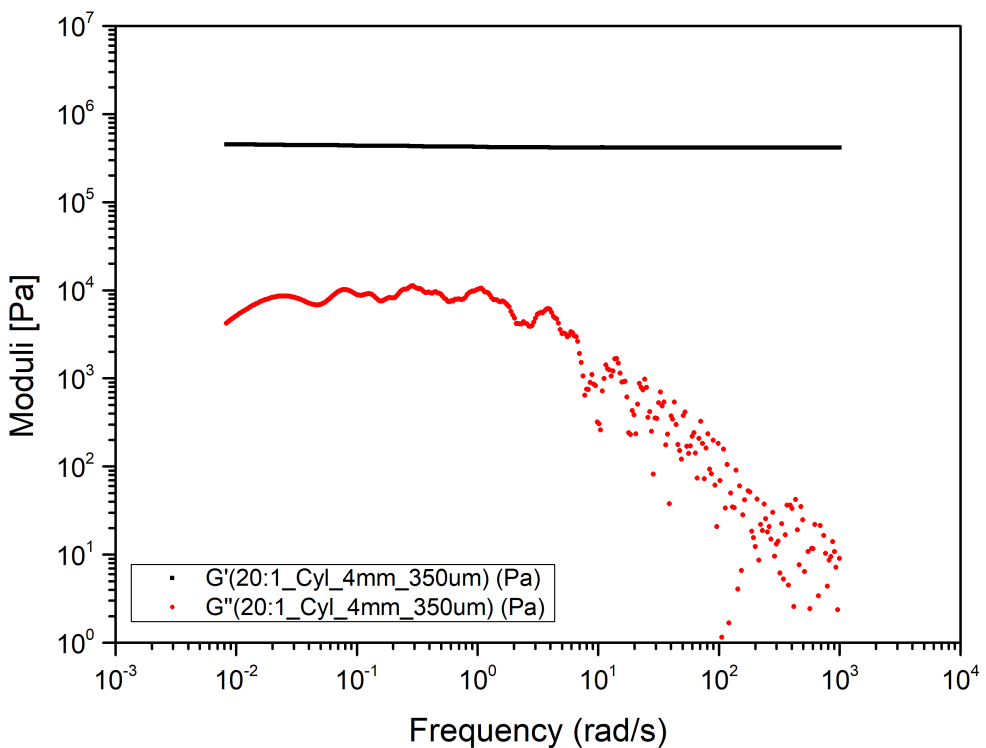


Figure B.84: the 20:1 PDMS sample's viscoelastic moduli derived by means of i-Rheo indentation using cylindrical indenter with 4mm in diameter and applying 0.35mm depth

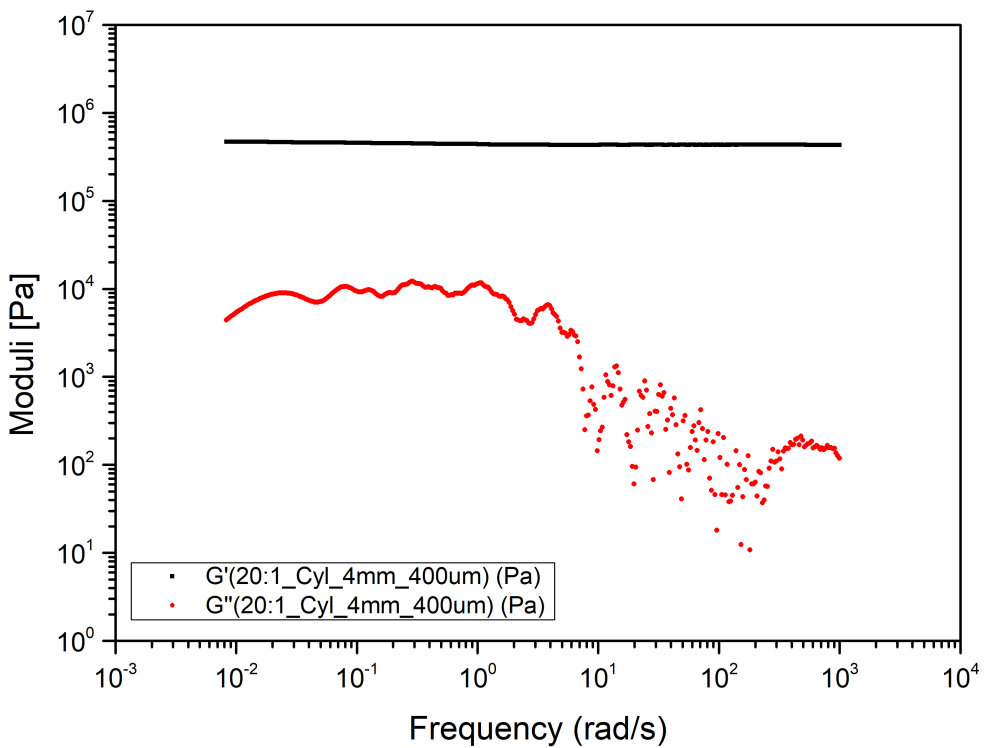


Figure B.85: the 20:1 PDMS sample's viscoelastic moduli derived by means of i-Rheo indentation using cylindrical indenter with 4mm in diameter and applying 0.4mm depth

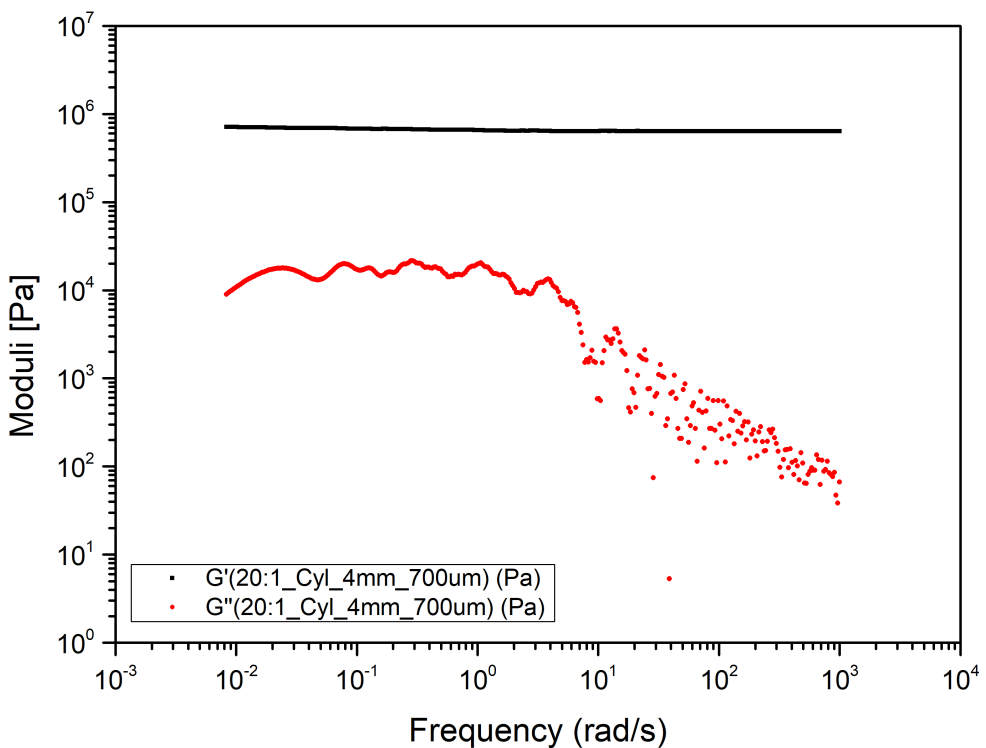


Figure B.86: the 20:1 PDMS sample's viscoelastic moduli derived by means of i-Rheo indentation using cylindrical indenter with 4mm in diameter and applying 0.7mm depth

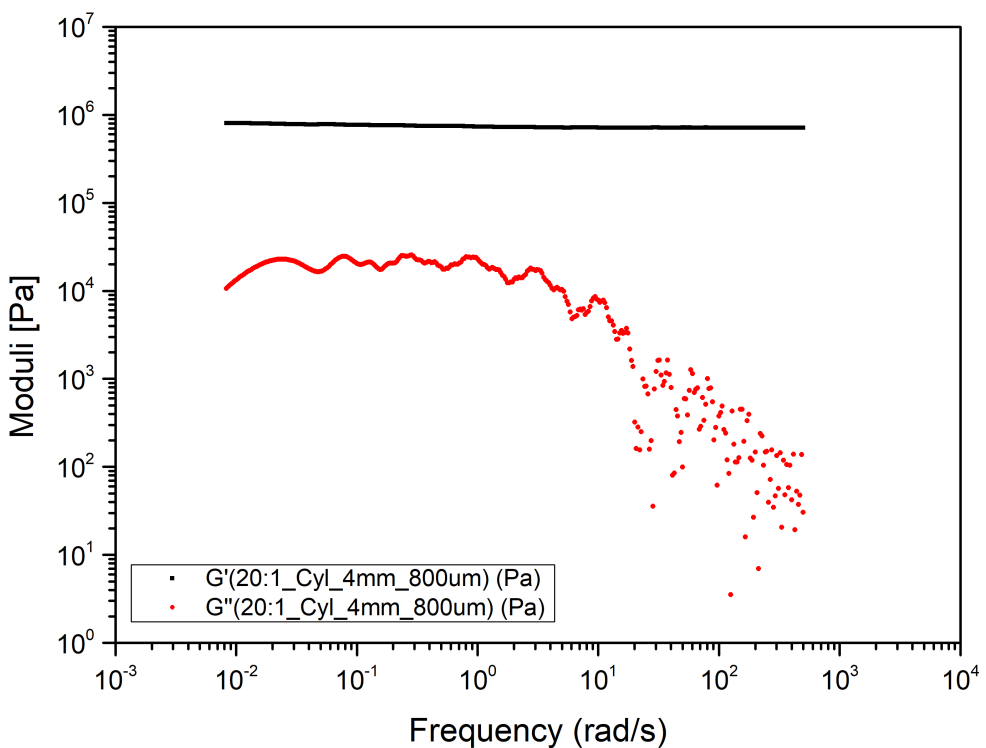


Figure B.87: the 20:1 PDMS sample's viscoelastic moduli derived by means of i-Rheo indentation using cylindrical indenter with 4mm in diameter and applying 0.8mm depth

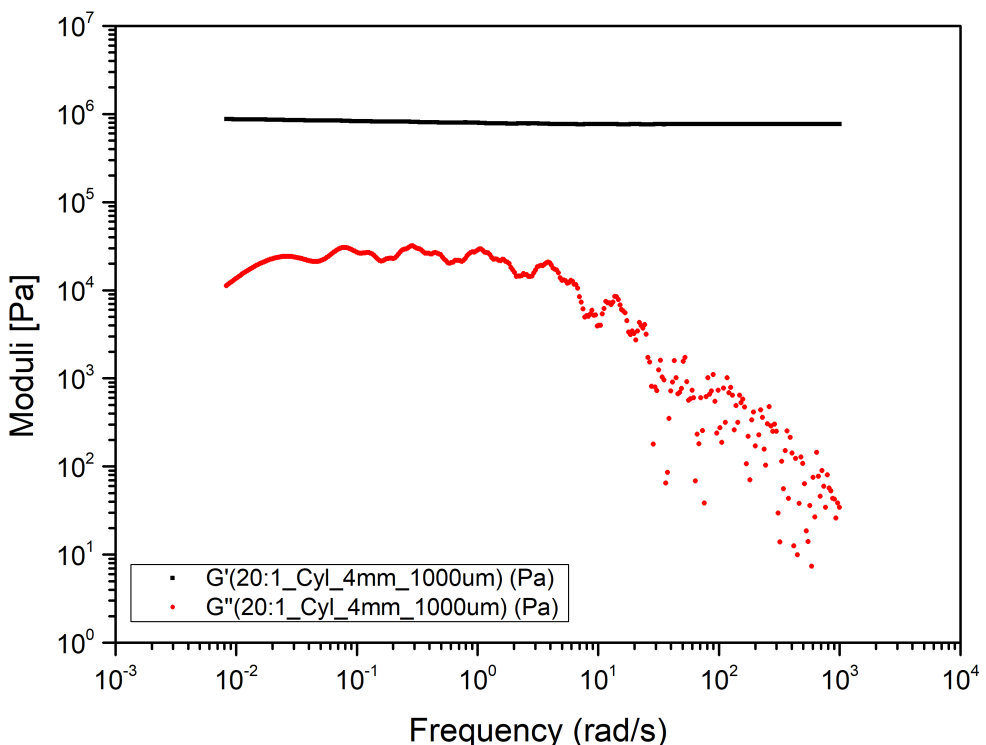


Figure B.88: the 20:1 PDMS sample's viscoelastic moduli derived by means of i-Rheo indentation using cylindrical indenter with 4mm in diameter and applying 1mm depth

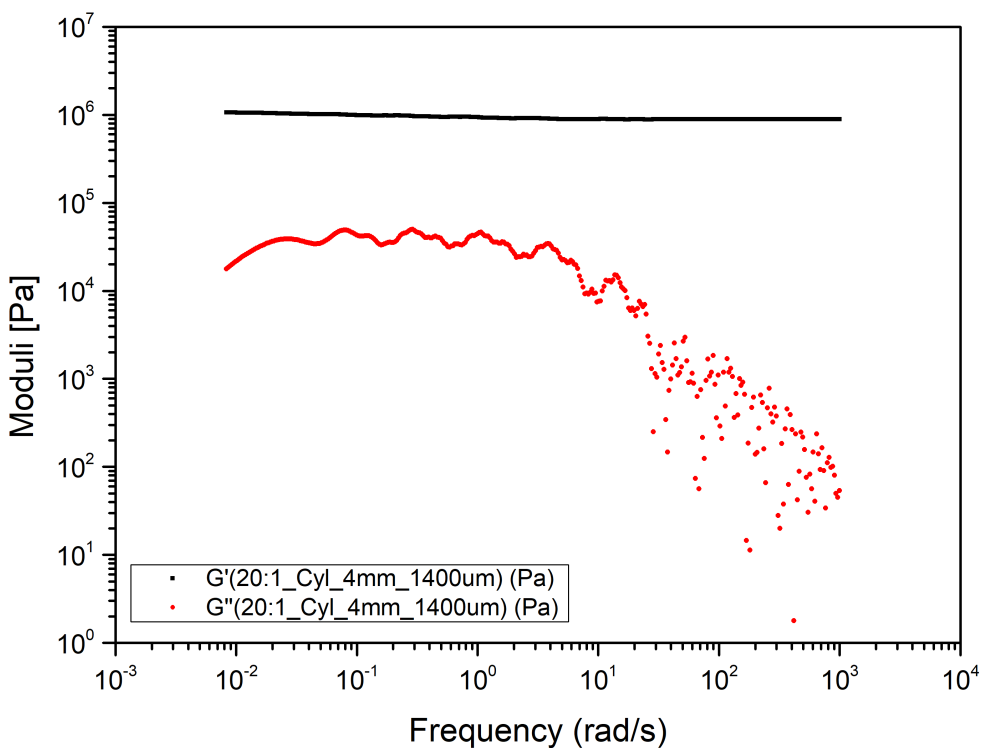


Figure B.89: the 20:1 PDMS sample's viscoelastic moduli derived by means of i-Rheo indentation using cylindrical indenter with 4mm in diameter and applying 1.4mm depth

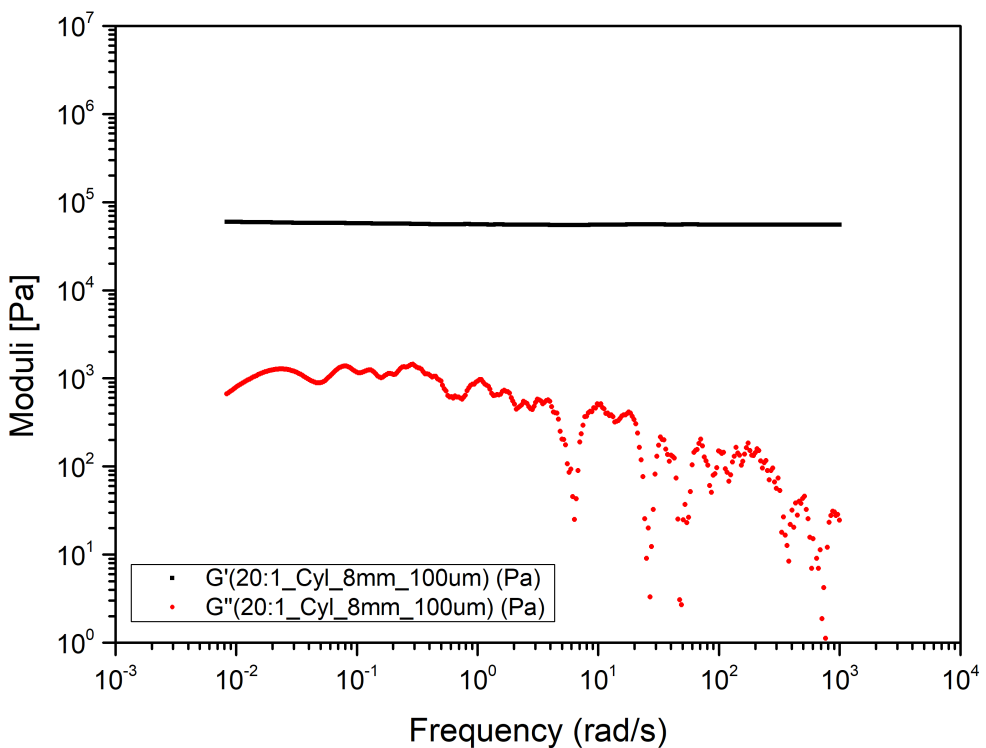


Figure B.90: the 20:1 PDMS sample's viscoelastic moduli derived by means of i-Rheo indentation using cylindrical indenter with 8mm in diameter and applying 0.1mm depth

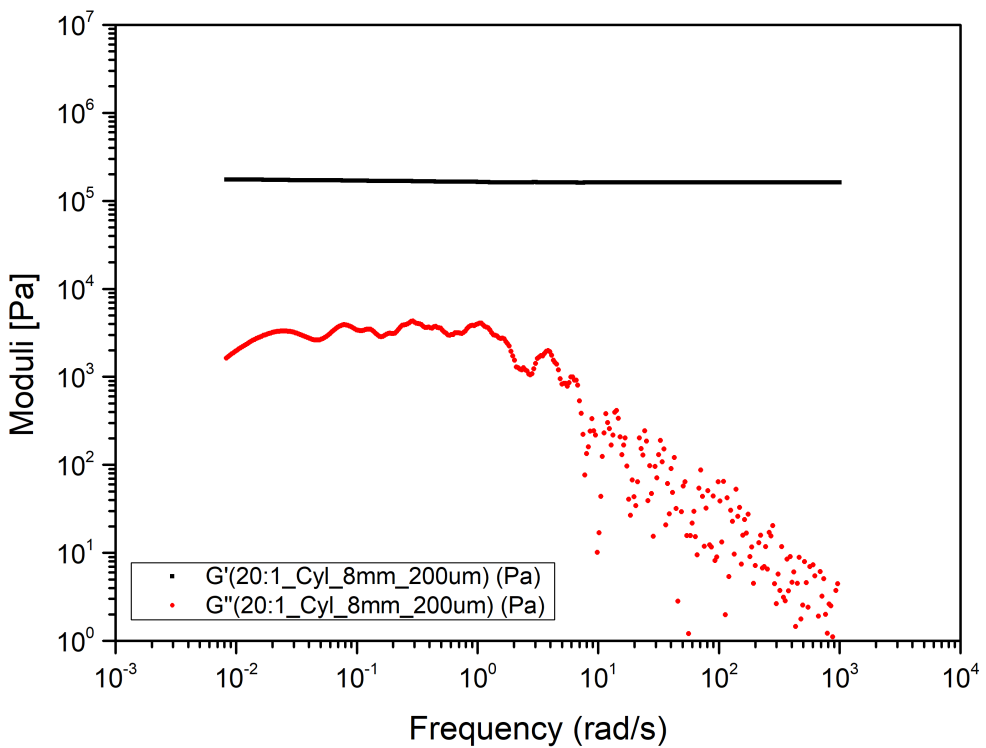


Figure B.91: the 20:1 PDMS sample's viscoelastic moduli derived by means of i-Rheo indentation using cylindrical indenter with 8mm in diameter and applying 0.2mm depth

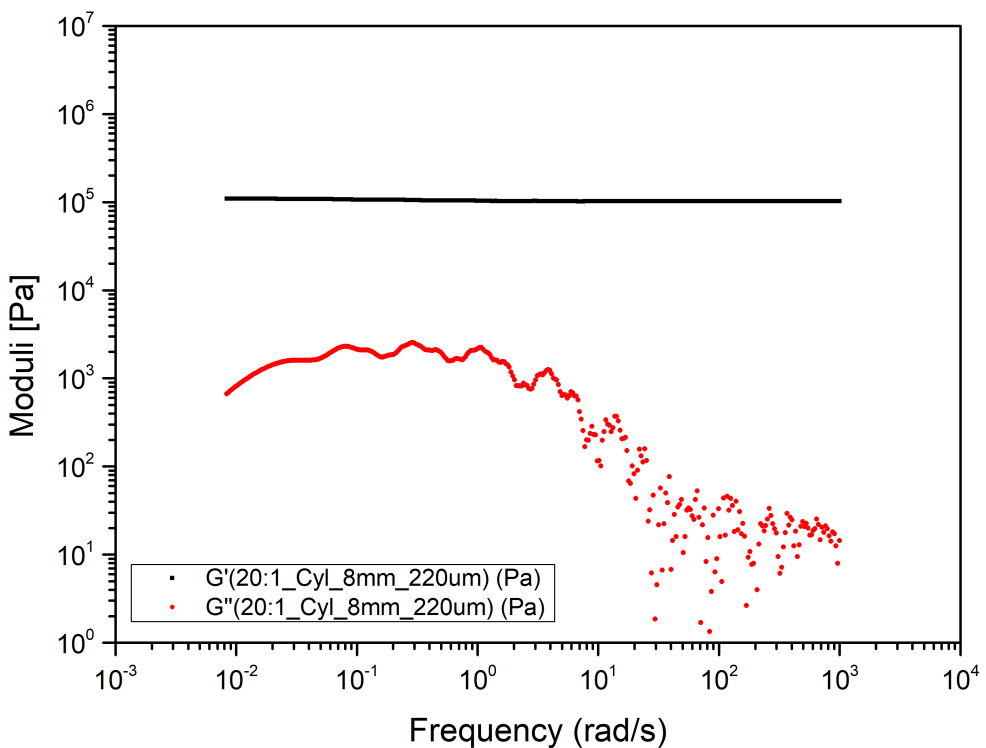


Figure B.92: the 20:1 PDMS sample's viscoelastic moduli derived by means of i-Rheo indentation using cylindrical indenter with 8mm in diameter and applying 0.22mm depth

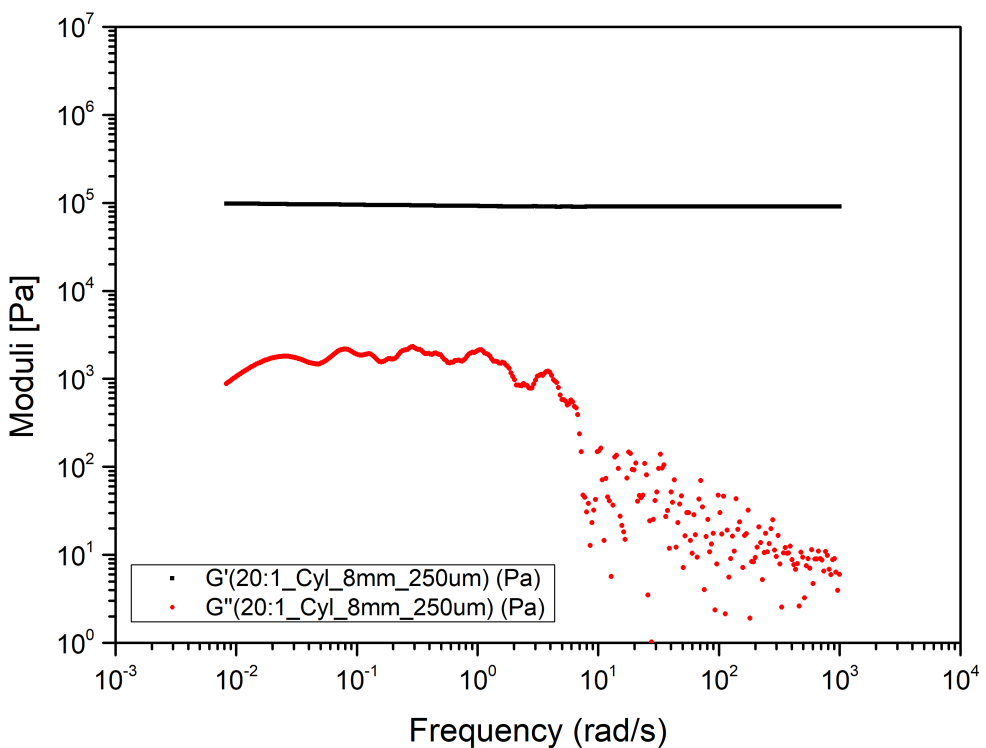


Figure B.93: the 20:1 PDMS sample's viscoelastic moduli derived by means of i-Rheo indentation using cylindrical indenter with 8mm in diameter and applying 0.25mm depth

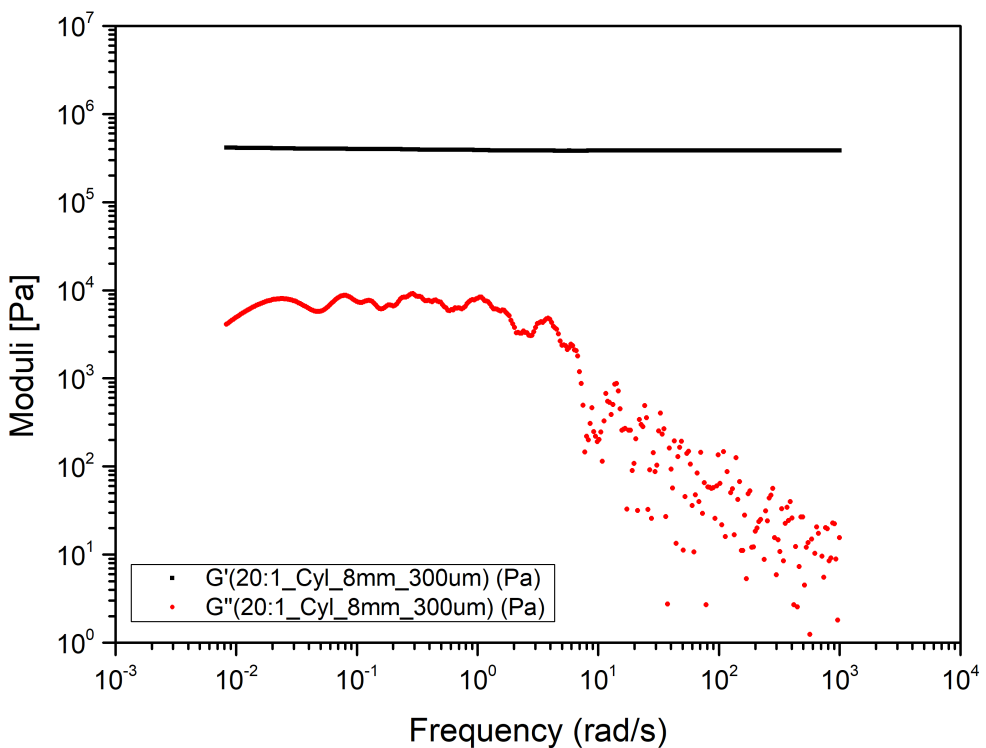


Figure B.94: the 20:1 PDMS sample's viscoelastic moduli derived by means of i-Rheo indentation using cylindrical indenter with 8mm in diameter and applying 0.3mm depth

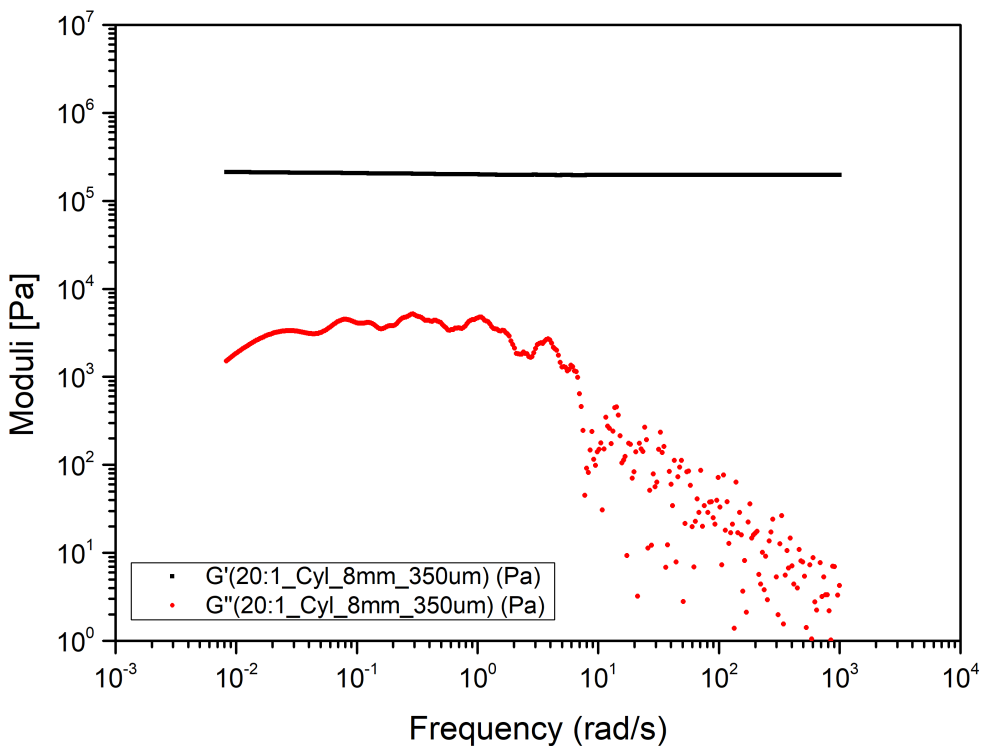


Figure B.95: the 20:1 PDMS sample's viscoelastic moduli derived by means of i-Rheo indentation using cylindrical indenter with 8mm in diameter and applying 0.35mm depth

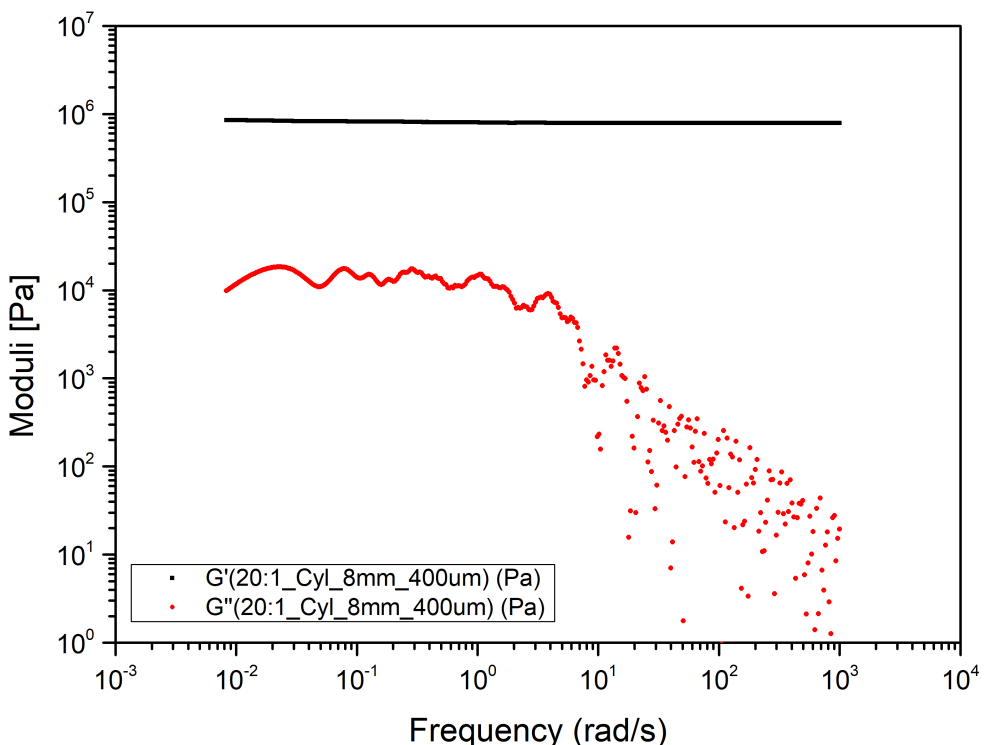


Figure B.96: the 20:1 PDMS sample's viscoelastic moduli derived by means of i-Rheo indentation using cylindrical indenter with 8mm in diameter and applying 0.4mm depth

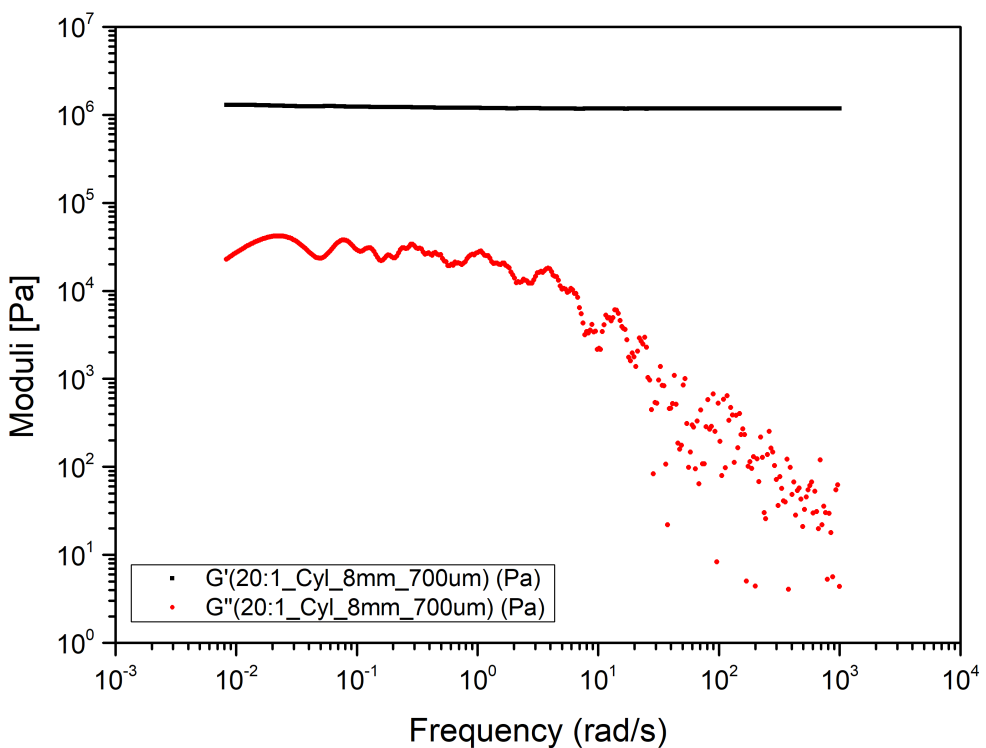


Figure B.97: the 20:1 PDMS sample's viscoelastic moduli derived by means of i-Rheo indentation using cylindrical indenter with 8mm in diameter and applying 0.7mm depth

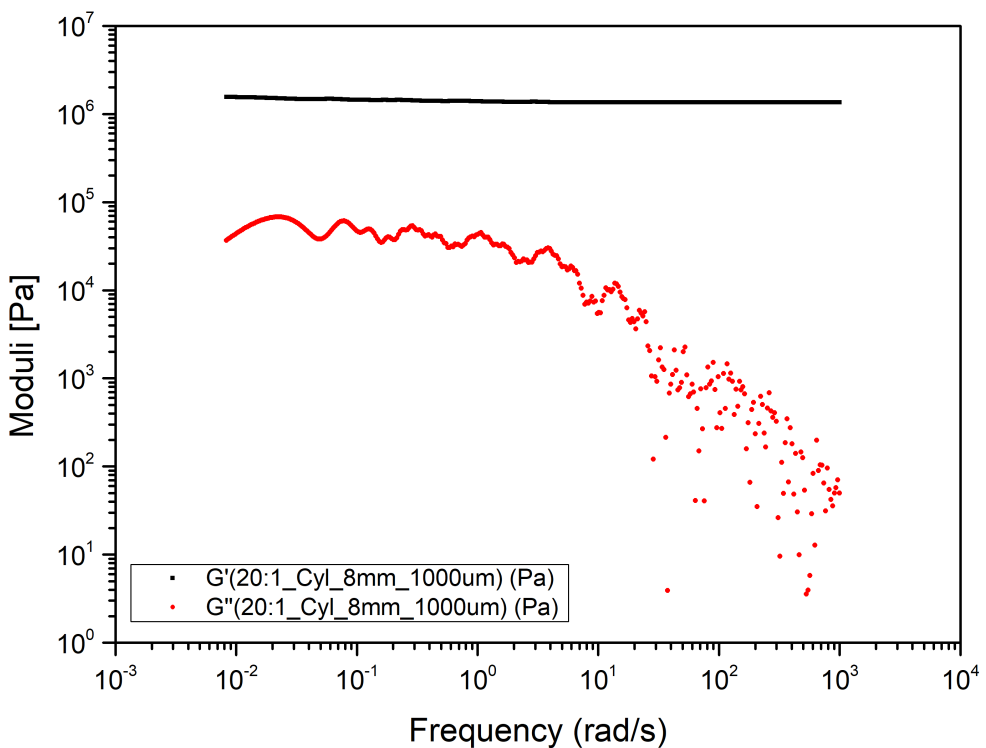


Figure B.98: the 20:1 PDMS sample's viscoelastic moduli derived by means of i-Rheo indentation using cylindrical indenter with 8mm in diameter and applying 1mm depth

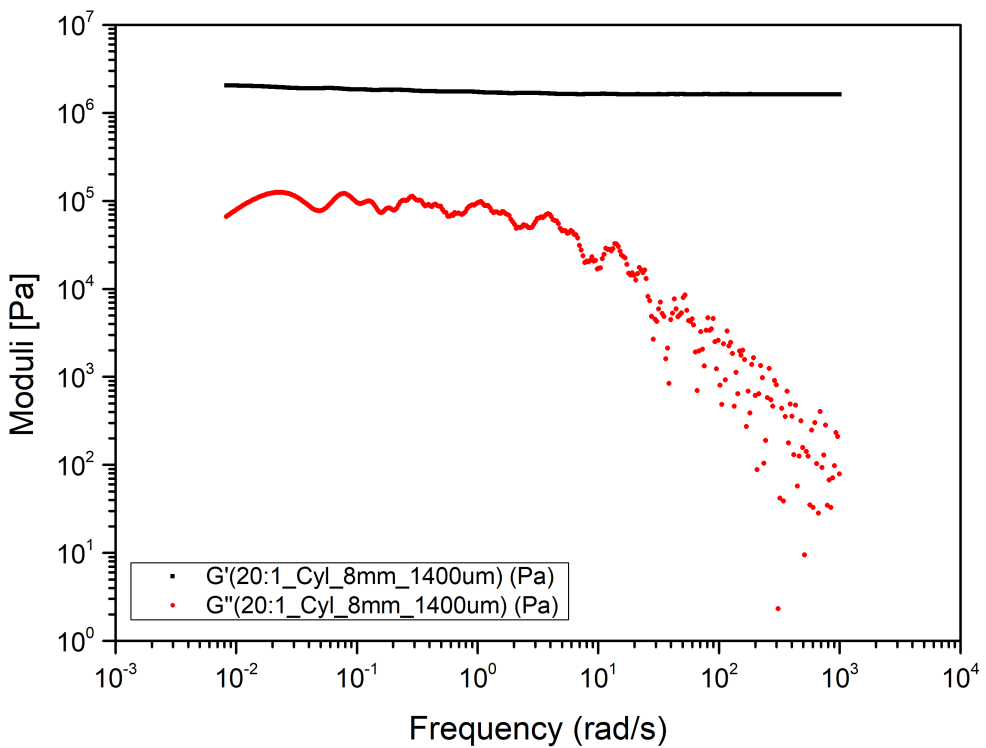


Figure B.99: the 20:1 PDMS sample's viscoelastic moduli derived by means of i-Rheo indentation using cylindrical indenter with 8mm in diameter and applying 1.4mm depth

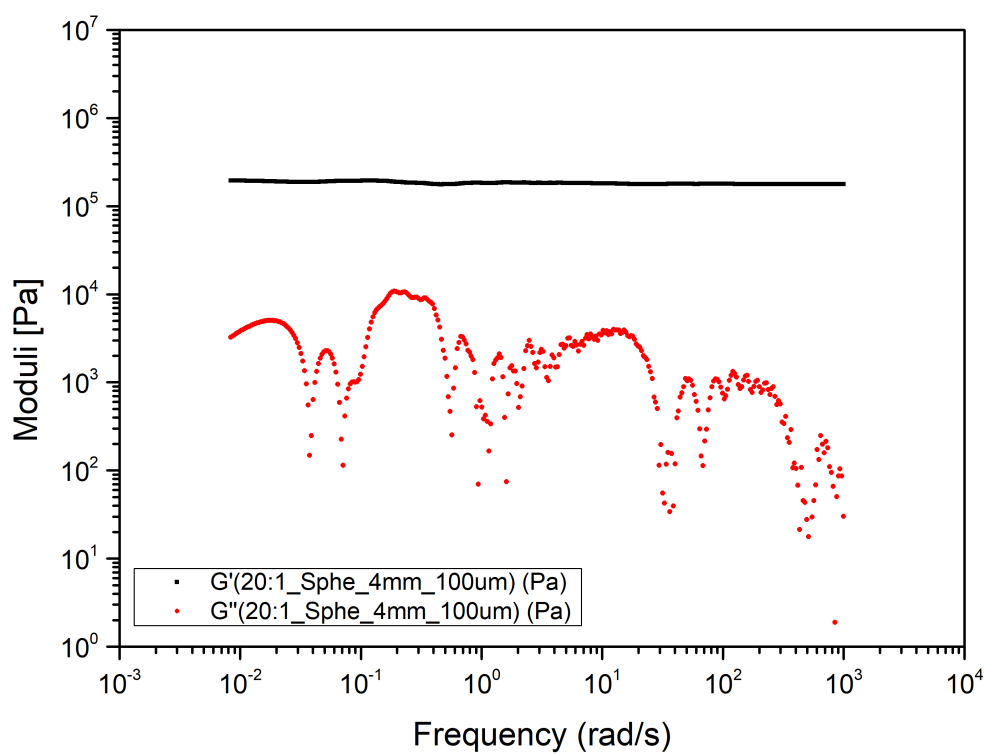


Figure B.100: the 20:1 PDMS sample's viscoelastic moduli derived by means of i-Rheo indentation using spherical indenter with 4mm in diameter and applying 0.1mm depth

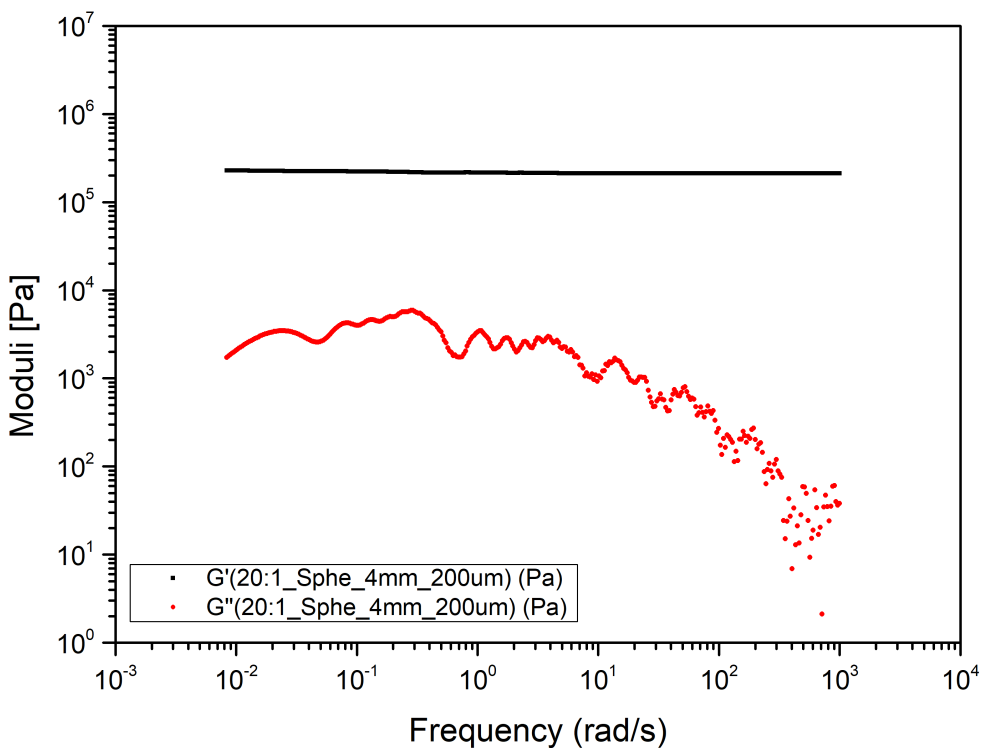


Figure B.101: the 20:1 PDMS sample's viscoelastic moduli derived by means of i-Rheo indentation using spherical indenter with 4mm in diameter and applying 0.2mm depth

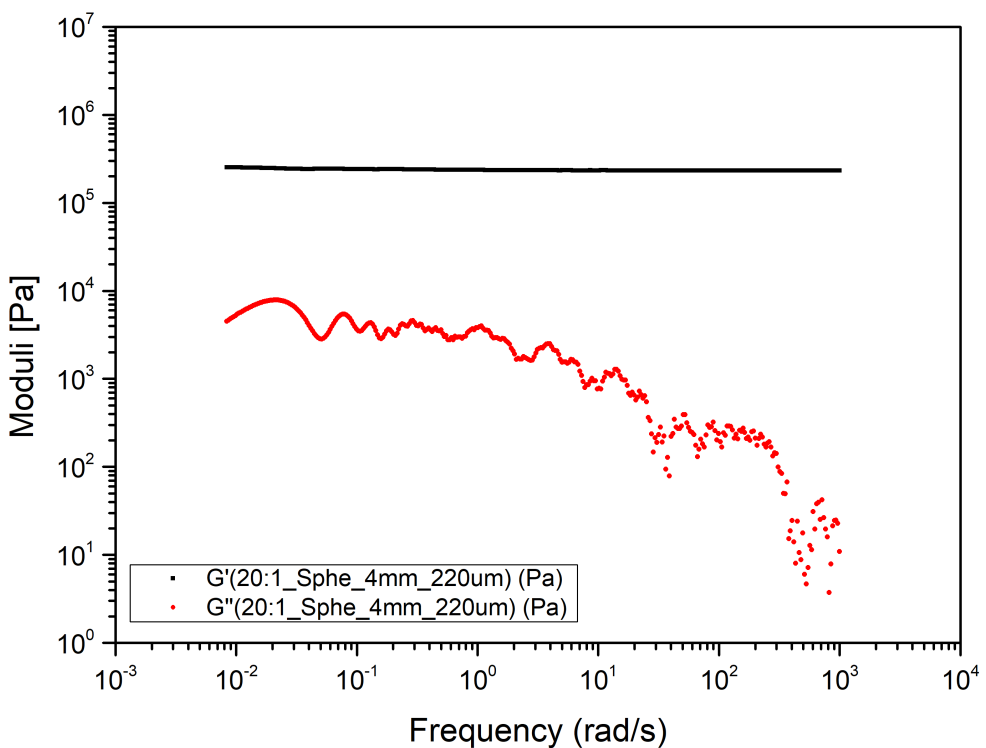


Figure B.102: the 20:1 PDMS sample's viscoelastic moduli derived by means of i-Rheo indentation using spherical indenter with 4mm in diameter and applying 0.22mm depth

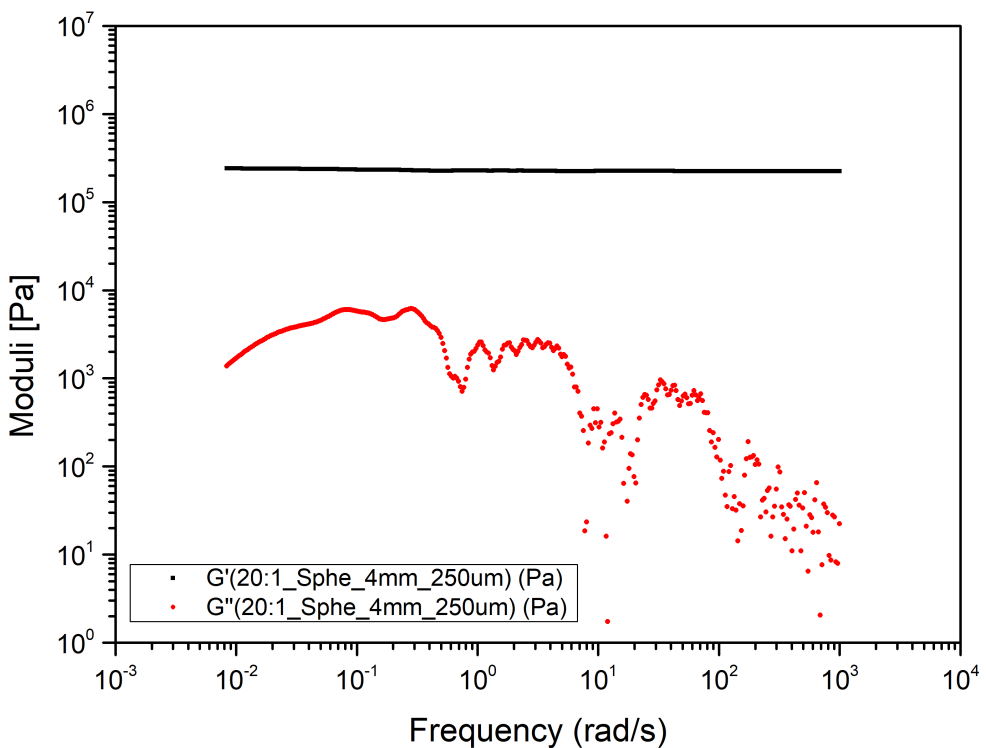


Figure B.103: the 20:1 PDMS sample's viscoelastic moduli derived by means of i-Rheo indentation using spherical indenter with 4mm in diameter and applying 0.25mm depth

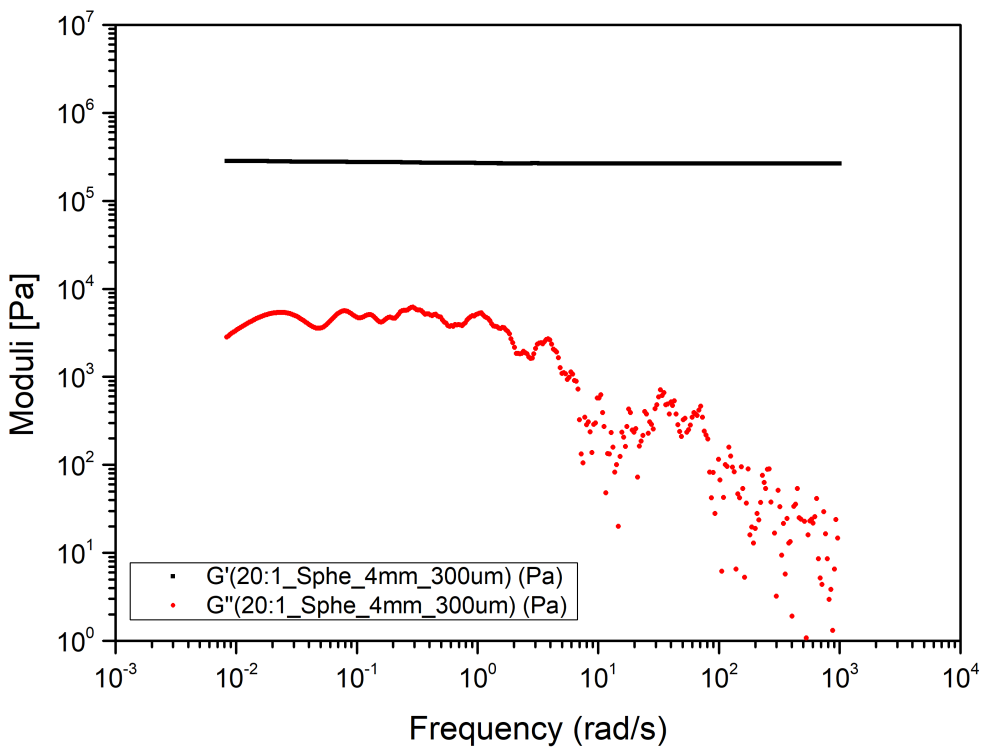


Figure B.104: the 20:1 PDMS sample's viscoelastic moduli derived by means of i-Rheo indentation using spherical indenter with 4mm in diameter and applying 0.3mm depth

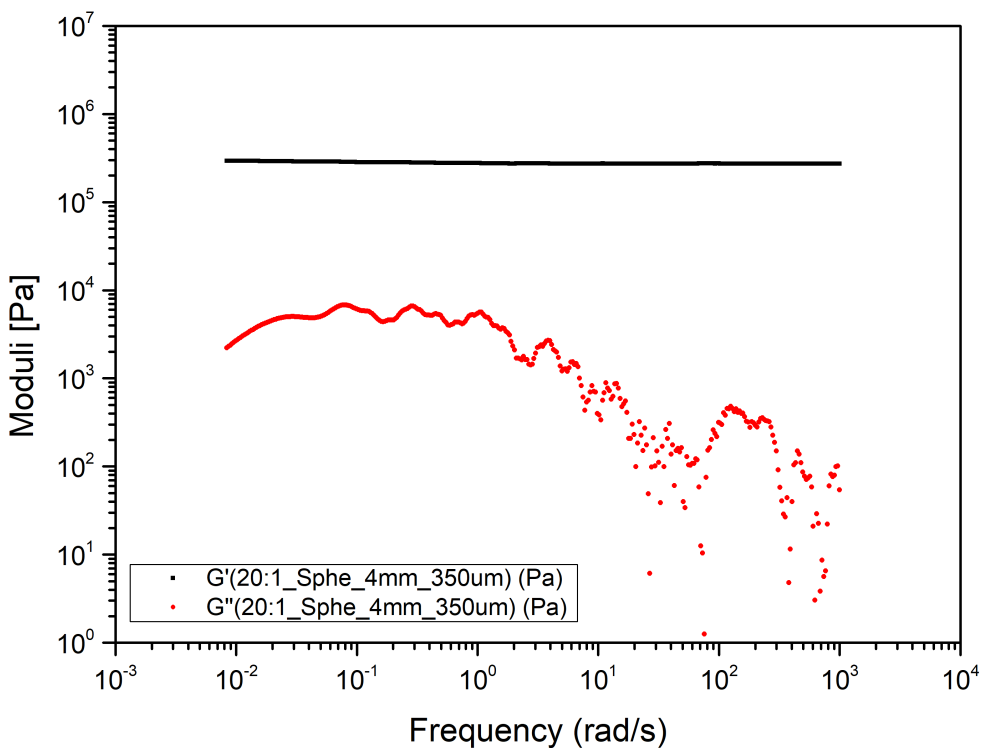


Figure B.105: the 20:1 PDMS sample's viscoelastic moduli derived by means of i-Rheo indentation using spherical indenter with 4mm in diameter and applying 0.35mm depth

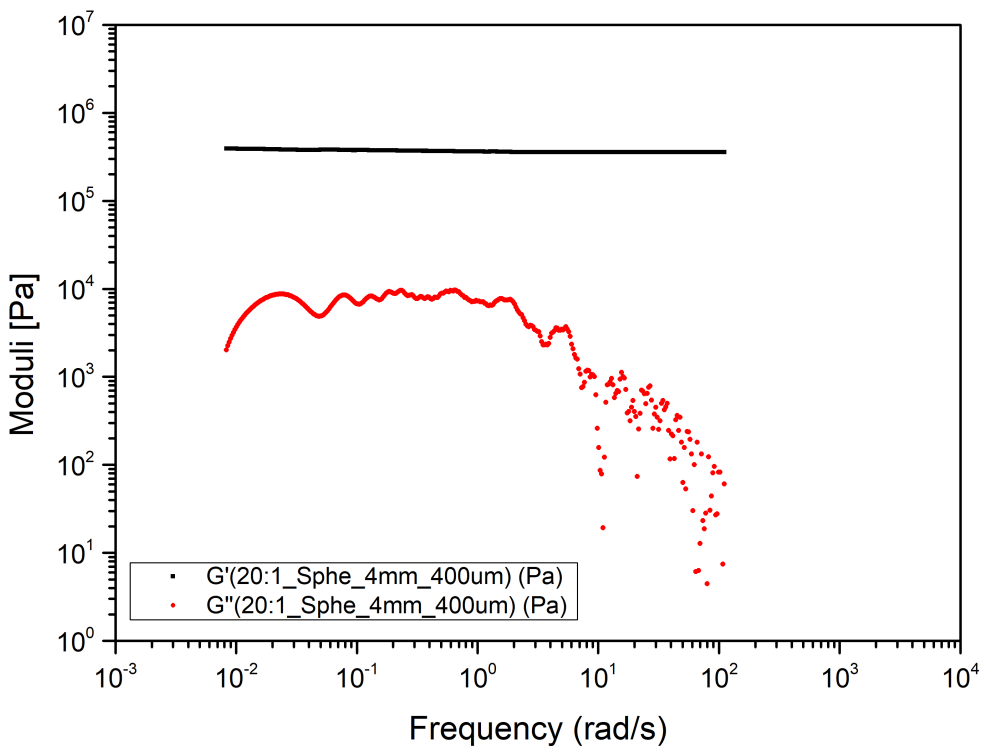


Figure B.106: the 20:1 PDMS sample's viscoelastic moduli derived by means of i-Rheo indentation using spherical indenter with 4mm in diameter and applying 0.4mm depth

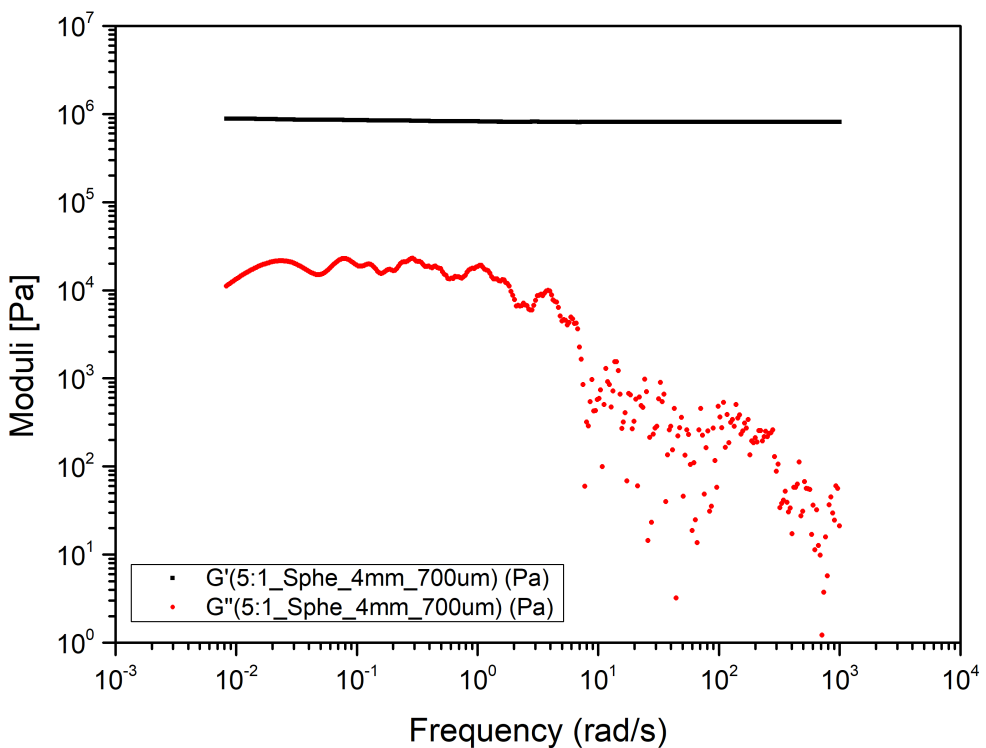


Figure B.107: the 20:1 PDMS sample's viscoelastic moduli derived by means of i-Rheo indentation using spherical indenter with 4mm in diameter and applying 0.7mm depth

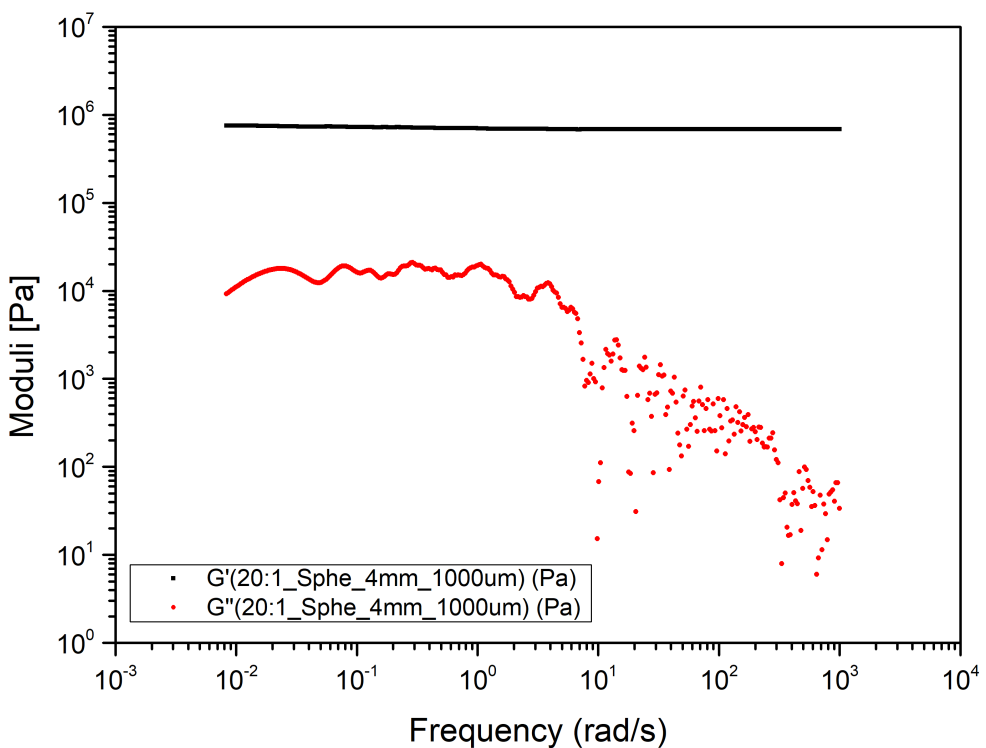


Figure B.108: the 20:1 PDMS sample's viscoelastic moduli derived by means of i-Rheo indentation using spherical indenter with 4mm in diameter and applying 1mm depth

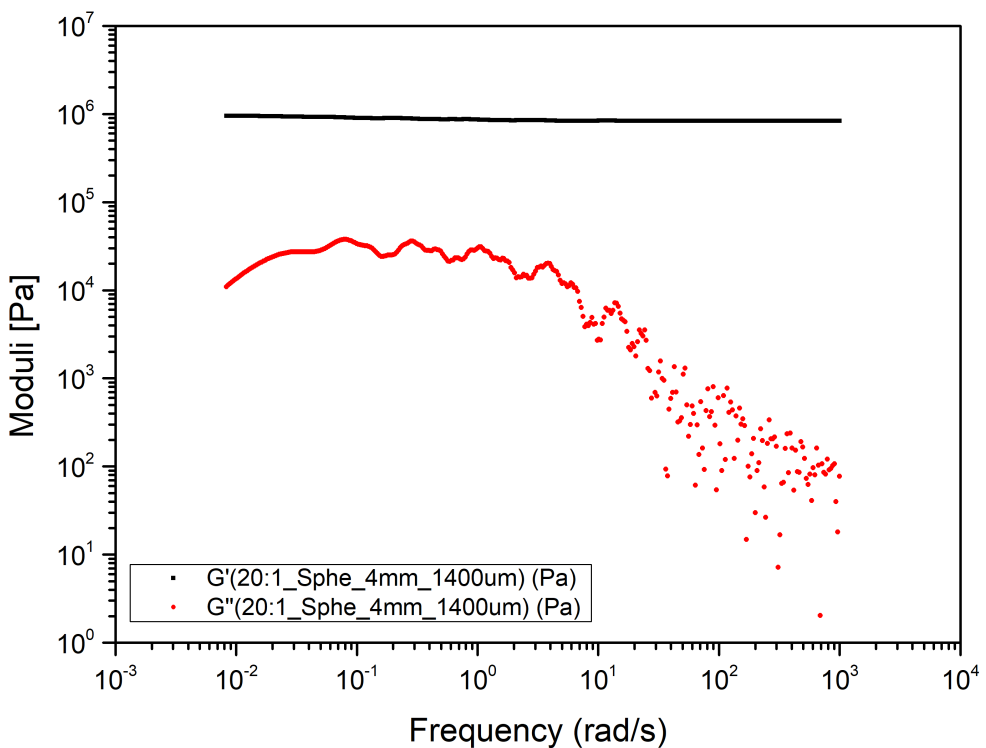


Figure B.109: the 20:1 PDMS sample's viscoelastic moduli derived by means of i-Rheo indentation using spherical indenter with 4mm in diameter and applying 1.4mm depth

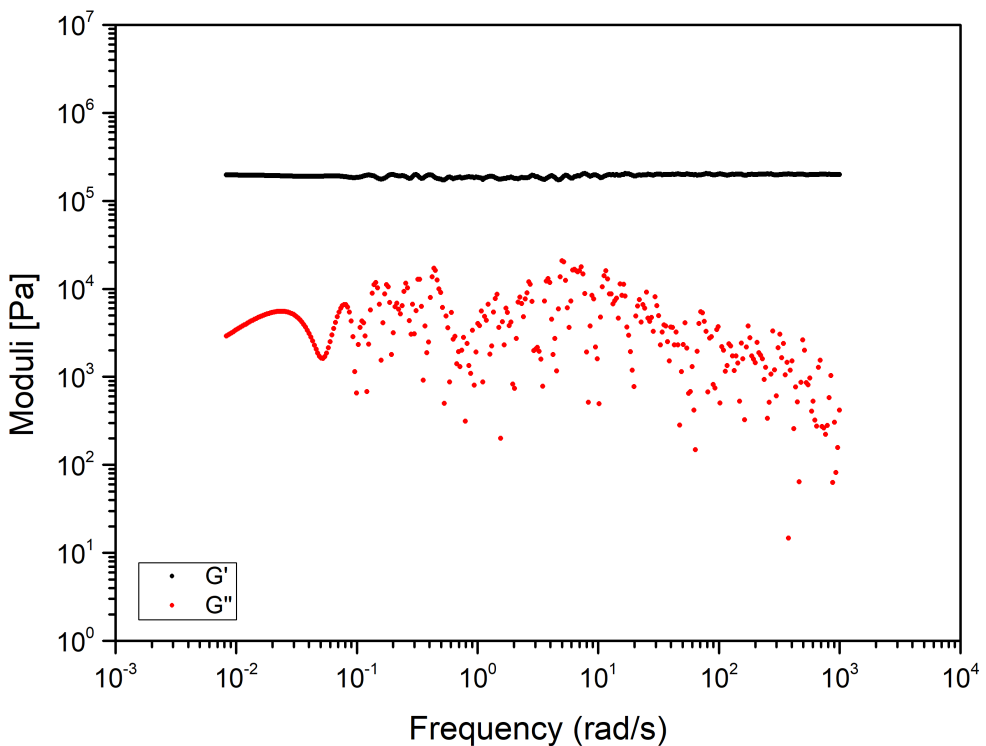


Figure B.110: the 20:1 PDMS sample's viscoelastic moduli derived by means of i-Rheo indentation using spherical indenter with 8mm in diameter and applying 0.1mm depth

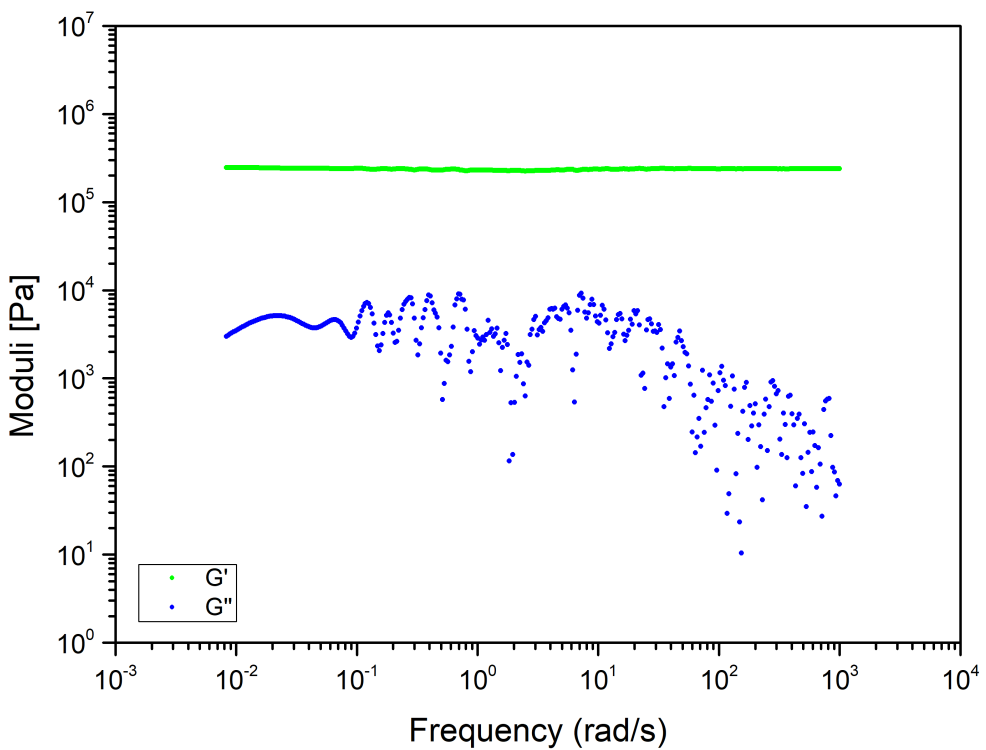


Figure B.111: the 20:1 PDMS sample's viscoelastic moduli derived by means of i-Rheo indentation using spherical indenter with 8mm in diameter and applying 0.2mm depth

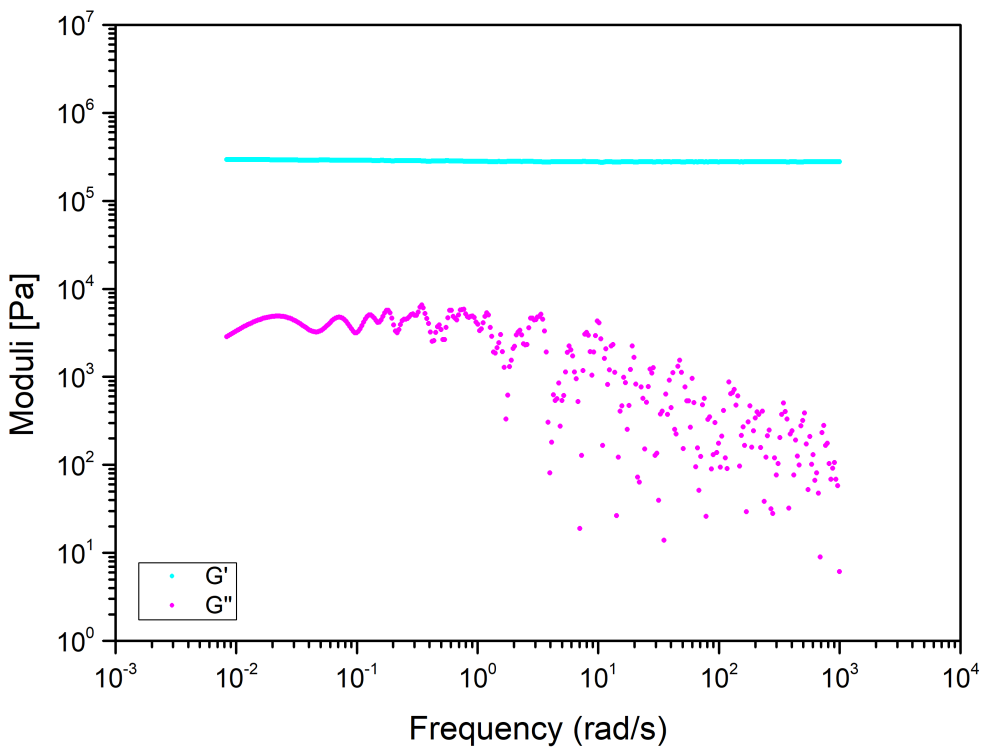


Figure B.112: the 20:1 PDMS sample's viscoelastic moduli derived by means of i-Rheo indentation using spherical indenter with 8mm in diameter and applying 0.3mm depth

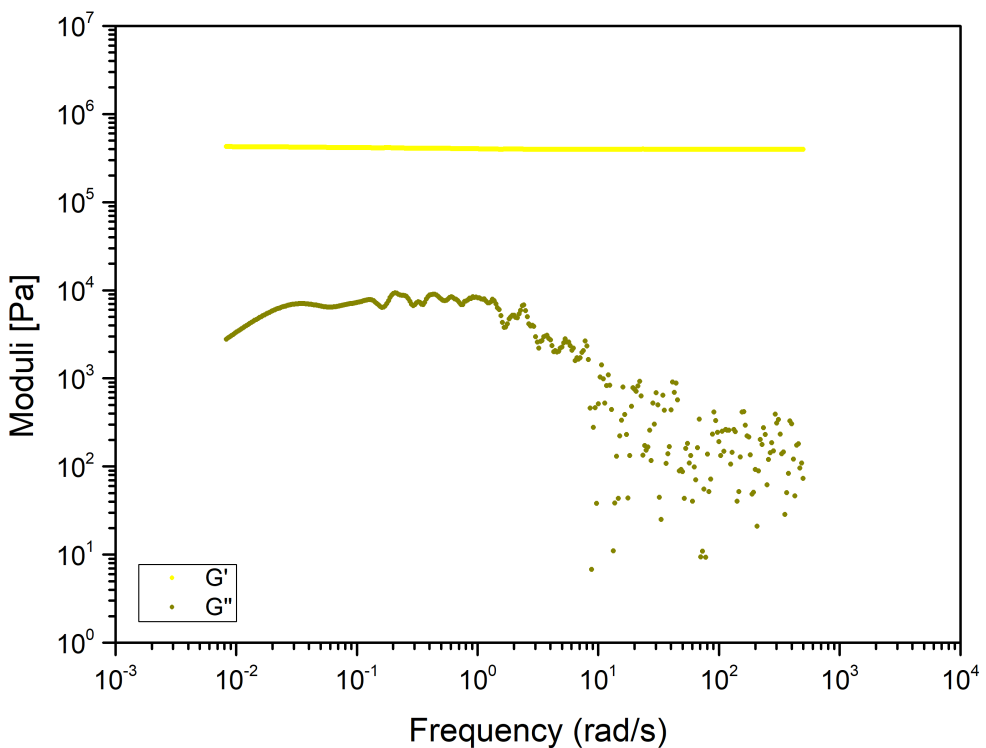


Figure B.113: the 20:1 PDMS sample's viscoelastic moduli derived by means of i-Rheo indentation using spherical indenter with 8mm in diameter and applying 0.4mm depth

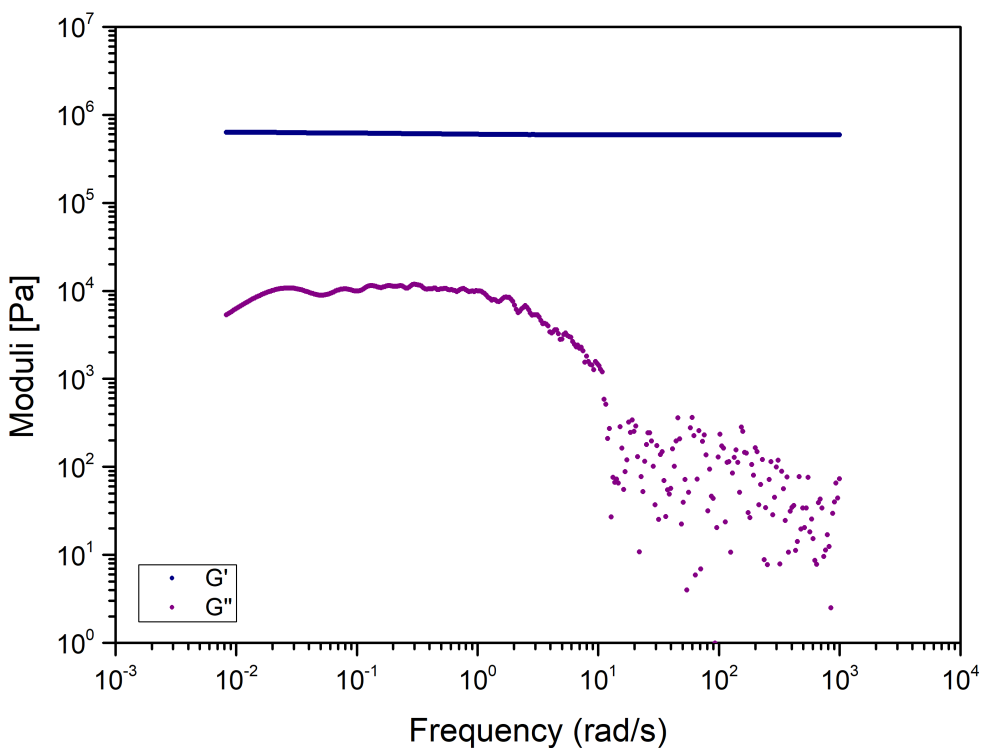


Figure B.114: the 20:1 PDMS sample's viscoelastic moduli derived by means of i-Rheo indentation using spherical indenter with 8mm in diameter and applying 0.7mm depth

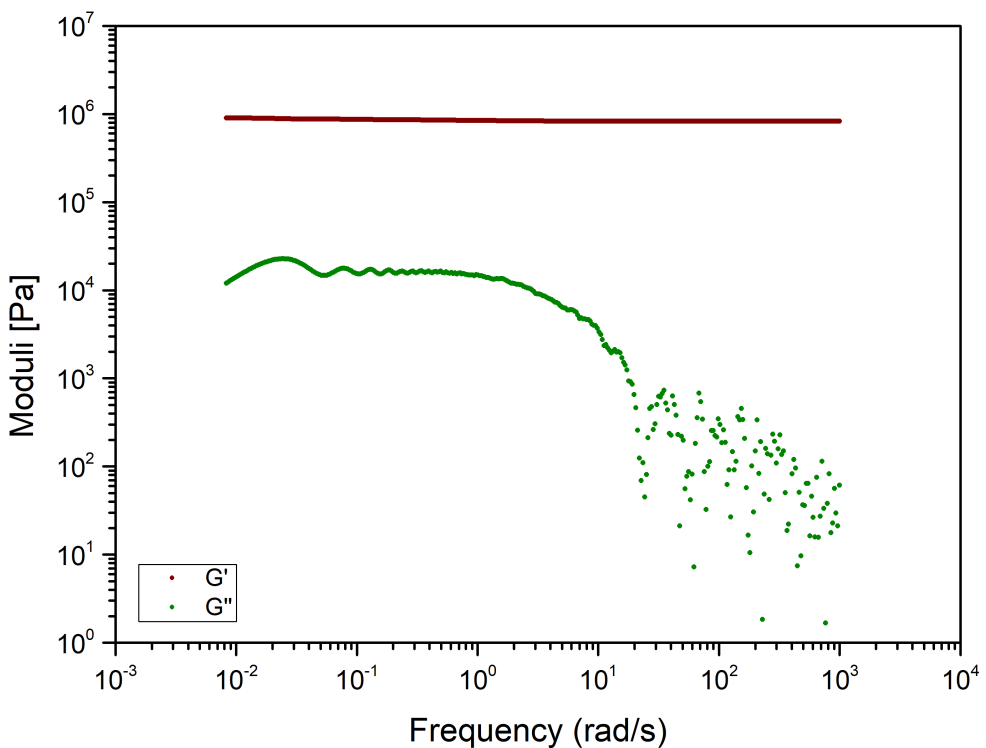


Figure B.115: the 20:1 PDMS sample's viscoelastic moduli derived by means of i-Rheo indentation using spherical indenter with 8mm in diameter and applying 1mm depth

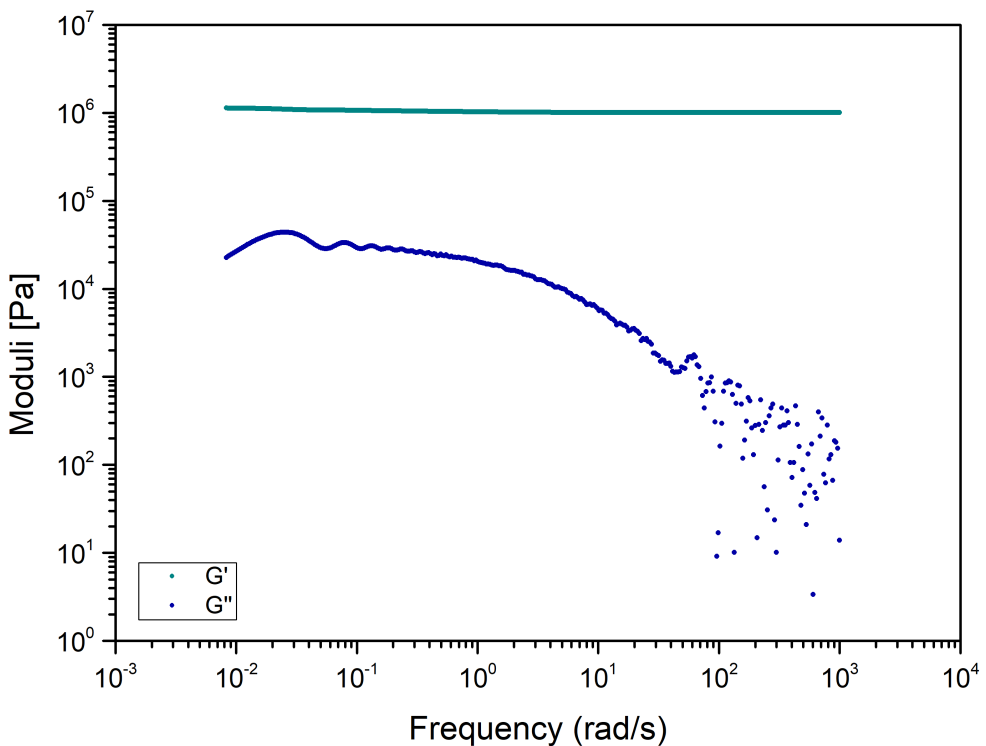


Figure B.116: the 20:1 PDMS sample's viscoelastic moduli derived by means of i-Rheo indentation using spherical indenter with 8mm in diameter and applying 1.4mm depth